USDOT Tier 1
University Transportation Center
on Improving Rail Transportation
Infrastructure Sustainability and Durability

Final Report VT-8

QUANTITATIVE EVALUATION OF EFFECT OF TOP OF RAIL FRICTION MODIFIERS ON REDUCING WHEEL AND RAIL WEAR

Mehdi Ahmadian, J. Bernard Jones Chair and Director

and

Ahmad Radmehr, Graduate Research Assistant

Center for Vehicle Systems and Safety
Railway Technologies Laboratory
Virginia Tech
3103 Commerce Street
Blacksburg, VA 24060

October 2021

Grant Number: 69A3551747132

DISCLAIMER

ABSTRACT

This study provides a detailed experimental evaluation of wheel-rail interaction for railroad vehicles, using the Virginia Tech Federal Railroad Administration (VT-FRA) Roller Rig. Various contact dynamics that emulate field application of railroad wheels on tracks are set up on the rig under precise, highly controlled and repeatable conditions. For each set up, the longitudinal and lateral traction (creep) forces are measured for different percent creepages, wheel loads, and angle of attack. The tests are performed using quarter-scaled wheels with different profiles, one cylindrical and the other AAR-1B with 1:20 taper. Beyond the contact forces, the wheel wear and the deposition of worn materials are measured and estimated as a function of time using a micron-precision laser optics measurement device. The change in traction versus amount of worn material at the contact surface is analyzed and related to wheel-rail friction. It is determined that the accumulation of the worn material at the contact surface, which appears as a fine gray powder, acts as a friction modifier that increases friction. The friction (traction) increase occurs asymptotically. Initially, it increases rapidly with time (and worn material accumulation) and eventually reaches a plateau that defines the maximum friction (traction) at a stable rate. It is estimated that the maximum is reached when the running surface is saturated with the worn material. Prior to the saturation, the friction increases directly with increasing amount of deposited material. The material that accumulates naturally at the surface—hence, referred to as "natural third-body layer"—is estimated to be a ferrous oxide. It has an opposite effect from the Top of Rail friction modifiers (TOR) that are deposited onto the rail surface to reduce friction in a controlled manner.

Additionally, the results of the study indicate that longitudinal traction decreases nonlinearly with increasing angle of attack (AoA) while lateral traction increases, also nonlinearly. The AoA is varied from -2.0 to 2.0 degrees, representing a right- and left-hand curve. Lateral traction increases at a high rate with increasing AoA between 0.0 – 0.5 degrees and increases at a slow rate beyond 0.5 degree. Similarly, longitudinal traction reduces at a high rate for smaller AoA and at a slower rate for larger AoA. For the tapered wheel, an offset in lateral forces is observed for a right-hand curve versus a left-hand curve. The wheel taper generates a lateral traction that is present at all time. In one direction, it adds to the lateral traction due to the AoA while in the opposite direction it subtracts from it, resulting in unequal lateral traction for the same AoA in a right-hand versus a left-hand curve.

The change in traction with changing wheel load is nearly linear under steady state conditions. Increasing the wheel load increases both longitudinal and lateral tractions linearly. This is attributed to the friction-like behavior of longitudinal and lateral tractions.

An attempt is made to measure the contact shape with wheel load and AoA using pressure-sensitive films with various degrees of sensitivity. Additionally, the mathematical modeling of the wheel-roller contact in both pure steel-to-steel contact and in presence of pressure sensitive films is presented. The modeling results are in good agreement with the measurements, indicating that the pressure sensitive films have a measurable effect on the shape and contact patch pressure distribution, as compared with steel-to-steel.

Content

LIST OF FIGURES

LIST OF TABLES

1. Introduction

1.1. Motivation

There exists a large number of studies that concentrate on better understating of the wheel-rail mechanics, extending over the past century. While a limited number of these studies have been based on field measurements or laboratory experiments that intend to emulate wheel-rail running condition in the field, the vast majority resort to analytical means that are based on the classical Hertzian contact and its advancements. During the past four decades, the majority of the wheel-rail contact studies are based on Finite Element (FE) studies that are often difficult to calibrate with field testing or laboratory experiments. Field tests are inherently prone to wide variations in measurements due to the various uncontrolled environmental elements. On the other hand, although the test conditions can be controlled far more precisely in the laboratory, the means of testing have often been limited to disk machines that use small rollers that do not accurately represent the true running contact mechanics of the full-size wheel on rail. There is a need for more sophisticated testing that can be better emulate the field conditions. There is also a need for performing tests that can help with verifying some of the theories that stem from the contact mechanic models that have existed for the past few decades.

The primary thrust of this study is to use the recently-commissioned Virginia Tech-Federal Railroad Administration (VT-FRA) roller rig to provide experimental verification for some of the analytical and FE theories that have been suggested in the literature, through precisely-controlled design of experiments. It is also intended to offer observations and practical evaluations that can further enhance railroad’s safety and operational efficiency.

The VT-FRA roller rig, which has been successfully designed and fabricated at the Railway Technologies Laboratory (RTL) at Virginia Tech provides an unprecedented opportunity to explore the physics and mechanics of wheel-rail interface (WRI). The rig provides the means for measuring traction (creep) forces at the wheel-rail contact with a high degree of accuracy under precisely-controlled conditions. One can accurately position a quarter-scaled wheel against a roller with a running-surface profile of a quarter-scaled 136RE rail. The rig enables conducting experiments under various wheel-rail conditions that emulate the field environment for a full-scale wheel and rail. The rig is equipped with two AC traction motors that allows precise control of the wheel and roller rotational speed, hence achieving various percent creepages accurately and repeatably. It is also equipped with six electromagnetic servo motors that allow precise control of wheel load, lateral position, angle of attack (AoA), and cant.

1.2. Objectives

The primary objectives of this study are to:

- Provide the means for conducting experiments that can further verify the analytical and numerical models that exist for wheel-rail contact mechanics and dynamics,
- Measure the wheel-rail contact dynamics and the changes occurring at the running surfaces under precise and repeatable conditions,

- Experimentally study the effects of wheel load and angle of attach between the wheel and rail for various percent creepages,
- Evaluate the effect of naturally-occurring due to wheel wear or added third-body layers on traction forces,
- Determine the changes in contact size and pressure resulting from the running condition of wheel on rail statically and possibly dynamically,
- Provide recommendations that can improve the safety and operational efficiency of the U.S. railroad industry.

1.3. Approach

The objectives of this study are intended to be achieved through

1. Improving the capabilities of the VT-FRA roller rig such that it can be used in areas such as enabling precise measurement of the changes that occur to running surfaces with time under the test conditions, and
2. Conducting a series of experiments that can provide the basis for the scientific analysis that is needed for the study's goal.

The following specific steps are taken for this study:

- A literature review is performed on the parameters affecting creep forces and contact conditions.
- A thorough investigation of of-the-shelf sensors that are available for precise measurement of surface topography is performed, two are selected for a pilot evaluation, and one is chosen for implementation onto the roller rig.
- Experiments are designed and performed to evaluate the accumulation of natural third body layer at the running surfaces and its effect on lateral and longitudinal creep forces.
- Several critical parameters of the wheel-rail interaction are studied in-depth and the critical ones are chosen for more in-depth analysis through a design of experiment.
- Angle of attack as a critical factor in derailment is investigated through a series of experiments in which the changes in lateral and longitudinal traction are evaluated for different running surface conditions.
- A dynamic resonance-like condition, referred to as "high frequency dynamics," is evaluated experimentally in support of the past modeling studies by Vtech CMCC.
- The laser scanner is utilized to measure the wheel surface topography and analyze the third body layer accumulation.
- An evaluation of various methods for statically measuring contact patch is performed and a special type of pressure sensitive film is selected to study the shape and pressure distribution at the contact.

1.4. Contributions

The potential contributions of the research presented in this study to wheel-rail interface (WRI) mechanics and dynamics are:

- Analyzing experimental creep forces and traction coefficient that can be related to some actual wheel-rail interactions in the railroad.
- Evaluating the effect of third body layer generation at contact, which has a significant influence on traction behavior.
- Calculating the range of high frequencies, which occur at contact, and analyzing to what extent the high frequencies are related to the material, geometry, and contact force.
- Measuring the wheel surface topography and estimating the natural third body layer accumulation.
- Measuring the actual contact patch geometry on the roller rig and evaluating the contact area and pressure.

1.5. Outline

The results of this study are organized in eight chapters that are intended to provide a step-by-step and detailed description of the work that has been performed. Specifically,

- Chapter 1 introduces the study and provides the objective, approach to address the issues, potential contributions in railroads, and an outline of the report.
- Chapter 2 provides the background for the study.
- Chapter 3 presents a brief description of VT-FRA Roller Rig capabilities and accuracy of measurements.
- Chapter 4 introduces the high frequency dynamics and evaluates the eigenfrequencies, eigenvectors, and the resulting high frequency on the rig.
- Chapter 5 analyzes the creep forces and traction coefficients obtained from experimenting on the rig under various test conditions.
- Chapter 6 introduces the newly added surface scanner for measuring the changes to the running surface roughness and accumulation of any worn material as a third-body layer and provide the details of measurements made under various running conditions.
- Chapter 7 investigates the contact patch geometry and pressure distribution for different positionings of wheel and rail relative to each other, statically.
- Chapter 8 provides a summary of the work and discusses the recommendation for future studies.

2. Background and Literature Review

This chapter provides a review of some of the past studies that have been performed in evaluating the parameters affecting wheel-rail traction. It also includes an overview of the various methods used for measuring contact patch geometry and pressure distribution, and some of the conclusions that have been reached. Some of the improvements made to the approaches and methods to the past studies are summarized at the conclusion of the chapter.

2.1. Background on Third Body Layers

Some studies have been performed to evaluate the third body layers influence on the wheel-rail interaction, composition of the third body layers, and methods of measuring friction. They have shown that the third body layer can act as a friction modifier and either increases or decreases the coefficient of friction at the wheel-rail contact. In some cases, it may have a neutral effect. In some studies, the traction coefficient is measured for a given slip ratio and low rolling speed for wet surface condition [1]. In some others, the differences between the new and worn test surfaces are investigated. In most of these studies, the experiments are performed on a twin-disc rolling-sliding frictional machine, such as the one shown in

Figure 2.1. In this test rig, two relatively small disks are used to perform the experiments under controlled condition.

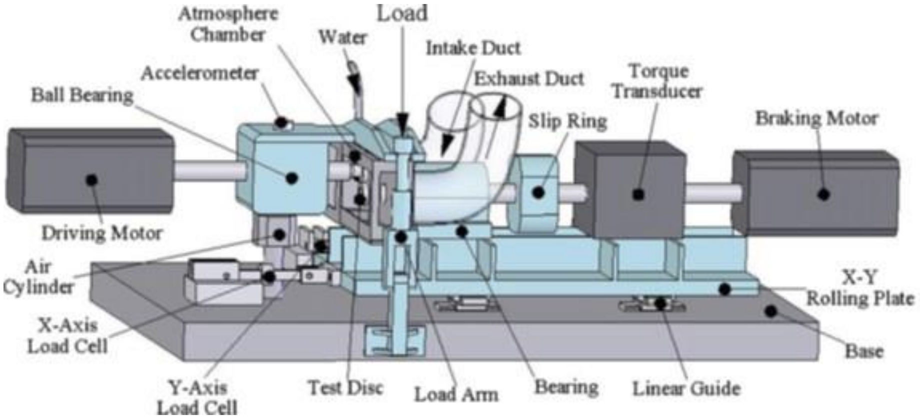

Figure 2.1 Twin-Disc Rolling-Sliding Frictional Machine [1]

Baek [1] investigated the effect of rolling speed, contact pressure, and slip ratio on the traction coefficient. The study shows that the traction coefficient increases and become steady under dry conditions. In another study, the same group investigated the influence of dry and unlubricated conditions with varying humidity and temperature on the transient traction coefficient at the wheel-rail interface [2]. The same test setup was utilized to report the environmental variables like temperature and relative humidity on the traction characteristics. It is considered that surface roughness, effective hardness, oxide layer, and the third body layer comprising wear debris has a significant effect on the variations in traction coefficient. Although several parameters are investigated in these studies, the twin-disc machine does not exactly replicate the actual wheel-rail contact conditions, and the results may have large deviations.

The third body layer and contaminants have significant effects on the wheel-rail contact. Ballast stone, asphaltic oil, and aluminum powder are among the artificial third body layers considered by Berthier and Descartes [3]–[5]. Lewis [6] determined the traction levels by developing a pendulum rig, and considering states of contamination under dry and wet conditions. The results indicate significantly higher levels of friction for dry surfaces compared to wet and oily contacts. In another study, a Fastsim algorithm is developed to analyze the traction coefficients [7]. In this study, the creep force model is identified from the measured data. Although the model can be used approximately instead of Polach's model [8] but it is limited to the application of large tractive or braking efforts under various contact conditions such as dry, wet, and polluted.

Zhu [9] performed several experiments on a mini-traction machine to investigate factors influencing wheel-rail adhesion under dry conditions and using water or oil as lubricants. In addition, surface topographies are measured to correlate the test results with surface conditions. The results indicate that rough surfaces have slightly higher adhesion coefficients than smooth surfaces in oil-lubricated tests. In water-lubricated tests, the low adhesion coefficient is observed, even lower than oil-lubricated tests. In another study, Zhu [10] used a pin-on-disc test setup to evaluate the influence of environmental conditions and iron oxides on the coefficient of friction between the wheel and rail. Results indicate that the coefficient of friction decreases with increasing relative humidity up to a saturation level because water molecules act as a lubrication film. The papers provide good understanding of the behavior of different friction modifiers, whether they enhance the traction or decrease the creep forces, but a pin-on disc machine may not be an appropriate representation of the real-world condition.

Nakahara [11] utilized a twin-disc of pearlite carbon steel to evaluate the relationship between transient traction coefficient and the surface oxide layer. The results indicate that $\alpha - Fe_2O_3$ causes an abrupt increase in the traction coefficient under both dry and wet conditions; however, Fe_3O_4 may suppress the increase in the traction coefficient. In another study, Hou [12] suggested an elastic-plastic rheological model for the third body layer. A rheometer is used to generate an extensive database of rheological properties for numerous constituents. The shear stress for several compounds was analyzed. Based on the results, it is mentioned that friction modifying interfacial layers can exhibit positive, neutral, and negative friction characteristics.

Arias-Cuevas [13] used a twin-disc roller rig to evaluate the performance of two friction modifiers in dry and wet contacts. A schematic of the rig is presented in

Figure 2.2. The adhesion characteristics of friction modifiers are examined for different slip ratios. In dry conditions, the highest adhesion coefficients are obtained. In the presence of water, the adhesion coefficient is reduced, which my lead to traction problem for the rail vehicles.

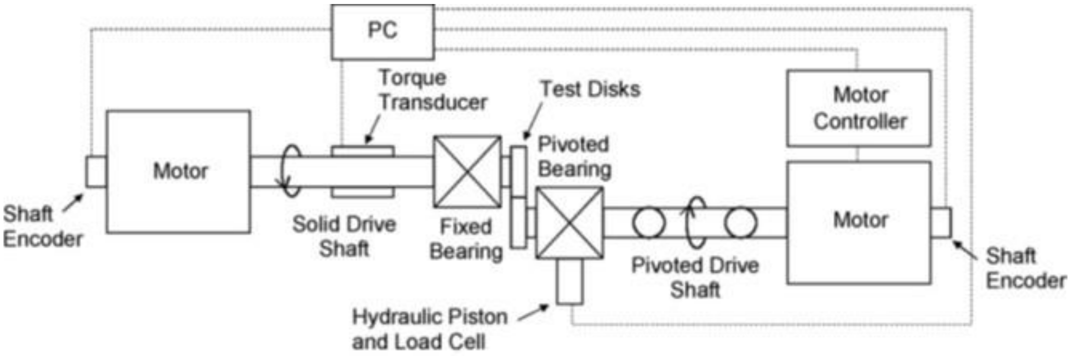

Figure 2.2 Schematic Representation of the Roller Rig [13]

Friction modifiers are using for reduction of noise, lateral forces, wear, rolling contact fatigue, etc. [14]. Several iron oxides performances on friction are reviewed by Zhu [15]. The influence of various types of iron oxides on friction and adhesion differs. Besides, the thickness of the iron oxide layer affects friction and wear. Meierhofer [16] performed several experiments and defined a model to describe the influence of the traction coefficient at contact. The twin-disc test presented in the paper shows that the layer consists of iron and iron oxides with a thickness of up to $50\ \mu m$. A qualitative and quantitative agreement is achieved on the effect of third body layers on traction coefficients.

Ronasi [17] carried out an experimental approach to identify the traction-creepage curve at the wheel-rail interface. The measurement apparatus consists of two discs of different sizes, which one is driven by an electromotor, and the other is idle. The two discs are pressed on each other to simulate the contact force. The results show that traction coefficient goes up with increasing percent creepage until it reaches the maximum value. Voltr [18] investigated the transient wheel-rail traction behavior using a tram wheel test rig. The test rig is presented in

Figure 2.3. The experiments indicate that the effective adhesion characteristic cannot be relied upon to conform to the ideal, theoretical shape. Analysis in the study shows that the differences can be related to the dynamic nature of the observed phenomena.

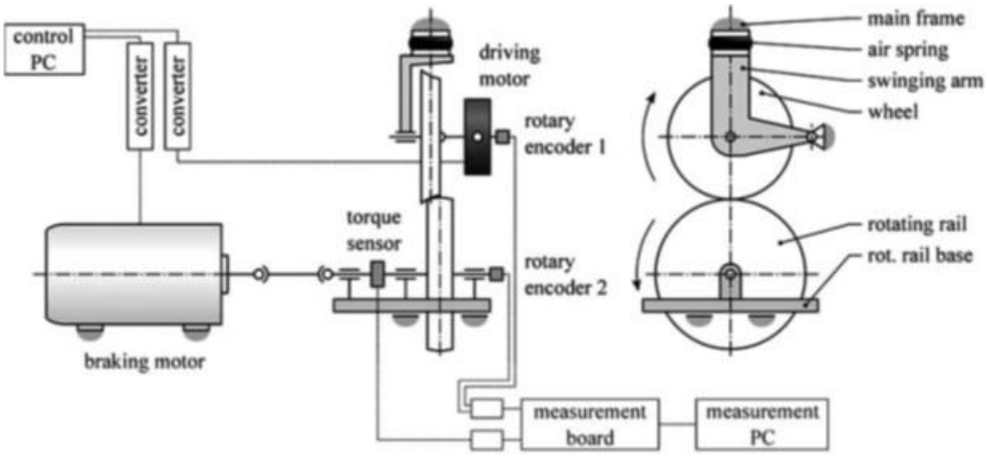

Figure 2.3 Diagram of the Tram Wheel Test Rig [18]

Lewi

s [19] investigated the effect of several types of third body layers on traction coefficients. The traction coefficient is simulated under dry, wet, oil, wet leaves, and dry leaves. It is observed that solid particles entered into the wheel-rail contact cannot support the high loads and so are crushed or deformed into smaller fragments. These go into the contact and damage the running surfaces. Sand is used in the area of low traction to enhance the friction coefficient with solid materials. Liquids form a thin layer between the wheel and rail, causing a reduction in traction. The presence of leaves on the track leads to chemical reactions between the rail steel and leaf constituents. It provides a highly durable, very low friction solid film on the surface.

Zhang [20] performed the adhesion test under various conditions of the wheel-rail contact, such as various speed, axle-loads, and contamination situation. The results show that the adhesion coefficient of the wheel-rail decreases with increasing in the axle-load and running speed under the water contaminated conditions. Also, the adhesion coefficients keep high values and do not drop much under the condition of dry and clean surfaces.

Arias-Cuevas [21] investigated the influence of sand particle sizes on adhesion. Sand-based friction modifiers are another type of materials that some railroads are using to overcome low adhesion incidents caused by contamination like wet tracks or crushed leaf residue at the running surface. In this study, the wheel-rail contact is simulated using a twin-disc roller rig. The results show that large particle sizes of sand yield a higher adhesion coefficient; however, it may cause more wear depending on the slip. Large particle sizes and high slips increase the work-hardening caused on the surfaces of both wheel and rail disks.

Trummer [22] presented a model to predict adhesion in rolling contact in the presence of water. The model is parametrized based on experimental results from a tram wheel test rig. To realize low amounts of water at contact, water is applied drop-wise to the rotating rail roller at a constant rate. The system is illustrated in Figure 2.4. The results show that low amounts of water considerably influence the adhesion level and the shape of the adhesion curve.

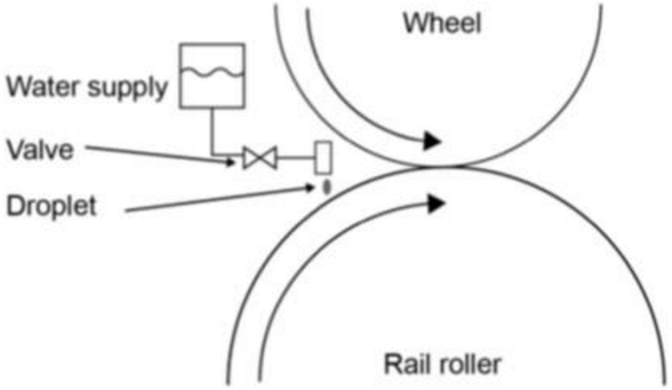

Figure 2.4 Drop-Wise Application of Low Amounts of Water by a Gravity Fed Water Application System at the Tram Wheel Test Rig [22]

Using the regression analysis, Xi [23] presented a formula on the numerical results of a wide range of parameters to estimate the traction coefficient for rolling-sliding contacts. The parameters include geometry, surface roughness, creepage, friction coefficient, and contact radius. Experiments were conducted on ball-on-disc test rig under dry and mixed lubrication conditions. For the experiments under dry condition, the ball and the disc are cleaned with heptane. For the experiments under mixed lubrication, the paraffin oil used as a lubricant. The results indicate that the formula's predictions are in good agreement with measurements on the rig. The traction levels with the oil lubricant are far lower than the measurements under dry condition.

Cao [24] investigated the effect of alumina particle, as a third body layer, on improving adhesion and wear damage of the wheel-rail interaction. The rig is composed of two rollers as the wheel and the roller. All experiments are carried out under wet conditions, and the water is continuously added to the contact surface of the wheel-rail using an infusion tube. The alumina particles are mainly composed of Al_2O_3. A schematic representation of the test setup is presented in Figure 2.5. The results indicate that alumina particles significantly improve adhesion coefficient.

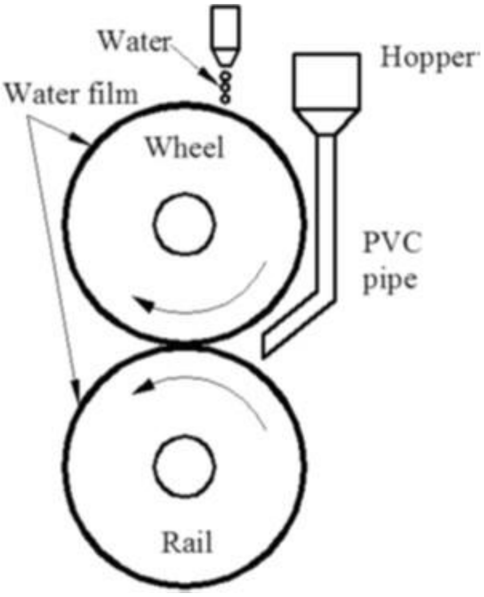

Figure 2.5 Scheme of the Application of Alumina Particle [24]

Galas [25] studied the role of typical water-based friction modifier constituents in terms of adhesion and film formation. The experiments were performed on a commercial ball-on-disc apparatus. A wide range of substance compositions is used where the content of base medium, binding agent, particles for friction modification, and solid lubricant varied. Binding agents are usually clays, such as bentonite or casein. The results show that less complex substances, e.g., free of particles for friction modification, can provide required adhesion. Substances consisting of water and bentonite can provide the intermediate level of adhesion.

Buckley-Johnstone [26] evaluated the effect of iron oxides on adhesion. In this study, a high-pressure torsion setup is developed to investigate the effect of small amounts of water and iron oxides when subjected to different contact pressures. The experiments show that the adhesion reduced due to the presence of water or iron oxide. Goryacheva [27] modeled the viscoelastic layer effect in rolling contact. The dependence of the adhesion coefficient on the relative slippage is analyzed based on several surface layer viscosity parameters. The results show that increasing the sliding friction coefficient between the layer and the roller leads to increasing adhesion coefficient and the value of the relative slippage corresponding to transition from rolling to complete sliding.

Current literature on the effect of third body layers is rich in quantity but lacks enough accurate and reliable information. Several researchers have made great efforts to bring meaningful explanations to the real phenomenon on wheel-rail interaction. They have usually used small twin-disc machines, which does not accurately replicate the wheel-rail contact. The results are mostly not comparable to the wheel-track interactions in the field due to the inaccurate design of machines and lack of implementing scaling factors. Additionally, there are several studies concluding that the third body layers decrease the creep forces and act as a lubricant, while others say that the third body layers enhance the creep forces and tractions. In the current study, a precise piece of equipment is used to evaluate the effect of several parameters on creep forces and traction coefficients. The results can be scaled and compared with the real wheel-rail contact due to the accurate design of the machine and testing in a highly controlled environment.

2.2. Background on the Surface Measurement and Contact Patch Studies

The wheel and the rail interact with each other in a small region called contact patch. Most of the parameters affecting the traction such as creep forces, pressure distribution, and contact area are occurring in the contact patch. Therefore, evaluating the contact patch geometry, area, and pressure distribution are essential for researchers working on the wheel-rail interaction. There are several methods to measure the contact geometry and pressure distribution. Rovira [28] used the ultrasound method to nondestructively quantify the stress distribution in new, worn, and damaged wheel-rail contacts. The response of a wheel-rail interface can be modeled as a spring. If the pressure is high, there would be few air gaps, which allows transmitting an ultrasonic sound wave [28]. Unused contact surfaces have similar contact areas as the Hertzian solution. Figure 2.6 shows the contact patch from the unused, sand damaged, and worn wheel-rail interfaces. Although the load is similar for all cases, the contact patch is extremely fragmented. The sand damage leads to a rough surface [28].

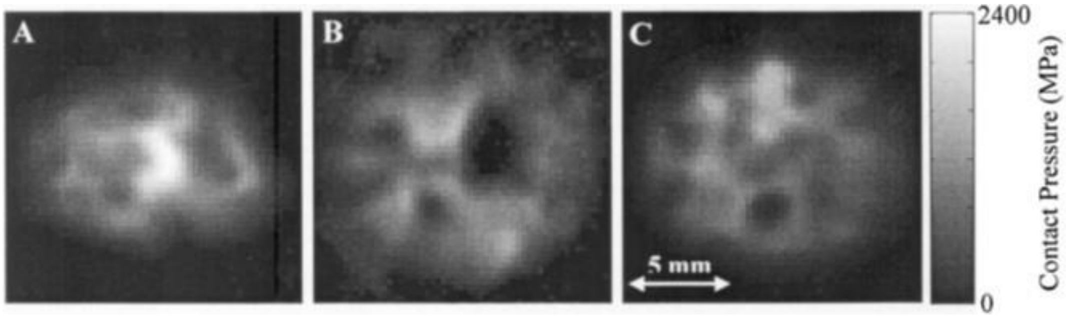

Figure 2.6 Wheel-Rail Contact at 65 kN for (a) Unused, (b) Sand Damaged, and (c) Worn Specimens [28]

In another paper, Zhou [29] used the same ultrasonic method to estimate the distribution of contact pressure in a real wheel-rail system. A set of tests were performed on a simple sphere-plate to analyze the reflection of ultrasonic sound from the interface. Besides, a finite element model is established to relate the contact pressure and ultrasonic reflection. Piotrowski [30] compared the experimental measurements of the ultrasonic reflection with the Hertz model. Although, he found that there is a deviation between measured data and Hertz theory, the difference of the average magnitudes of the contact patches are reported to be small. The wear life of a component highly depends on its initial topography, and the wear mechanisms of the surface will vary. Therefore, different initial conditions for the same running environment of the component would influence its overall life [30].

Ayasse [31] provided the measurement of a dynamic wheel-rail contact patch using an ultrasonic method. The approach could provide not only the contact patch but a detailed and relatively high-resolution pressure distribution. The results were validated by conducting finite element methods. A sample of the results is presented in

Figure 2.7.

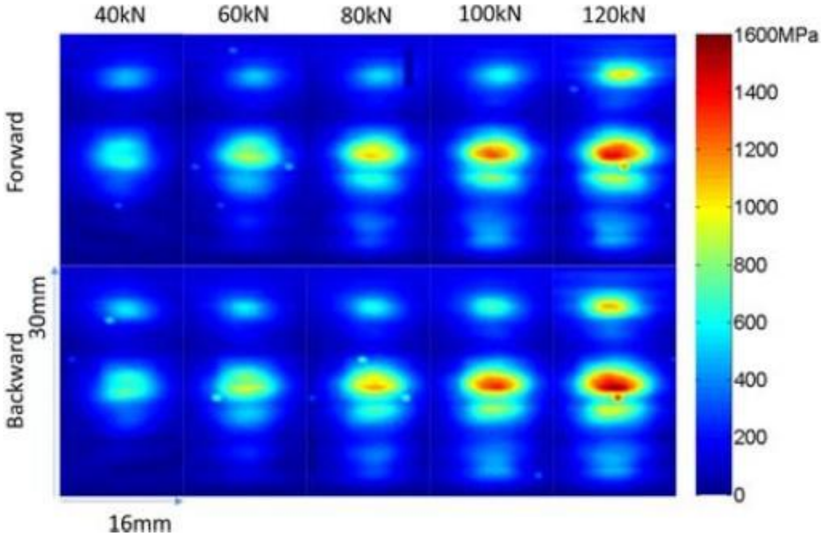

Figure 2.7 Contact Pressure Maps at $\mathbf{1}\ \boldsymbol{mm/s}$ [31]

Braghin [32] investigated the Wheel-rail contact models for vehicle system dynamics. Several methods were discussed in the paper, and the corresponding formulation was provided. In another study, Sichani [33] analyzed the wheel-rail contact patch in semi-Hertzian conditions. The method was based on the interpenetration of the bodies, which is, in fact, the value of the plastic approach between two bodies.

A wheel wear prediction is rather complicated due to the simulation of vehicle dynamics, local wheel-rail contact models, and local wear model [34]. Sun [34] represented a wear prediction model that was validated by experimental data. The wear tests were carried out using a twin-disc test machine. Simulations of wheelset life showed that a re-profiling of the wheel after 200,000 km would nearly double the wheel service life thus minimizing total life cycle costs [34].

Skrypnyk [35] investigated the approximate analytical model for calculating the contact patch and pressure distribution. The results were compared with a more detailed numerical method. In this method, the surface deformations were approximated in order to reduce the computational cost. The contact patch and pressure distribution estimated by the proposed method were in good agreement with the ones obtained by the rigorous numerical method. Polach [36] provided another mathematical model to study the wheel-rail normal contact problem. The model can consider the relationship between the elastic deformation of a line and the normal pressure distribution within the contact patch.

Myamlin [37] presented metamodels to predict the wheel-rail normal contact in railway switches and crossings. The first type of model was based on response surface methodology and was represented by a polynomial. The second type was based on Hertzian contact theory. For a given material, the model computes the size of the contact patch and the maximum contact pressure as a function of the normal force and the local curvatures of the bodies in contact. The performance of both models was quantified, and it was found out that the Hertzian-based model was more accurate.

The equivalent conicity is commonly used to evaluate the wheel-rail contact geometry [38]. Jaschinski [38] proposed other parameters to support the contact patch geometry assessment. A parameter, called contact concentration index, was presented to evaluate the contact conformity. The parameter was related to the development of the equivalent conicity due to wear and was calculated by averaging the contact concentration over the normal distribution between -3σ and 3σ of lateral wheelset displacement with the selected standard deviation σ.

Zhu [39] modeled a non-Hertzian wheel-rail contact considering wheelset yaw. The paper proposed a proper penetration for the non-Hertzian model by considering the change of local relative curvature of wheel-rail profiles based on semi-Hertzian method. The method was used for the wheel wear prediction of a high-speed train. Piotrowski [40] described a new procedure of regularization of the non-elliptical contact patch. In this paper, a look-up table for non-Hertzian contact, which was a fast creep force generator that can be used by multibody dynamics system simulation programs.

Although several studies are conducted on evaluating the wheel-rail contact patch, there are still some ambiguity in the test results. The contact geometry and pressure distribution are highly affected by the wheel and rail surface topography. Using a test rig, which does not replicate the actual contact condition, may not represent the geometry and pressure distribution accurately. In addition, the ultrasound can pass from one body to another when the clearance is too small. Therefore, the contact patch represented by the ultrasound method does not accurately simulate the actual contact between bodies. In this study, the contact geometry is measured using pressure sensitive films with various measurement accuracies. The results are analyzed, and the error caused by the method is presented.

3. VT-FRA Roller Rig Test Setup

3.1. Brief Description of VT-FRA Roller Rig

Roller rigs are often used for studying contact mechanics and dynamics by researchers for railroad applications. A wide variety of experiments with high degree of repeatability and flexibility can be set on the roller rigs [41]. Often, a roller rig is designed and fabricated for a specific demand or goal. For example, they are used to measure hunting dynamics of the wheelset or railway bogie/truck, study wheel-rail interactions, simulate vehicle vibrations on track, simulate the process of train acceleration and braking, or study rolling contact fatigue and wear [42]. The VT-FRA roller rig is designed and built with the specific goal of evaluating the wheel-rail contact mechanics and dynamics with a high degree of precision.

The rig consists of two rotating bodies, a wheel, and a roller, simulating a train wheel and the rail, respectively. The wheel is one-fourth scaled-down of a 36-inch railcar, and the roller is a 44-inch wheel, which is approximately five times larger than the scaled-wheel. The wheel mounted on the rig can be replaced easily with any other kinds of wheels. Mostly, a cylindrical wheel and a tapered wheel are used on the VT-FRA Roller Rig to simulate various conditions of wheel-rail interaction on the rig. The tapered wheel is a one-fourth scaled-down of AAR-1B wide-flange wheel type. The AAR-1B wheel profile is shown in Figure 3.1. According to the drawing, the wheel has a 1:20 taper, which affects the contact shape, creep forces, and traction coefficients significantly.

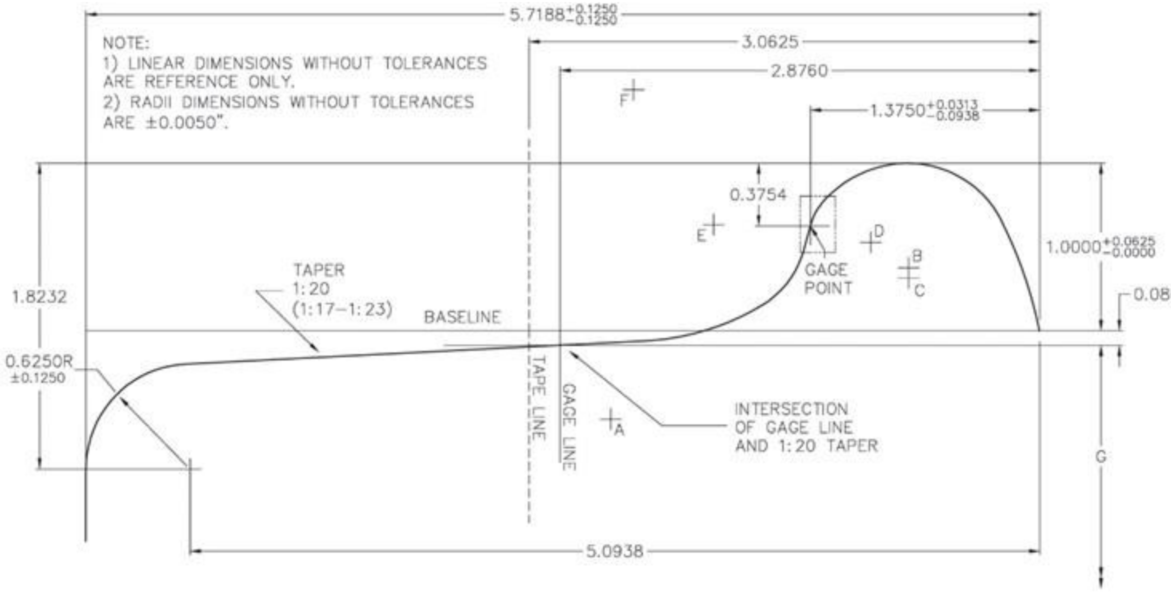

Figure 3.1 AAR-1B Wheel Profile [43]

The roller flange surface is machined to US-136 rail profile in one-fourth scale to replicate and simulate the real-world scenario and prevent distortion of the wheel-roller contact. The US-136 rail profile is shown in Figure 3.2.

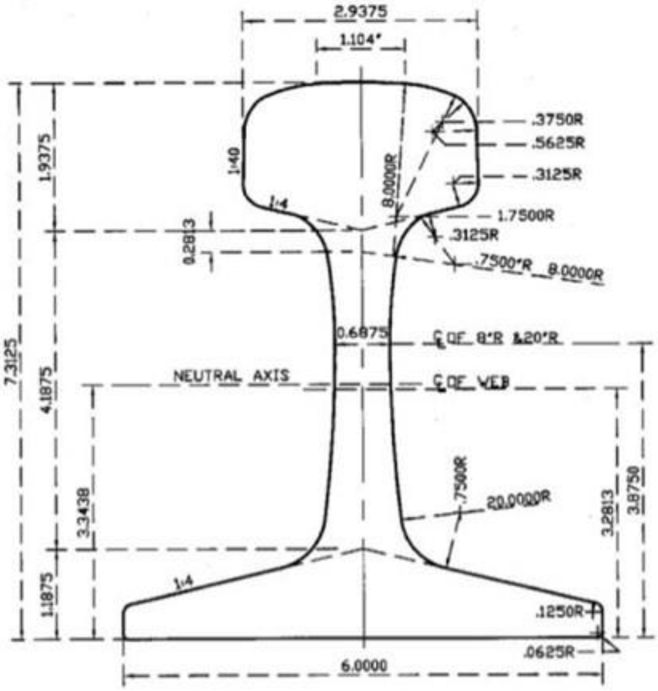

Figure 3.2 AREMA 136-lbs RE Rail Profile [44]

The wheel and roller are configured in a vertical direction with the wheel on top and the roller on the bottom. A schematic of the roller rig is presented in Figure 3.3. Figure 3.3 (right) shows a scaled AAR-1B wheel located on the roller. Each of the wheel and roller can be rotated precisely at desired rotational speeds since they are mounted on two independent drivelines. The slip condition at wheel and roller contact can be simulated based on the commanded wheel and roller angular velocities.

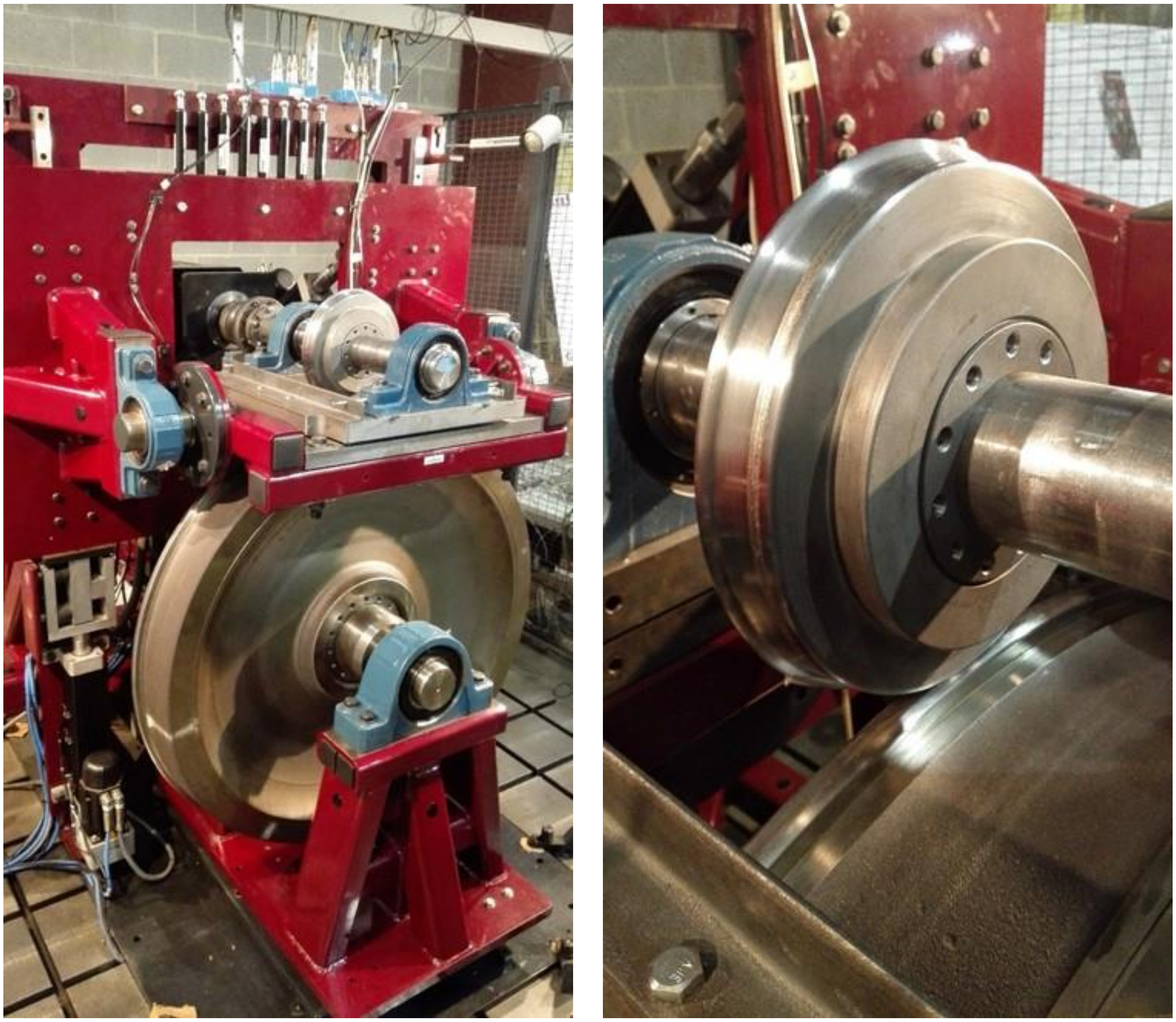

Figure 3.3 VT-FRA Roller Rig (Left) and the Wheel and Roller Relative Position (Right)

The rig consists of two load measurement platforms of four tri-axial load cells. The load cells measure the contact forces in three dimensions while experimenting. The primary load platform is placed on the cradle frame in-plane with the contact patch. The secondary platform is placed in the motor-side of the roller rig, measuring the loads passing through the driveline. The solid model of the measurement load platforms with load-path routes are shown in Figure 3.4. The total force and torque can be calculated based on the forces applied on both load platforms.

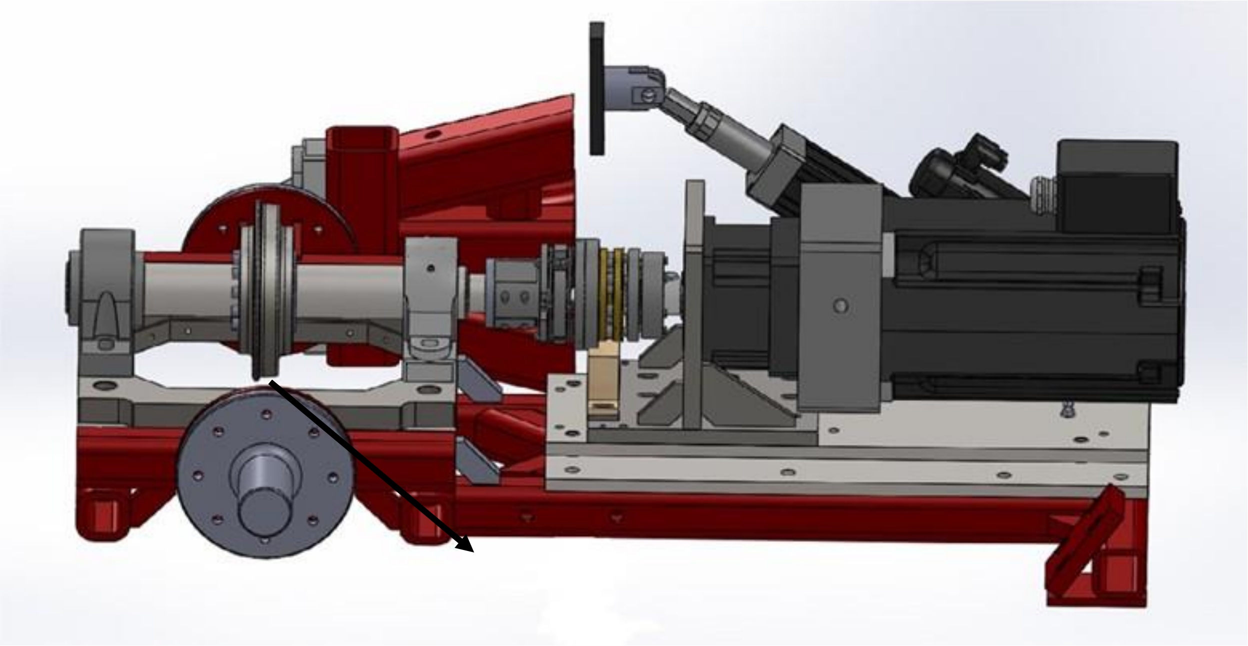

Figure 3.4 Solid Model of Primary and Secondary Load Measurement Platforms [45]

One of the significant features of the rig is controlling the relative position between the wheel and the roller precisely. Six linear actuators are utilized to control the relative wheel-rail position. Two of them are positioned vertically to move the wheel in a vertical configuration. The wheel can be pressed on the roller surface to achieve the desired force using the vertical actuators. Two other linear actuators control the cant angle between the wheel and the roller in the roll direction. Besides, the rig is equipped with one linear actuator to position the roller laterally relative to the wheel. Another linear actuator controls the angle of attack positioning. Accordingly, the wheel can be positioned precisely relative to the roller in different configurations including normal load, yaw, roll, and lateral displacement. The wheel-rail relative position can be maintained while experimenting to make sure tests are conducted in a controlled environment.

3.2. Scaling Factors

One of the key factors that affects the test results of a roller rig significantly is the scaling factor. It is vital to know how the results of a roller rig is comparable with the actual condition in the field. To be able to correlate the wheel-rail tangent track and a scaled roller rig results, it is needed to consider three different factors, correction factor, scaling factor, and transformation factor. Keylin [46] has done a comprehensive study to evaluate the factors. The relationship between a tangent track and a full-scale roller rig can be evaluated using correction factors, and scaling factors can be used when a full-size roller rig is compared with a scaled one. Transformation factor is the combination of these two factors, which makes it possible to compare a tangent track with a scaled-roller rig. Figure 3.5 illustrates the factors needed to correlate a tangent track with a scaled-roller rig.

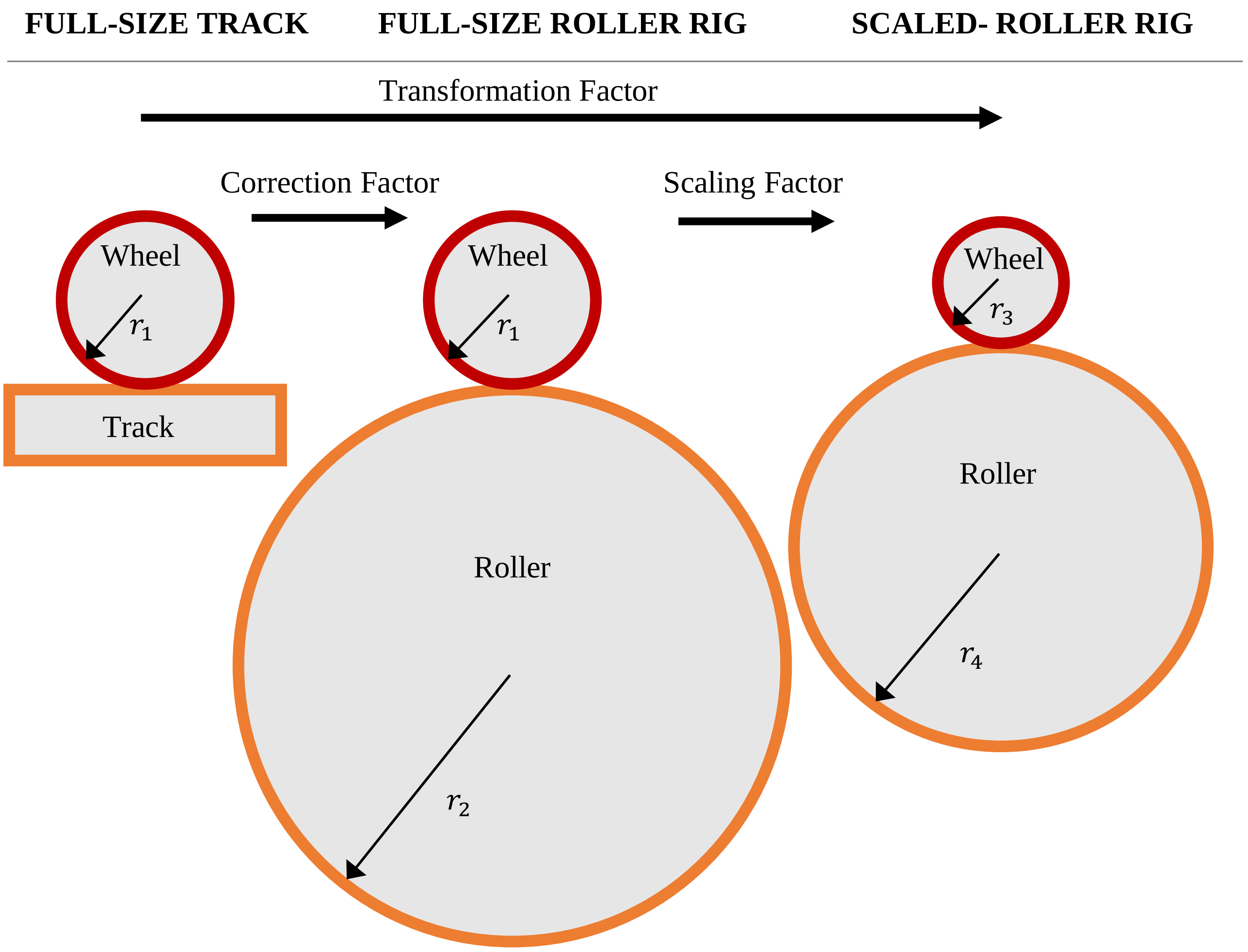

Figure 3.5 Factors Used to Correlate a Tangent Track with a Scaled-Roller Rig

According to Figure 3.5, an actual full-scale wheel has a radius of r_1, which is finally scale to r_3. The track is simulated to a roller using a correction factor. The full-size roller is shown by r_2 radius. For the VT-FRA roller rig, the roller radius is chosen to be approximately five times bigger than the wheel to minimize contact patch distortion. r_4 is the scaled radius of the roller. The ratio of the radii is presented in equation (3-1).

$$\frac{r_2}{r_1} = \frac{r_4}{r_3} \cong 5 \qquad \textbf{(3-1)}$$

Although a very small roller rig is more affordable and more controllable, it reduces the accuracy of measurements as the scaling factor increases. Besides, a full-scale roller rig is complex in design, needs bigger electric motors and components, reduces the accuracy of speed control and slip. For the VT-FRA roller rig, a length scaling factor of four is considered based on discussions with suppliers and rail experts, considering available components in the market, and conducting many design calculations. The length scaling factor is shown by the ratio of full-scale wheel and scaled-wheel radii in equation (3-2).

$$\frac{r_3}{r_1} = \frac{r_4}{r_2} = 4 \tag{3-2}$$

The other scaling factors for geometric, kinematic, and dynamic quantities are derived based on the defined length scaling factor and similarity of stresses. Table 3.1 shows some of the physical quantity scaling factors associated with the rig.

Table 3.1 The Scaling Factors for Physical Quantities of the Rig

PHYSICAL QUANTITY	SCALING FACTOR
Length	4
Time	4
Density	1
Area	16
Force	16
Velocity	1
Acceleration	$^1/_4$
Stiffness	4
Frequency	$^1/_4$
Mass	64
Friction Coefficient	1

3.3. Roller Rig's Capabilities

The strategy taken to develop the rig with specific scaling factors, accurate linear actuators, and motors, using a slew of sensors and load cells have made the VT-FRA roller rig a precise measurement tool to measure contact forces, and evaluate wheel surface condition with a high level of accuracy. Some of the key specifications related to the rig are:

- The wheel and the roller angular positions can be maintained within 0.1-degrees,
- The angle of attack and cant angle can be set in 0.05-degrees accuracy,
- Positioning accuracy is within $16\ nm$ of the target location,
- Although the creepage can be set to any desired value since the wheel and the roller drivelines are independent, a maximum creepage of 10% is considered for the rig to prevent damaging the roller,

- The wheel can be easily replaced with any other kinds of cylindrical, tapered, or profiled wheels,
- The vertical force capability is defined based on the safety and prevention of any damage to the rig.

A summary of the VT-FRA roller rig capabilities is presented in Table 3.2.

Table 3.2 Summary of VT-FRA Roller Rig Capabilities

	Dynamic	**Capability**
AC Motors	Wheel and Roller Rotations	Maximum Velocity: $10\ mph\ (16\ {}^{km}/_{h})$ Maximum Creepage: 10%
Linear Actuators	Lateral Displacement	The actuator can cover all the wheel width
	Angle of Attack	$\pm 6°$
	Cant Angle	$\pm 6°$
	Vertical Contact Force (Full Scale Wheel Load)	Min. Force: $1\ kN\ (16\ kN\ or\ 3.6\ kips)$ Max. Force: $12\ kN\ (192\ kN\ or\ 43\ kips)$

The rig's capabilities allow conducting various experiments, including creep force measurements at various %creepages, the effect of third body layers at various wheel load, %creepage, and angle of attack, the effect of flange contact on wheel-rail interface (WRI), the effect of surface finish and wear conditions on WRI, and measurement of contact geometry.

All test parameters can be set before running the experiments. During tests, the parameters are held constant. For simulating transient conditions such as sweeping the angle of attack (AoA) during curving, traction, braking, and changing %creepage, each parameter can be changed independent of the others during the tests.

The parameters that need to be changed during the experiment can be increased or decreased to reach the target value based on the desired motion, velocity, and acceleration, and jerk. The change in parameters can be according to one of the two shapes in Figure 3.6. The change from an initial to a final state can be achieved at a constant rate, shown by the trapezoidal shape in Figure 3.6. Alternatively, the change can be done in an "S" form in which the rate of change is nonlinear, to achieve a smoother transition (less jerk, in case of acceleration). The S-curve is more gradual at the start and end of the transition between the two states. Figure 3.6 shows the transition in velocity from 0 to a target value for both the constant rate (trapezoidal shape) and non-constant rate (the S-curve).

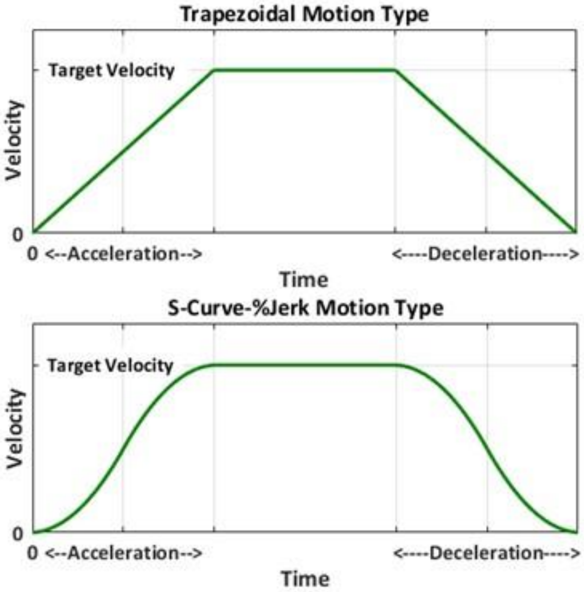

Figure 3.6 Trapezoidal and S-Curve-%Jerk Motion Types [47]

3.4. Roller Rig Data Analysis

Usually, every measurement contains a certain level of random deviations, called measuring noise, around the actual value. It is necessary to use noise reduction and filtering methods to remove unnecessary data out of the measurements; however, each filtering method can have side effects such as lags or truncation of peaks. The measurement noises usually actuate with high frequencies at the rig. Therefore, using a low-pass filter can attenuate the components of the data above the cut-off frequency. In addition, moving average can be used to smooth out short-term fluctuations.

Using a low-pass filter, one of the important parameters, which affects the filtering output significantly is the break frequency, the frequency at which the data with lower frequency is desirable and the larger frequencies are considered to be noises. The break frequency can be set based on the nature of testing machine and natural frequencies of parts collaborating. The most important frequencies are the wheel and roller rotation frequencies. Based on the angular velocity of the wheel and roller, the rotational frequency of them can be calculated by diving the revolution per minute (RPM) by 60. The Fast Fourier transform (FFT) analysis gives a good grasp of the frequencies existing in the measurements. To eliminate the high-frequency content that is not of interest to this study, we filter the data with a low-pass filter. The break frequency is set close to the wheel rotational frequency.

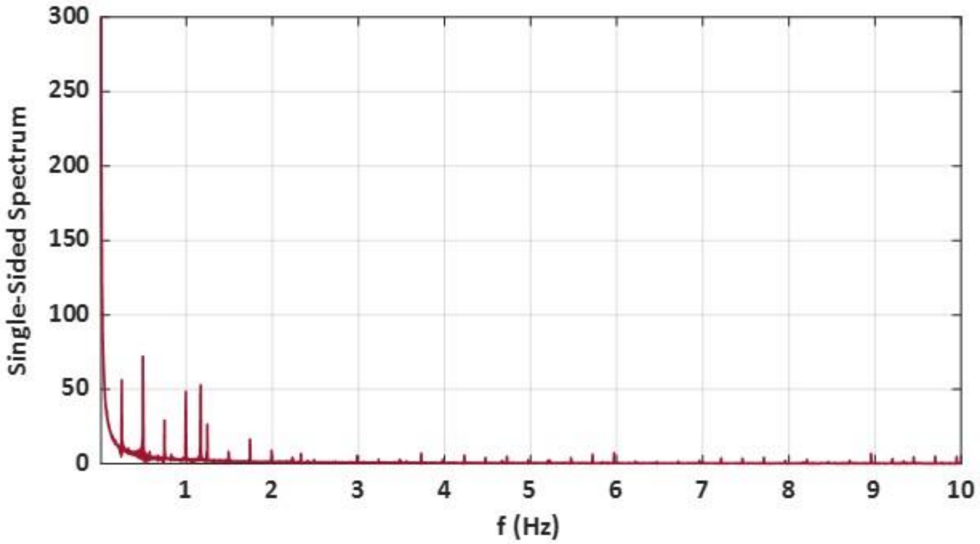

Figure 3.7 Sample FFT Analysis of Measured Longitudinal Force

Figure 3.7 shows a sample FFT analysis on the measured longitudinal force. As shown in the figure, the single-sided spectrum is dominant in the range of roller rotational frequency. Note that there are some other components at higher frequencies that are estimated to be caused by dynamics other than the wheel and roller's rotation.

To smooth out the measurement curves, a moving average function is applied to the filtered data. For the moving average, each data point is replaced by the average of a predefined number of data points forward or rearward of the specific data point. This would have a similar effect as a low pass filter. Because of the moving average, the resulting data profile is shortened by the size of the window. Therefore, it is needed to center the profile to agree with the initial measurement.

4. Formulation of the High Frequency Dynamics at Contact and its Evaluation on the Roller Rig

4.1. Introduction

Commonly, wheel-rail contact models are based on the relationship between creep forces and creepage. They do not consider the dynamic interaction between the two bodies [48]. The local deformation of the contact patch can be related to the friction. Therefore, the forward and angular velocities that are oscillating with an opposite phase, causing a high-frequency dynamic that has been studied [48]. In this section, the high frequencies at wheel-roller contact on the VT-FRA roller rig are calculated, and the dependency of the high frequency dynamics on material, geometry, and normal load is evaluated.

The dynamics of rolling motion of the wheel and roller is derived, and the equations of motion for both the wheel and roller are presented. The wheel-rail contact can be modeled as a spring with a specific stiffness constant depending on the normal force, radius, and module of elasticity. Then, the equations of motion are decoupled, and the high frequency is evaluated. Most of the equations and explanations are as a result of discussions with Dr.ir. Edwin A.H. Vollebregt [49].

4.2. Dynamics of Rolling Motion

4.2.1. Dynamical Model

Figure 4.1 shows the free body diagram of the roller rig in traction mode. F_x is the contact force between the wheel and the roller. In the braking mode, the direction of contact forces on these two rotating bodies are reversed.

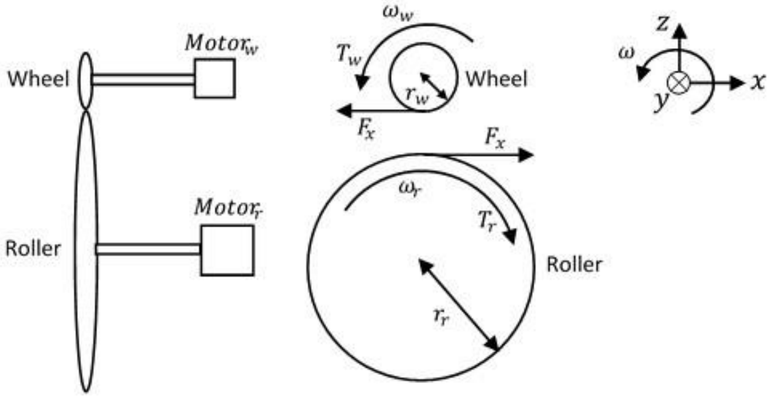

Figure 4.1 Free Body Diagram of the Wheel and the Roller in Traction Mode

According to the free body diagram of the system, equations of motion for the wheel and the roller in the traction mode are presented in equation (4-1). No damping or energy losses are considered at contact.

$$\begin{cases} I_w \dot{\omega}_w = T_w(t) - r_w F_x - C_w \omega_w \\ I_r \dot{\omega}_r = T_r(t) + r_r F_x - C_r \omega_r \end{cases} \tag{4-1}$$

where subscripts w and r denote to the wheel and the roller, respectively. T_w and T_r are the torques exerted on the axles, ω_w and ω_r are the angular velocities, r_w and r_r are the radii and I_w and I_r are the moments of inertia of the wheel and the roller. The terms $C\omega$ describes frictional losses.

The contact force F_x is assumed to be proportional to the amount of the elastic deformation in and around the contact zone. While in traction mode, the velocity of the wheel is more than the roller at contact, i.e., the wheel travels more distance than the roller. Therefore, the contact force F_x can be modeled as a spring, expressed in equation (4-2).

$$F_x = K_x\big((r_w\theta_w + d_x) - r_r\theta_r\big) = K_x(r_w\theta_w - r_r\theta_r + d_x) \tag{4-2}$$

Here the term d_x is the total slipped distance caused by the creepage between the wheel and the roller. The factor K_x is a constant of proportionality, describing the stiffness of the surface. Ignoring the slippage, the contact force equation reduces to the equation (4-3).

$$F_x = K_x(r_w\theta_w - r_r\theta_r) \tag{4-3}$$

Substituting the equation (4-3) into equation (4-1), the equation of motion leads to equation (4-4).

$$\begin{cases} I_w \dot{\omega}_w + K_x(r_w^2\theta_w - r_w r_r \theta_r) + C_w \omega_w = T_w(t) \\ I_r \dot{\omega}_r + K_x(-r_w r_r \theta_w + r_r^2 \theta_r) + C_r \omega_r = T_r(t) \end{cases} \tag{4-4}$$

Equation (4-4) can be further written as a function of θ. Considering $\omega = \dot{\theta}$ and $\dot{\omega} = \ddot{\theta}$, the equations of motion can be presented in the form of equation (4-5).

$$\begin{cases} I_w \ddot{\theta}_w + C_w \dot{\theta}_w + K_x(r_w^2\theta_w - r_w r_r \theta_r) = T_w(t) \\ I_r \ddot{\theta}_r + C_r \dot{\theta}_r + K_x(-r_w r_r \theta_w + r_r^2 \theta_r) = T_r(t) \end{cases} \tag{4-5}$$

Putting the equation (4-5) in a matrix form, the equation (4-6) will be derived.

$$M\ddot{x} + C\dot{x} + Kx = f \tag{4-6}$$

where $x = \begin{bmatrix} \theta_w \\ \theta_r \end{bmatrix}, f = \begin{bmatrix} T_w(t) \\ T_r(t) \end{bmatrix}, M = \begin{bmatrix} I_w & 0 \\ 0 & I_r \end{bmatrix}, C = \begin{bmatrix} C_w & 0 \\ 0 & C_r \end{bmatrix}, K = K_x \begin{bmatrix} r_w^2 & -r_w r_r \\ -r_w r_r & r_r^2 \end{bmatrix}$

4.2.2. Decoupling the Equations

In this section, the equations of motion are decoupled to calculate the eigenfrequencies and eigenvectors of the system. To decouple the equations, the mass normalized damping, $\tilde{C}$, and stiffness, $\widetilde{K}$, matrices should be calculated. Equations (4-7) provide the calculation of the mass normalized damping matrix.

$$\tilde{C} = M^{-\frac{1}{2}} C M^{-\frac{1}{2}} = \begin{bmatrix} I_w^{-\frac{1}{2}} & 0 \\ 0 & I_r^{-\frac{1}{2}} \end{bmatrix} \begin{bmatrix} C_w & 0 \\ 0 & C_r \end{bmatrix} \begin{bmatrix} I_w^{-\frac{1}{2}} & 0 \\ 0 & I_r^{-\frac{1}{2}} \end{bmatrix} = \begin{bmatrix} \frac{C_w}{I_w} & 0 \\ 0 & \frac{C_r}{I_r} \end{bmatrix} \qquad \textbf{(4-7)}$$

The mass normalized stiffness matrix, equation (4-8), can be calculated in the same way as the normalized damping matrix.

$$\widetilde{K} = M^{-\frac{1}{2}} K M^{-\frac{1}{2}} = K_x \begin{bmatrix} \frac{r_w^2}{I_w} & -\frac{r_w r_r}{I_r^{\frac{1}{2}} I_w^{\frac{1}{2}}} \\ -\frac{r_w r_r}{I_r^{\frac{1}{2}} I_w^{\frac{1}{2}}} & \frac{r_r^2}{I_r} \end{bmatrix} \qquad \textbf{(4-8)}$$

The eigenfrequencies of the system can be derived based on $\widetilde{K}v = \lambda v$, where v is the eigenvector related to the eigenvalue problem. To calculate the eigenfrequencies, $\det(\widetilde{K} - \lambda I)$ is set to zero.

$$\det(\widetilde{K} - \lambda I) = \begin{vmatrix} K_x \frac{r_w^2}{I_w} - \lambda & -\frac{K_x r_w r_r}{I_r^{\frac{1}{2}} I_w^{\frac{1}{2}}} \\ -\frac{K_x r_w r_r}{I_r^{\frac{1}{2}} I_w^{\frac{1}{2}}} & K_x \frac{r_r^2}{I_r} - \lambda \end{vmatrix} = \frac{\lambda^2}{K_x} - \lambda \left(\frac{r_w^2}{I_w} + \frac{r_r^2}{I_r} \right) = 0 \qquad \textbf{(4-9)}$$

Based on equation (4-9), the eigenfrequencies of the system can be calculated. The frequencies are shown in equation (4-11).

$$\xrightarrow{yields} \lambda_1 = 0 \; and \; \lambda_2 = K_x \left(\frac{r_w^2}{I_w} + \frac{r_r^2}{I_r} \right) \qquad \textbf{(4-10)}$$

$$\xrightarrow{yields} \omega_1 = 0 \; and \; \omega_2 = \sqrt{K_x \left(\frac{r_w^2}{I_w} + \frac{r_r^2}{I_r} \right)} \; {rad}/{s} \qquad \textbf{(4-11)}$$

Therefore, the so-called high frequency is derived in equation (4-12).

$$f = \frac{1}{2\pi} \sqrt{K_x \left(\frac{r_w^2}{I_w} + \frac{r_r^2}{I_r} \right)} \; Hz \qquad \textbf{(4-12)}$$

The contact stiffness is a function of the material property. The equation (4-12) indicates that the high frequency depends on the contact bodies geometries and also material properties.

After calculating the eigenfrequencies, the eigenvectors related to each eigenfrequency can be calculated based on $\widetilde{K}v = \lambda v$ equation mentioned before. For the first natural frequency, which is related to the rigid motion, the first eigenvector is derived, normalized, and shown in equation (4-13).

$$\lambda_1 = 0 \Rightarrow \begin{bmatrix} K_x \dfrac{r_w^2}{I_w} - 0 & -\dfrac{K_x r_w r_r}{I_r^{\frac{1}{2}} I_w^{\frac{1}{2}}} \\ -\dfrac{K_x r_w r_r}{I_r^{\frac{1}{2}} I_w^{\frac{1}{2}}} & K_x \dfrac{r_r^2}{I_r} - 0 \end{bmatrix} v_1 = \begin{bmatrix} 0 \\ 0 \end{bmatrix} \Rightarrow v_1 = \frac{1}{\sqrt{r_r^2 I_w + r_w^2 I_r}} \begin{bmatrix} r_r I_w^{\frac{1}{2}} \\ r_w I_r^{\frac{1}{2}} \end{bmatrix} \tag{4-13}$$

The second eigenvector, v_2, is related to the high frequency term, and can be calculated in the same way as equation (4-13). Equation (4-14) shows the normalized eigenvector related to the predefined high frequency.

$$\begin{gathered} \lambda_2 = K_x \left(\frac{r_w^2}{I_w} + \frac{r_r^2}{I_r} \right) \\ \Rightarrow \begin{bmatrix} K_x \dfrac{r_w^2}{I_w} - K_x \left(\dfrac{r_w^2}{I_w} + \dfrac{r_r^2}{I_r} \right) & -\dfrac{K_x r_w r_r}{I_r^{\frac{1}{2}} I_w^{\frac{1}{2}}} \\ -\dfrac{K_x r_w r_r}{I_r^{\frac{1}{2}} I_w^{\frac{1}{2}}} & K_x \dfrac{r_r^2}{I_r} - K_x \left(\dfrac{r_w^2}{I_w} + \dfrac{r_r^2}{I_r} \right) \end{bmatrix} v_2 = \begin{bmatrix} 0 \\ 0 \end{bmatrix} \\ \Rightarrow v_2 = \frac{1}{\sqrt{r_r^2 I_w + r_w^2 I_r}} \begin{bmatrix} -r_w I_r^{\frac{1}{2}} \\ r_r I_w^{\frac{1}{2}} \end{bmatrix} \end{gathered} \tag{4-14}$$

Therefore, the matrix of eigenvectors, P, will be the following equation (4-15).

$$\begin{gathered} P = [v_1 \quad v_2] \\ \Rightarrow P = \frac{1}{\sqrt{r_r^2 I_w + r_w^2 I_r}} \begin{bmatrix} r_r I_w^{\frac{1}{2}} & -r_w I_r^{\frac{1}{2}} \\ r_w I_r^{\frac{1}{2}} & r_r I_w^{\frac{1}{2}} \end{bmatrix} \end{gathered} \tag{4-15}$$

According to the VT-FRA roller rig specifications mentioned in

Table 4.1, the matrix of eigenvectors for the rig can be evaluated.

$$\boldsymbol{P} = \frac{1}{\sqrt{r_r^2 I_w + r_w^2 I_r}} \begin{bmatrix} r_r I_w^{\frac{1}{2}} & -r_w I_r^{\frac{1}{2}} \\ r_w I_r^{\frac{1}{2}} & r_r I_w^{\frac{1}{2}} \end{bmatrix} = \begin{bmatrix} 0.1688 & -0.9856 \\ 0.9856 & 0.1688 \end{bmatrix} \tag{4-16}$$

Table 4.1 VT-FRA Roller Rig Wheel and Roller Specification

PARAMETER	SYMBOL	VALUE
Wheel Radius (mm)	$\mathrm{r_w}$	120.4
Roller Radius (mm)	$\mathrm{r_r}$	561.3
Wheel Moment of Inertia $(kg.m^2)$	$\mathrm{I_w}$	0.13
Roller Moment of Inertia $(kg.m^2)$	$\mathrm{I_r}$	96.3

The VT-FRA roller rig eigenvectors are shown in Figure 4.2.

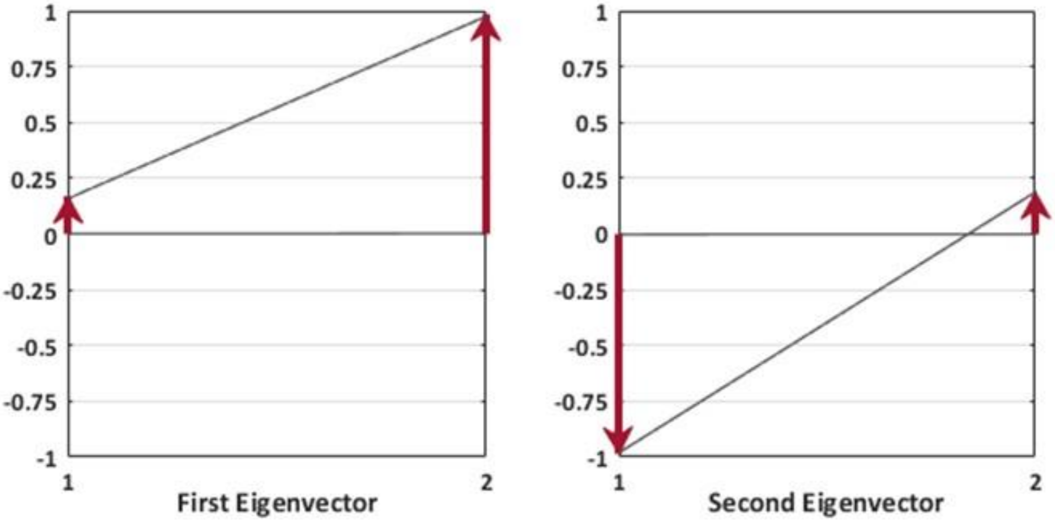

Figure 4.2 VT-FRA Roller Rig Eigenvectors

The damping matrix can be transformed using the calculated matrix of eigenvectors.

$$
\begin{aligned}
P^T\tilde{C}P &= \frac{1}{r_r^2 I_w + r_w^2 I_r}\begin{bmatrix} r_r I_w^{\frac{1}{2}} & r_w I_r^{\frac{1}{2}} \\ -r_w I_r^{\frac{1}{2}} & r_r I_w^{\frac{1}{2}} \end{bmatrix}\begin{bmatrix} \frac{C_w}{I_w} & 0 \\ 0 & \frac{C_r}{I_r} \end{bmatrix}\begin{bmatrix} r_r I_w^{\frac{1}{2}} & -r_w I_r^{\frac{1}{2}} \\ r_w I_r^{\frac{1}{2}} & r_r I_w^{\frac{1}{2}} \end{bmatrix} \\
&= \frac{1}{r_r^2 I_w + r_w^2 I_r}\begin{bmatrix} C_w r_r^2 + C_r r_w^2 & -\frac{C_w r_w r_r I_r^{\frac{1}{2}}}{I_w^{\frac{1}{2}}} + \frac{C_r r_w r_r I_w^{\frac{1}{2}}}{I_r^{\frac{1}{2}}} \\ -\frac{C_w r_w r_r I_r^{\frac{1}{2}}}{I_w^{\frac{1}{2}}} + \frac{C_r r_w r_r I_w^{\frac{1}{2}}}{I_r^{\frac{1}{2}}} & \frac{C_w r_w^2 I_r}{I_w} + \frac{C_r r_r^2 I_w}{I_r} \end{bmatrix}
\end{aligned}
\tag{4-17}
$$

$P^T\widetilde{C}P$ should be diagonal. However, it seems that the off-diagonal terms are too small and can be ignored. To simplify the equations, we define the term C and assume that

$$C = \frac{C_w}{I_w} = \frac{C_r}{I_r}.$$

This assumption causes off-diagonal terms of damping matrix to go to zero. The transformed damping matrix is simplified in equation (4-18).

$$P^T\tilde{C}P = \begin{bmatrix} C & 0 \\ 0 & C \end{bmatrix} \tag{4-18}$$

Similarly, the stiffness matrix can be transformed according to:

$$
\begin{aligned}
&P^T\widetilde{K}P \\
&= \frac{K_x}{r_r^2 I_w + r_w^2 I_r}\begin{bmatrix} r_r I_w^{\frac{1}{2}} & r_w I_r^{\frac{1}{2}} \\ -r_w I_r^{\frac{1}{2}} & r_r I_w^{\frac{1}{2}} \end{bmatrix}\begin{bmatrix} \frac{r_w^2}{I_w} & -r_w r_r I_r^{-\frac{1}{2}} I_w^{-\frac{1}{2}} \\ -r_w r_r I_r^{-\frac{1}{2}} I_w^{-\frac{1}{2}} & \frac{r_r^2}{I_r} \end{bmatrix}\begin{bmatrix} r_r I_w^{\frac{1}{2}} & -r_w I_r^{\frac{1}{2}} \\ r_w I_r^{\frac{1}{2}} & r_r I_w^{\frac{1}{2}} \end{bmatrix} \\
&= K_x\begin{bmatrix} 0 & 0 \\ 0 & \frac{r_w^2}{I_w} + \frac{r_r^2}{I_r} \end{bmatrix} = \begin{bmatrix} \lambda_1 & 0 \\ 0 & \lambda_2 \end{bmatrix} = \begin{bmatrix} \omega_1^2 & 0 \\ 0 & \omega_2^2 \end{bmatrix}
\end{aligned}
\tag{4-19}
$$

The transformed stiffness matrix shown in equation (4-19) is diagonal, and the diagonal terms are the eigenfrequencies. To transform the forcing function, equation (4-20), the same steps can be taken.

$$
\begin{aligned}
F(t) = P^T M^{-\frac{1}{2}} f &= \frac{1}{\sqrt{r_r^2 I_w + r_w^2 I_r}} \begin{bmatrix} r_r I_w^{\frac{1}{2}} & r_w I_r^{\frac{1}{2}} \\ -r_w I_r^{\frac{1}{2}} & r_r I_w^{\frac{1}{2}} \end{bmatrix} \begin{bmatrix} I_w^{-\frac{1}{2}} & 0 \\ 0 & I_r^{-\frac{1}{2}} \end{bmatrix} \begin{bmatrix} T_w(t) \\ T_r(t) \end{bmatrix} \\
&= \frac{1}{\sqrt{r_r^2 I_w + r_w^2 I_r}} \begin{bmatrix} r_r T_w + r_w T_r \\ -r_w \frac{I_r^{\frac{1}{2}}}{I_w^{\frac{1}{2}}} T_w + r_r \frac{I_w^{\frac{1}{2}}}{I_r^{\frac{1}{2}}} T_r \end{bmatrix}
\end{aligned} \tag{4-20}
$$

Transforming the damping, stiffness, and forcing function enable us to write the decoupled equations of motion in the new coordinate system. The decoupled equations are presented in equation (4-21).

$$
\begin{cases}
\ddot{r}_1(t) + C\dot{r}_1(t) = \dfrac{r_r T_w + r_w T_r}{\sqrt{r_r^2 I_w + r_w^2 I_r}} \\[2ex]
\ddot{r}_2(t) + C\dot{r}_2(t) + K_x\left(\dfrac{r_w^2}{I_w} + \dfrac{r_r^2}{I_r}\right) r_2(t) = \dfrac{-r_w \frac{I_r^{\frac{1}{2}}}{I_w^{\frac{1}{2}}} T_w + r_r \frac{I_w^{\frac{1}{2}}}{I_r^{\frac{1}{2}}} T_r}{\sqrt{r_r^2 I_w + r_w^2 I_r}}
\end{cases} \tag{4-21}
$$

where $r_1(t)$ and $r_2(t)$ are the first and second decoupled modal equations, respectively. Considering zero initial conditions, the decoupled system is solved and presented in equations (4-22) and (4-23).

$$
r_1(t) = \frac{1}{C^2} \frac{r_r T_w + r_w T_r}{\sqrt{r_r^2 I_w + r_w^2 I_r}} \left(e^{-Ct} + Ct - 1\right) \tag{4-22}
$$

$$
r_2(t) = a\left(-\left(\frac{1}{2} - \frac{\frac{C}{4}}{b}\right) e^{-\left(b+\frac{C}{2}\right)t} - \left(\frac{1}{2} + \frac{\frac{C}{4}}{b}\right) e^{\left(b-\frac{C}{2}\right)t} + 1\right) \tag{4-23}
$$

where

$$
a = \frac{1}{K_x\left(\frac{r_w^2}{I_w} + \frac{r_r^2}{I_r}\right)} \left(\frac{-r_w \frac{I_r^{\frac{1}{2}}}{I_w^{\frac{1}{2}}} T_w + r_r \frac{I_w^{\frac{1}{2}}}{I_r^{\frac{1}{2}}} T_r}{\sqrt{r_r^2 I_w + r_w^2 I_r}} \right) \tag{4-24}
$$

$$
b = \sqrt{\left(\frac{C}{2}\right)^2 - K_x\left(\frac{r_w^2}{I_w} + \frac{r_r^2}{I_r}\right)} \tag{4-25}
$$

With $r(t)$ known, the physical solution can be recovered using the inverse transform.

$$x(t) = M^{-\frac{1}{2}}\,\mathrm{Pr}(t) = \frac{1}{\sqrt{r_r^2 I_w + r_w^2 I_r}} \begin{bmatrix} I_w^{-\frac{1}{2}} & 0 \\ 0 & I_r^{-\frac{1}{2}} \end{bmatrix} \begin{bmatrix} r_r I_w^{\frac{1}{2}} & -r_w I_r^{\frac{1}{2}} \\ r_w I_r^{\frac{1}{2}} & r_r I_w^{\frac{1}{2}} \end{bmatrix} \begin{bmatrix} r_1(t) \\ r_2(t) \end{bmatrix} \tag{4-26}$$

4.2.3. State Space Formulation

The second-order system defined in equation (4-6) can be expanded into a first-order system. The equations can be rewritten as the equation (4-28).

$$\begin{cases} \omega_w = \dot{\theta}_w \\ \omega_r = \dot{\theta}_r \\ I_w \dot{\omega}_w = -K_x(r_w^2 \theta_w - r_w r_r \theta_r) - C_w \omega_w + T_w(t) \\ I_r \dot{\omega}_r = -K_x(-r_w r_r \theta_w + r_r^2 \theta_r) - C_r \omega_r + T_r(t) \end{cases} \tag{4-27}$$

$$D\frac{dy}{dt} = Ay + f \tag{4-28}$$

Where

$$y = y(t) = \begin{bmatrix} \theta_w \\ \theta_r \\ \omega_w \\ \omega_r \end{bmatrix}, D = \begin{bmatrix} 1 & 0 & 0 & 0 \\ 0 & 1 & 0 & 0 \\ 0 & 0 & I_w & 0 \\ 0 & 0 & 0 & I_r \end{bmatrix},$$
$$A = \begin{bmatrix} 0 & 0 & 1 & 0 \\ 0 & 0 & 0 & 1 \\ -r_w^2 K_x & r_w r_r K_x & -C_w & 0 \\ r_w r_r K_x & -r_r^2 K_x & 0 & -C_r \end{bmatrix}, f = \begin{bmatrix} 0 \\ 0 \\ T_w(t) \\ T_r(t) \end{bmatrix} \tag{4-29}$$

With $y(0) = 0$.

It is a forced system that has homogeneous and particular solutions. For the homogeneous solution, f is assumed to be zero, and the solution is considered to be $ce^{\lambda t}$. Substituting the solution in the equation (4-28), the following equations and are derived.

$$y = ce^{\lambda t} \tag{4-30}$$

$$D\lambda c e^{\lambda t} = Ace^{\lambda t} \rightarrow D^{-1}A = \lambda \tag{4-31}$$

To get the eigenfrequencies of the system, $\det(D^{-1}A - \lambda I)$ should be equal to zero.

$$\begin{vmatrix} -\lambda & 0 & 1 & 0 \end{vmatrix} \tag{4-32}$$

$$
\begin{aligned}
\Rightarrow \det(D^{-1}A-\lambda I)& \\
&= -\lambda\left(-\lambda\left(\frac{C_w}{I_w}+\lambda\right)\left(\frac{C_r}{I_r}+\lambda\right)-\left(\frac{C_w}{I_w}+\lambda\right)\left(\frac{r_r^2K_x}{I_r}\right)\right) \\
&\quad+\lambda\left(\left(\frac{r_w^2K_x}{I_w}\right)\left(\frac{C_r}{I_r}+\lambda\right)\right)+\left(\frac{r_w^2K_x}{I_w}\right)\left(\frac{r_r^2K_x}{I_r}\right) \\
&\quad-\left(\frac{r_wr_rK_x}{I_w}\right)\left(\frac{r_wr_rK_x}{I_r}\right)
\end{aligned}
$$

Defining

$$
K_{xw}=\frac{K_x}{I_w},K_{xr}=\frac{K_x}{I_r},C'_w=\frac{C_w}{I_w},C'_r=\frac{C_r}{I_r} \tag{4-33}
$$

The equation (4-32) simplifies to equation (4-34).

$$
\begin{aligned}
\det(D^{-1}A-\lambda I)& \\
&=\lambda^4+(C'_w+C'_r)\lambda^3+(C'_wC'_r+r_r^2K_{xr}+r_w^2K_{xw})\lambda^2 \\
&\quad+(r_r^2K_{xr}C'_w+r_w^2K_{xw}C'_r)\lambda
\end{aligned} \tag{4-34}
$$

4.2.4. Undamped Solution

Assuming no damping, we can re-write equation (4-34) as

$$
\det\left(D^{-1}A-\lambda I\right)=\lambda^4+\left(r_r^2K_{xr}+r_w^2K_{xw}\right)\lambda^2=0 \tag{4-35}
$$

The roots of equation (4-35) are the eigenfrequencies of the system.

$$
\lambda_{1,2}=0,\lambda_{3,4}=\pm i\sqrt{K_x\left(\frac{r_r^2}{I_r}+\frac{r_w^2}{I_w}\right)} \tag{4-36}
$$

The eigenfrequencies of the motion are obtained as $\bar{\lambda}=|\lambda_3|\ rad/s$ and $f_{rock}=\frac{\bar{\lambda}}{2\pi}\ Hz$

4.2.5. Damped Solution

When damping is present, equation (4-34) yields

$$
\lambda_1=0, \tag{4-37}
$$

which represents the rigid body dynamics. We additionally have

$$
\begin{aligned}
\lambda^3+\left(C'_w+C'_r\right)\lambda^2+\left(C'_wC'_r+r_r^2K_{xr}+r_w^2K_{xw}\right)\lambda& \\
+\left(r_r^2K_{xr}C'_w+r_w^2K_{xw}C'_r\right)=0&
\end{aligned} \tag{4-38}
$$

Assuming small damping, the second eigenfrequency should be close to the origin since the undamped system has two eigenfrequencies of zero. Ignoring higher orders of second natural frequency and damping, the second eigenfrequency can be estimated using equation (4-39).

$$\begin{gathered}(r_r^2K_{xr}+r_w^2K_{xw})\lambda_2+(r_r^2K_{xr}C'_w+r_w^2K_{xw}C'_r)=0\\ \Rightarrow\lambda_2=-\frac{\frac{C_w}{r_w^2}+\frac{C_r}{r_r^2}}{\frac{I_w}{r_w^2}+\frac{I_r}{r_r^2}}\end{gathered}\tag{4-39}$$

Introducing the shape factors in equation (4-40), the second eigenfrequency can be written as equation (4-41).

$$\alpha_w=\frac{I_w}{m_wr_w^2},\alpha_r=\frac{I_r}{m_rr_r^2},\bar{r}_w^2=\frac{r_w^2}{I_w}=\frac{1}{\alpha_wm_w}\ and\ \bar{r}_r^2=\frac{r_r^2}{I_r}=\frac{1}{\alpha_rm_r}\tag{4-40}$$

$$\lambda_2=-\frac{\frac{C_w}{r_w^2}+\frac{C_r}{r_r^2}}{\frac{I_w}{r_w^2}+\frac{I_r}{r_r^2}}=-\frac{\frac{C_w}{r_w^2}+\frac{C_r}{r_r^2}}{\alpha_wm_w+\alpha_rm_r}\tag{4-41}$$

To derive the third and fourth eigenfrequencies, equation (4-38) is simplified and solved for the third and fourth eigenfrequencies:

$$\lambda^2+\left(C^{'}_w+C^{'}_r\right)\lambda+\left(\bar{r}_r^2K_x+\bar{r}_w^2K_x\right)=0\tag{4-42}$$

$$\begin{aligned}\lambda_{3,4}&=-\frac{C^{'}_w+C^{'}_r}{2}\pm i\sqrt{K_x\left(\frac{r_w^2}{I_w}+\frac{r_r^2}{I_r}\right)}\\&=-\frac{C^{'}_w+C^{'}_r}{2}\pm i\sqrt{K_x\left(\frac{1}{\alpha_wm_w}+\frac{1}{\alpha_rm_r}\right)}\end{aligned}\tag{4-43}$$

The $\lambda_{3,4}$ terms describe the oscillatory motion at high frequency.

4.3. Estimating the Contact Stiffness K_x

The linear relationship between the force and linear displacement can be written as $F_x=K_x\delta_x$. For circular contact and equal materials assuming Hertzian loading, the contact stiffness can be calculated using equation (4-44) [50].

$$K_x=\frac{F_x}{\delta_x}=\frac{4aG}{2-\upsilon}=\frac{2aE}{(2-\nu)(1+\nu)}\tag{4-44}$$

The (4-44) formula is derived based on displacement measurements at different loadings, F_x, and material properties [51]. For circular contact and based on Hertzian theory, the following parameters can be defined by assuming the contact occurs between a sphere of radius $r^*$and a flat plane.

$$a=\sqrt{r^*\delta_n}, F_n=\frac{4}{3}E^*(r^*)^{\frac{1}{2}}\delta_n^{\frac{3}{2}}, r^*=\frac{1}{\frac{1}{r_1}+\frac{1}{r_2}}, E^*=\frac{E}{2(1-\nu^2)}, \qquad \textbf{(4-45)}$$

where a and F_n are resulting contact area and vertical loading, respectively. Using equation (4-45) and eliminating δ_n, we can formulate the contact area as

$$a=\left(\frac{3F_n r^*(1-\nu^2)}{2E}\right)^{\frac{1}{3}} \qquad \textbf{(4-46)}$$

The contact stiffness formula can be written as

$$K_x=\frac{2\left(\frac{3F_n r^*(1-\nu^2)}{2E}\right)^{\frac{1}{3}}E}{(2-\nu)(1+\nu)} \qquad \textbf{(4-47)}$$

For steel wheel and steel roller, with Poisson ratio $\nu\approx 0.3$, K_x is approximated as

$$K_x=\frac{2\left(\frac{3F_n r^*\left(1-0.3^2\right)}{2E}\right)^{\frac{1}{3}}E}{(2-0.3)(1+0.3)}\approx\left(F_n r^* E^2\right)^{1/3} \qquad \textbf{(4-48)}$$

4.4. High Frequency Dynamics at Virginia Tech Roller Rig

Based on the VT-FRA roller rig specification and material properties, the shape factors mentioned in equation (4-40) and contact stiffness provided in equation (4-48), the high frequency,

$$f=\frac{1}{2\pi}\sqrt{K_x\left(\frac{1}{\alpha_w m_w}+\frac{1}{\alpha_r m_r}\right)}\ Hz,$$

can be evaluated. The VT-FRA roller rig specification and material properties for the steel wheel and the steel roller are provided in Table 4.2. It is assumed that both the wheel and roller have the same material specifications.

For the wheel and roller, the shape factors are calculated and presented in equations (4-49) and (4-50). The r^* radius presented in equation (4-45) is also needed to evaluate the contact stiffness, which is calculated in (4-51).

$$\alpha_w=\frac{I_w}{m_w r_w^2}=\frac{0.13\times 10^6}{15.6\times 120.4^2}=0.5749 \qquad (4\text{-}49)$$

$$\alpha_r = \frac{I_r}{m_r r_r^2} = \frac{96.3 \times 10^6}{669.5 \times 561.3^2} = 0.4565 \tag{4-50}$$

$$r^* = \frac{1}{\frac{1}{r_1} + \frac{1}{r_2}} = \frac{1}{\frac{1}{r_w} + \frac{1}{r_r}} = \frac{1}{\frac{1}{120.4} + \frac{1}{561.3}} = 99.1\ mm \tag{4-51}$$

Table 4.2 VT-FRA Roller Rig Wheel and Roller Specification and Material Properties

PARAMETER	SYMBOL	VALUE
Wheel Radius (mm)	r_w	120.4
Roller Radius (mm)	r_r	561.3
Simulated Point Contact Radius (mm)	r^*	99.1
Wheel Moment of Inertia $(kg.m^2)$	I_w	0.13
Roller Moment of Inertia $(kg.m^2)$	I_r	96.3
Wheel Weight (kg)	m_w	15.6
Roller Weight (kg)	m_r	669.5
Wheel Shape Factor	α_w	0.5749
Roller Shape Factor	α_r	0.4565
Module of Elasticity (GPa)	E	210
Poisson ratio	υ	0.28

The only other parameter needed to be specified to estimate the high frequency is the normal force, f_n. Assuming a normal force of $9.6\ kN$, we can calculate the contact stiffness and dynamic frequency as:

$$K_x = (F_n r^* E^2)^{\frac{1}{3}} = 3.4748e5\ N/mm \tag{4-52}$$

$$f = \frac{1}{2\pi}\sqrt{K_x\left(\frac{1}{\alpha_w m_w} + \frac{1}{\alpha_r m_r}\right)} = 1005.1\ Hz \tag{4-53}$$

Figure 4.3 shows the dynamic frequency at the wheel-roller contact for a range of normal forces. The frequency abruptly rises for small wheel loads, and the increasing slope slows down for higher wheel loads.

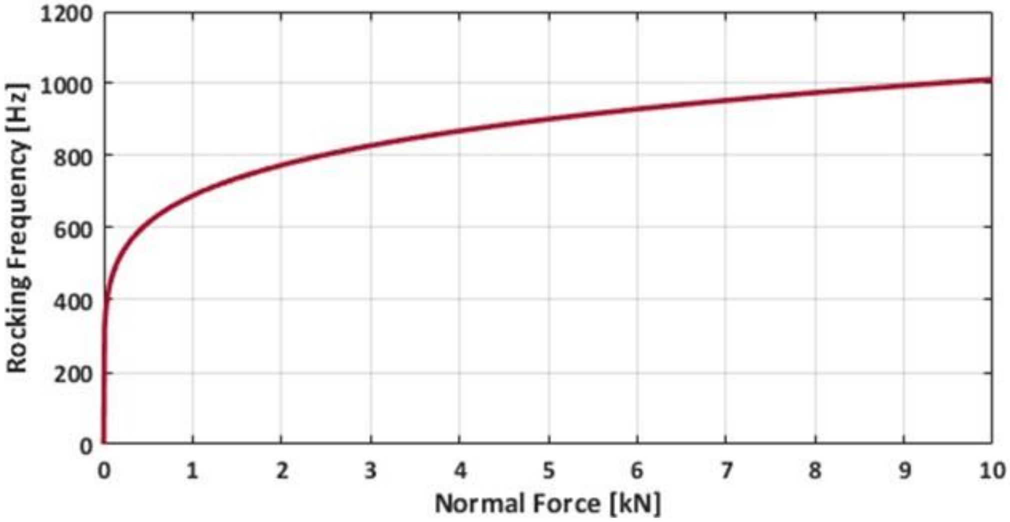

Figure 4.3 High Frequency at the VT-FRA Roller Rig with respect to Normal Force

4.5. Summary

In this chapter, the high frequency dynamics for a roller rig has been formulated, and the effect of several parameters such as normal load, material properties, and geometries is investigated. The equations of motion are derived, decoupled, and presented in the state space mode. The solution of the system indicates rigid motion frequencies along with an oscillating motion characteristic for undamped conditions. Furthermore, the contact stiffness, K_x, is estimated and formulated for bodies with the same material properties. By using the contact stiffness formula and the solution of the equations of motion, the high frequency of the wheel and the roller of the VT-FRA roller rig is evaluated and provided based on the normal force applying at the contact.

5. Evaluation of Simulation Parameters on Wheel-Rail Interface (WRI) Dynamics

5.1. Introduction

In this chapter, the effect of various test parameters on transient traction coefficient behavior is investigated using the VT-FRA roller rig. Running the wheels on each other under a specified vertical load (wheel load) and creepage leads to the generation of worn materials and debris at the running surfaces, causing a significant change in traction coefficient.

A slew of experiments are performed to evaluate the effect of the wheel load, creepage, and angle of attack on traction coefficient and accumulation of third body layers at the contact. The results show that there is a direct correlation between increasing wheel load and creepage and, traction coefficient. The higher the wheel load and % creepage, the faster the traction coefficient increases from its initial value to a plateau that marks the maximum achievable traction for the specific operating condition. Comparing the results for similar maximum tractions indicate that with larger wheel loads and %creepages, the transition to maximum traction occurs in less time due to the higher rate of the natural third-body layer generation.

The parametric study is organized in 4 case studies, in which one factor is changed while the others are maintained at their baseline value. The parameters that are changed are: wheel load, % creepages, and angle of attack (AOA). The % creepages and angle of attack (AOA) are changed in both discrete steps and continuously.

5.2. Case study 1: Wheel Load

Four different experiments are performed to evaluate the effect of wheel load on longitudinal creep forces and traction coefficients. A high value of 2% creepage is considered in order to highlight the effect of load on creep forces and traction coefficient at the contact patch. Wheel loads of 1.5 kN, 2.7 kN, 4.5 kN, and 9.8 kN are considered to cover a range of low to high values for the simulated test rig. In all sets of experiments, the angle of attack and cant angle are set to zero with an accuracy of 0.05-degree, and the field speed is set to 3 km/h. Table 5.1 shows a summary of the test conditions assigned to the experiments. All test conditions are maintained during the experiments using six high-precision linear actuators and two AC motors.

Before each test, both wheel and roller surfaces are cleaned to ensure no worn material, debris, or dust are in contact. A duration of 400 seconds is considered for the experiments to capture transient traction section. An extended period of experiments allows the wheel and roller surfaces to generate enough worn materials and debris at contact for the running surfaces to reach their “steady state” condition. The steady state condition is referred to the condition in which there is not rapid change in traction coefficient with time while the test parameters are kept unchanged. This is in contrast to the “transient” condition for which the traction coefficient changes with time even though the test parameters remain unchanged.

Table 5.1 Test Condition for Wheel Load Study

TEST PARAMETER	VALUE
Wheel Profile	AAR-1B
Roller Profile	US-136 rail
Angle of Attack (°)	0
Cant Angle (°)	0
Field Speed (km/h)	3.0
Rig Wheel Load (kN)	1.5 to 9.8
Full-Scale Wheel Load (kN)	24.0 to 156.8
Commanded Creepage (%)	2.0
Initial Surface Condition	Clean and Dry

Four different experiments were performed to evaluate the effect of wheel load on longitudinal creep forces and traction coefficients based on the test conditions given in Table 5.1. All the experiments were performed at the same test conditions except load. The measured longitudinal and vertical forces are presented in

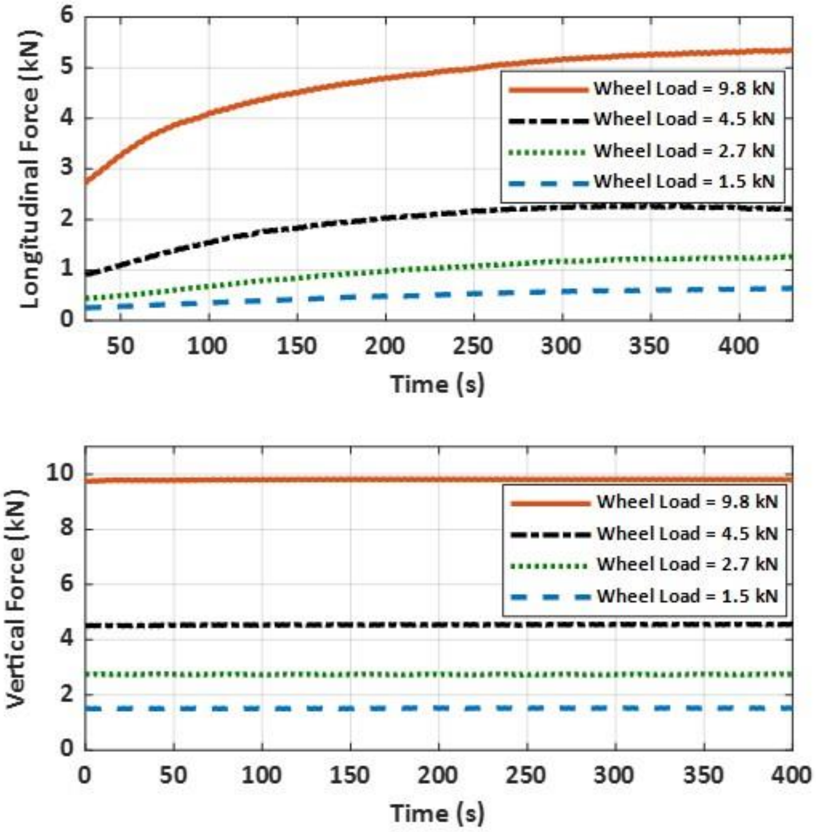

Figure 5.1.

Low longitudinal forces were observed at the beginning of experiments, which the wheel and roller surfaces were clean. For low wheel loads, it seems that the rate of worn material generation at contact is less compared to the experiments with high loads. Therefore, at low wheel loads, the longitudinal forces show lower rates of increase compared to the results of high wheel load experiments such as 9.8 kN.

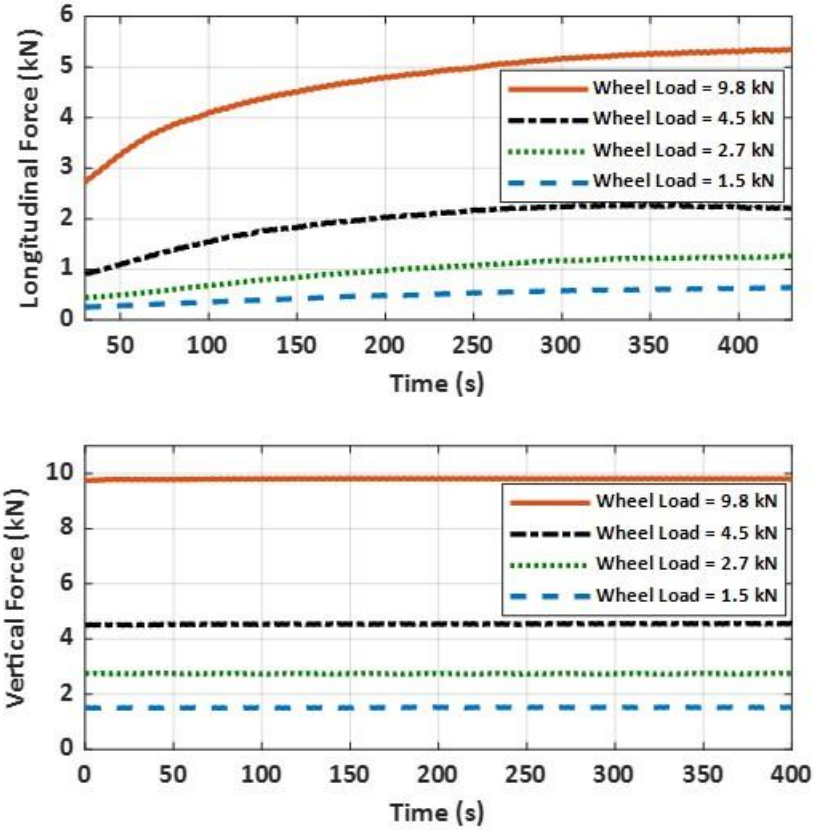

Figure 5.1 Longitudinal and Vertical Forces Measured for Wheel Load Experiments

Figure 5.2 shows two running traces after two different experiments. One on the left hand is cleaned after testing, and the other one is remained unclean containing worn materials and debris. In our case, the third body layer is a grayish powder consisting of debris and steel flakes. It is hypothesized that the powder contains ferrous oxides, which influence the creep forces at contact significantly. Although no chemical composition test was performed on the third body layers, it seems that the oxide is magnetite (Fe_3O_4) due to its color. In the literature, Nakahara [11] claimed that Fe_3O_4 suppress the increase in traction coefficient, and the brownish powder iron oxide (Fe_2O_3) increases the traction. In our case, no brown-color powder is observed, and the residue is gray. It adds to the complexity of the study. It is necessary to perform experiments under highly controlled environment due to the nature of complex contact dynamics.

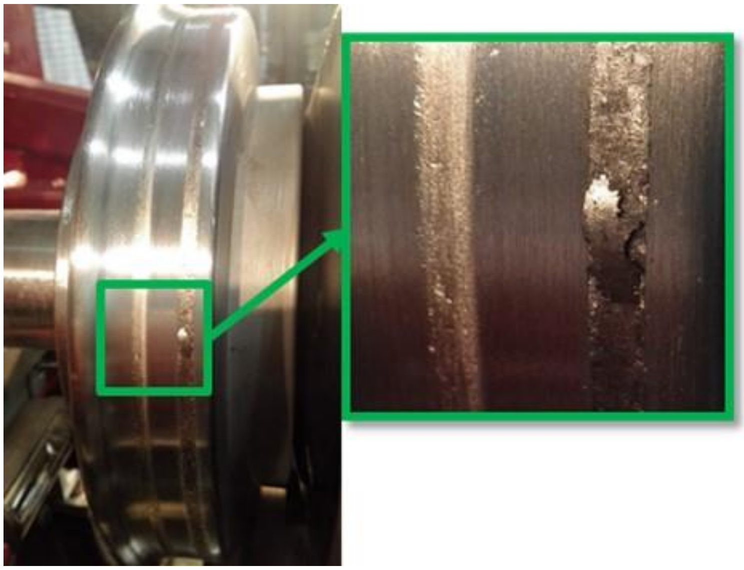

Figure 5.2 Running Traces on the Wheel Surface. Cleaned Surface (Left Trace), Worn Material and Debris (Right Trace)

Based on the creep forces measured at the contact patch, the traction coefficient can be calculated and plotted for all four experiments, shown in Figure 5.3. The following conclusions are reached:

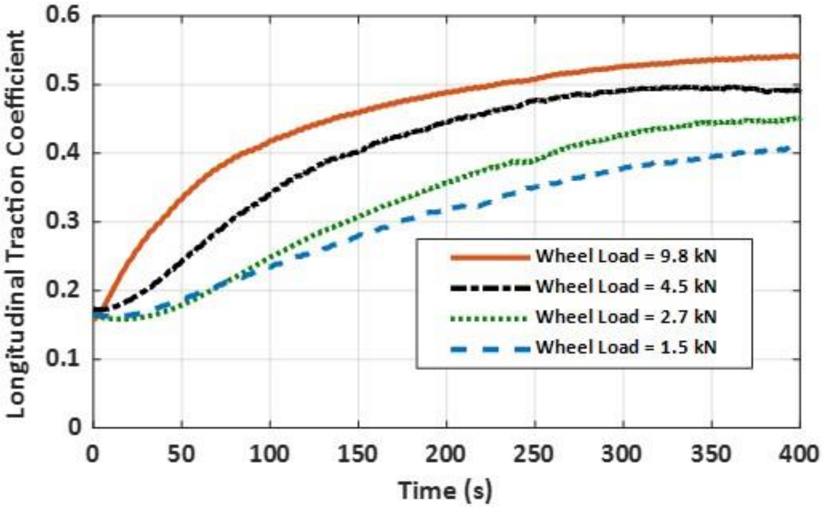

- All curves have almost started at the same traction coefficient level, which means that there is not any relation between traction coefficient and normal contact force at the beginning of the experiments for cleaned surfaces.
- All the curves indicate an increase in traction coefficients during the transition period, at the beginning of the tests

- The traction coefficients have low values at the beginning of the experiments when the wheel and roller surfaces are cleaned
- The traction coefficient increases with time until it reaches steady state
- The time to steady state is inversely proportional to wheel load, % creepage, or both. For higher wheel loads and/or % creepage, steady state condition is reached sooner.

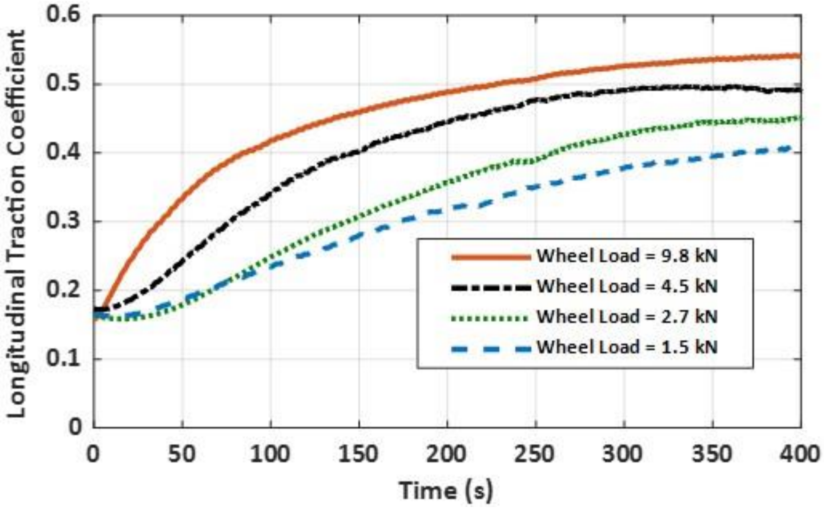

Figure 5.3 Traction Coefficient Behavior for Various Wheel Loads

To study the behavior of transient traction coefficient for wheel load experiments, the real-time measurements of creep forces at contact are analyzed and plotted in

Figure 5.4. As the experiments have almost the same traction coefficient at the beginning, the change in the traction coefficient for all four experiments can be evaluated and compared based on the traction coefficient values.

Figure 5.4 indicates the traction coefficient values at various times—namely, 200, 250, 300, 350, and 400 seconds—measured for the four wheel loads. A shape-preserving curve fit is used for each test condition. The curves show a steeper increase for low wheel loads. All the curves plateau approximately at 9.8 kN, which means that performing experiments with wheel loads, more than 9.8 kN would result in nearly the same transient traction curves.

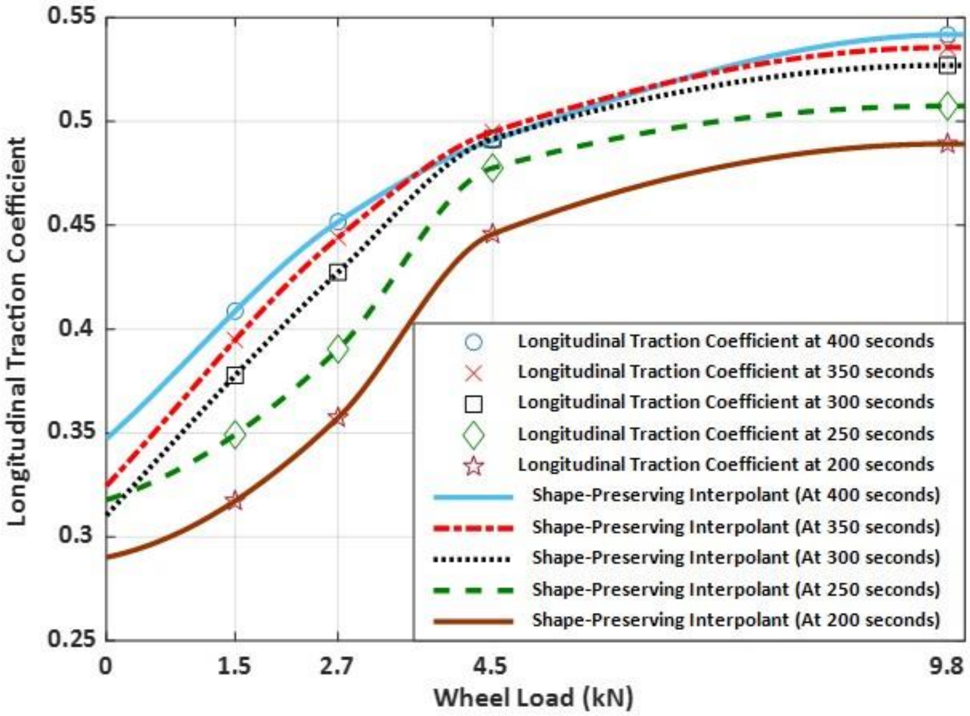

Figure 5.4 Traction Coefficient Values at Several Time Points for All Wheel Load Experiments

5.3. Case Study 2: Discrete Creepage

All creepage set of experiments are conducted at 9.8 kN wheel load (corresponding to a full-scale wheel load of 158 kN or 35 kips) to better compare the results for various creepages. A range of low and high creepages is considered to magnify the effect of creepage on test results. Based on the rig's capabilities, six experiments are performed at 0.06%, 0.13%, 0.25%, 0.50%, 1.00%, and 2.00% creepages. To ensure that cant angle and angle of attack do not have any effect on the test results, all the creepage experiments are performed at zero cant angle and angle of attack. The field speed is kept at 3 km/h for a 1:20 tapered wheel. A summary of test conditions is provided in Table 5.2.

Table 5.2 Test Conditions for Discrete Creepage Study

TEST PARAMETER	VALUE
Wheel Profile	AAR-1B
Roller Profile	US-136 rail
Angle of Attack (°)	0
Cant Angle (°)	0

Field Speed (km/h)	3.0
Rig Wheel Load (kN)	9.8
Full-Scale Wheel Load (kN)	156.8
Commanded Creepage (%)	0.06 to 2.00
Initial Surface condition	Clean and Dry

At the beginning of the experiments, the wheel and roller surfaces are cleaned to ensure that no worn materials or dust are present at the wheel and roller running surfaces. During the experiment, worn materials and debris are generated at the running surfaces, enabling us to record the rising longitudinal creep forces at the contact during the transient period.

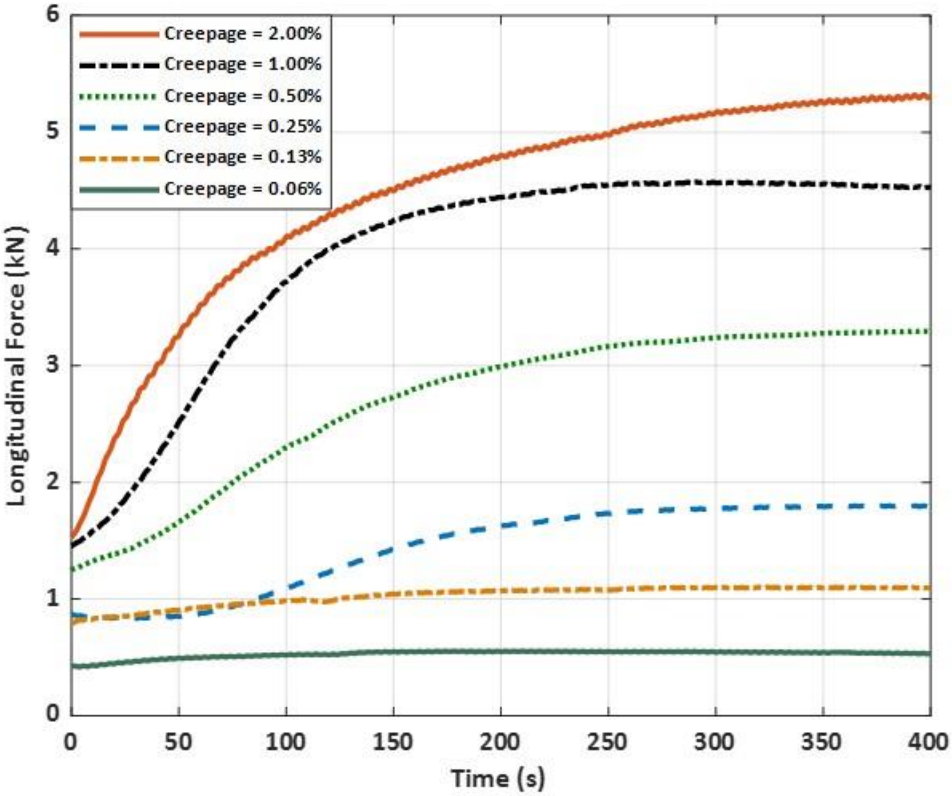

Figure 5.5 shows the longitudinal forces measured during each experiment. For lower %creepages, 0.06% and 0.13%, a smaller rise in traction coefficients is detected, due to the smaller amounts of worn materials accumulated at the contact. As %creepage increases, the difference between the lower and higher traction coefficients significantly increases as a result of more worn materials being generated.

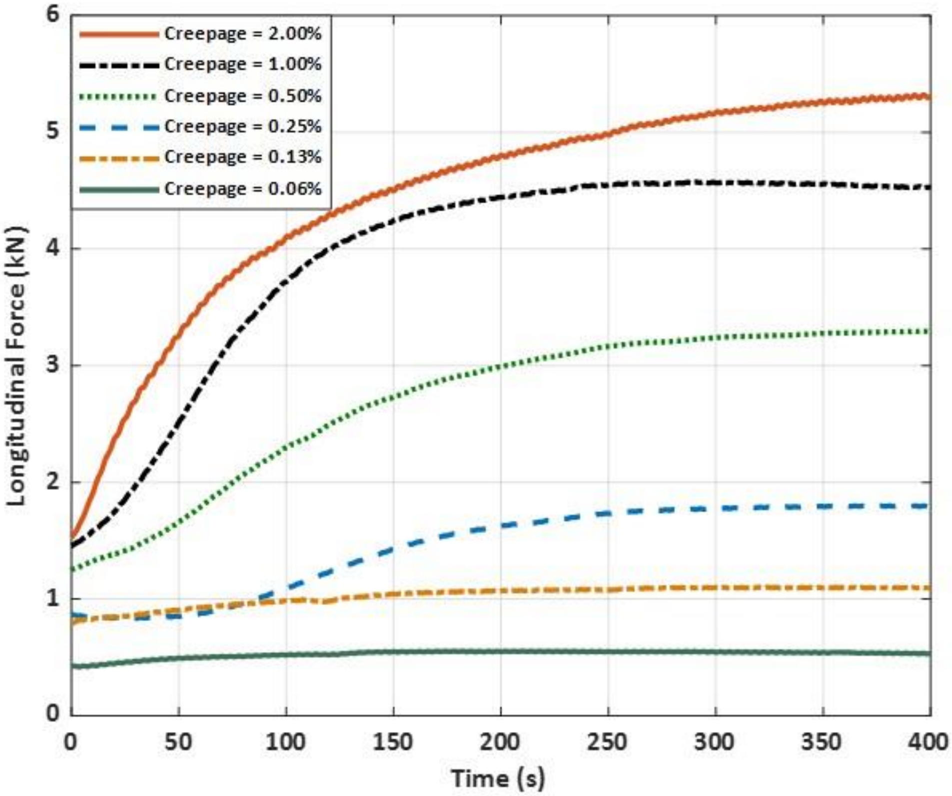

Figure 5.5 Longitudinal Forces Measured for the Creepage-based Experiments

Traction coefficient behaviors can be studied based on the measured creep forces at the contact patch.

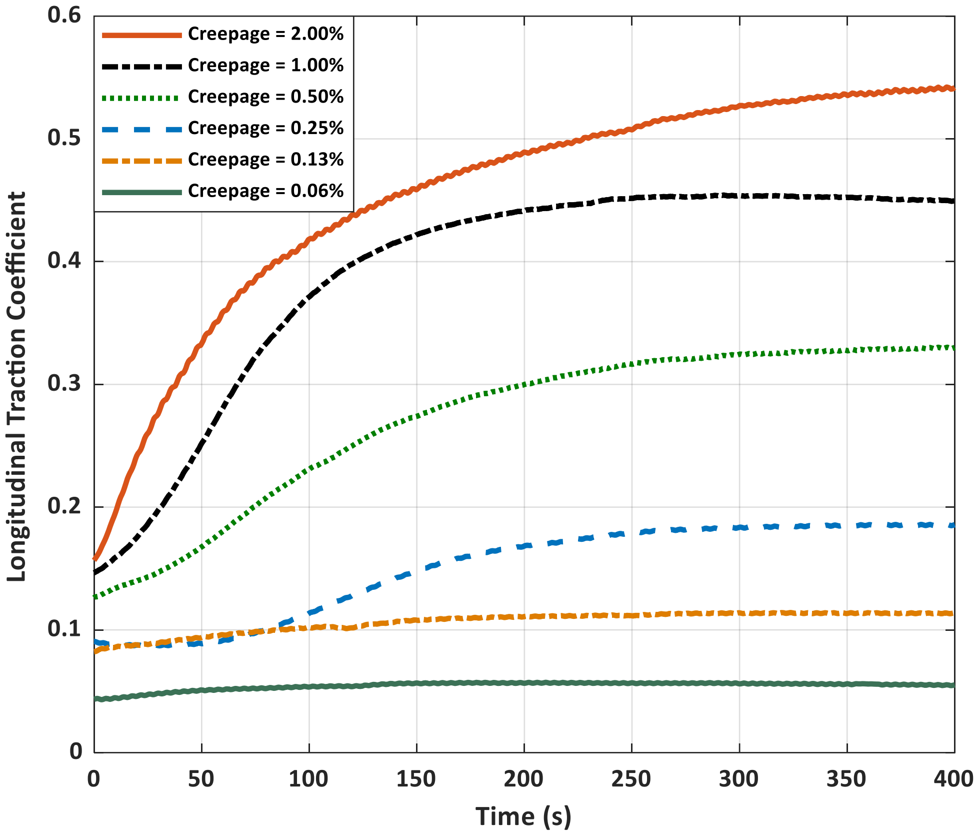

Figure 5.6 shows the calculated traction coefficients for all the experiments. From Figure 5.6, the following observations can be made:

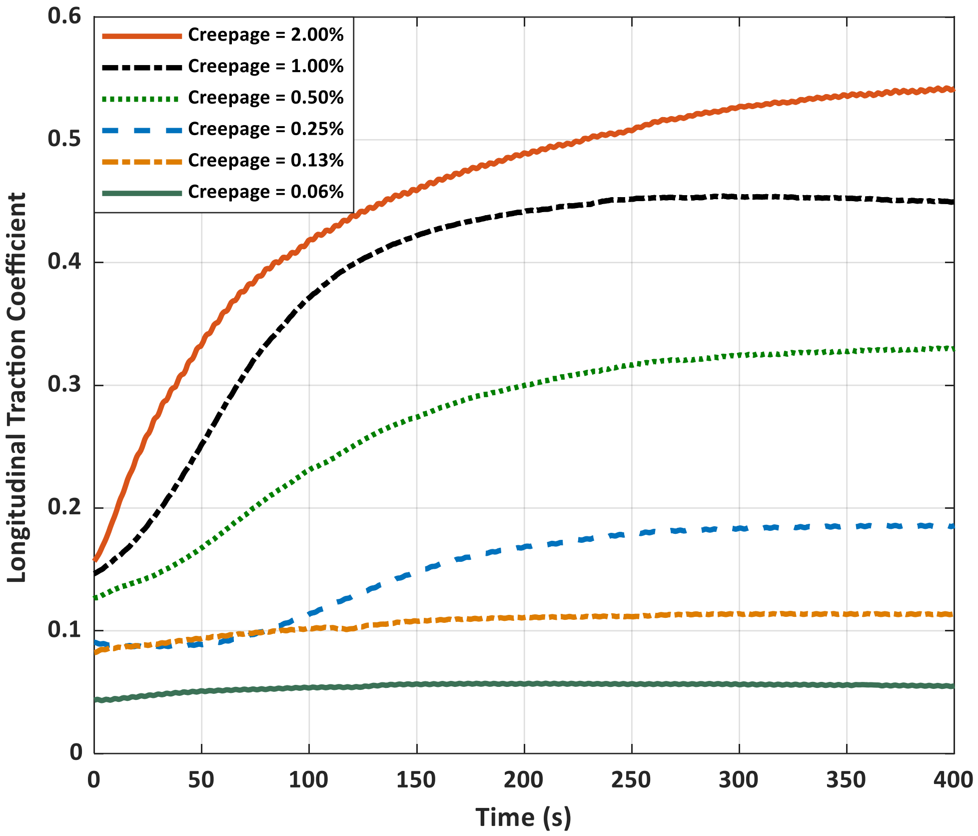

- Similar to wheel load experiments, all the curves indicate an increasing phase in the traction coefficients; however, the increase in traction coefficients for low creepages is considerably small
- For cleaned surfaces at the beginning of the experiments, traction coefficients are significantly smaller than those reached in time with added wear
- The %creepage significantly influences the generation of third body layers at contact. Higher %creepage result in high creep forces and traction coefficient at the contact
- Unlike wheel load experiments, the traction coefficient curves for creepage experiments have started at different values indicating that the traction coefficient varies with %creepage even for cleaned surfaces, at the start of the tests
- There is a direct correlation between %creepages and traction coefficients
- For lower %creepages, lower traction coefficients are observed at given times, mainly due to generation of less worn materials at the contact
- At each creepage, the traction coefficient increases during the transient phase and plateaus to a level that is directly proportional to %creepage
- The relationship between %creepage and traction coefficient is nonlinear, meaning that doubling the %creepage does not yield twice as much traction

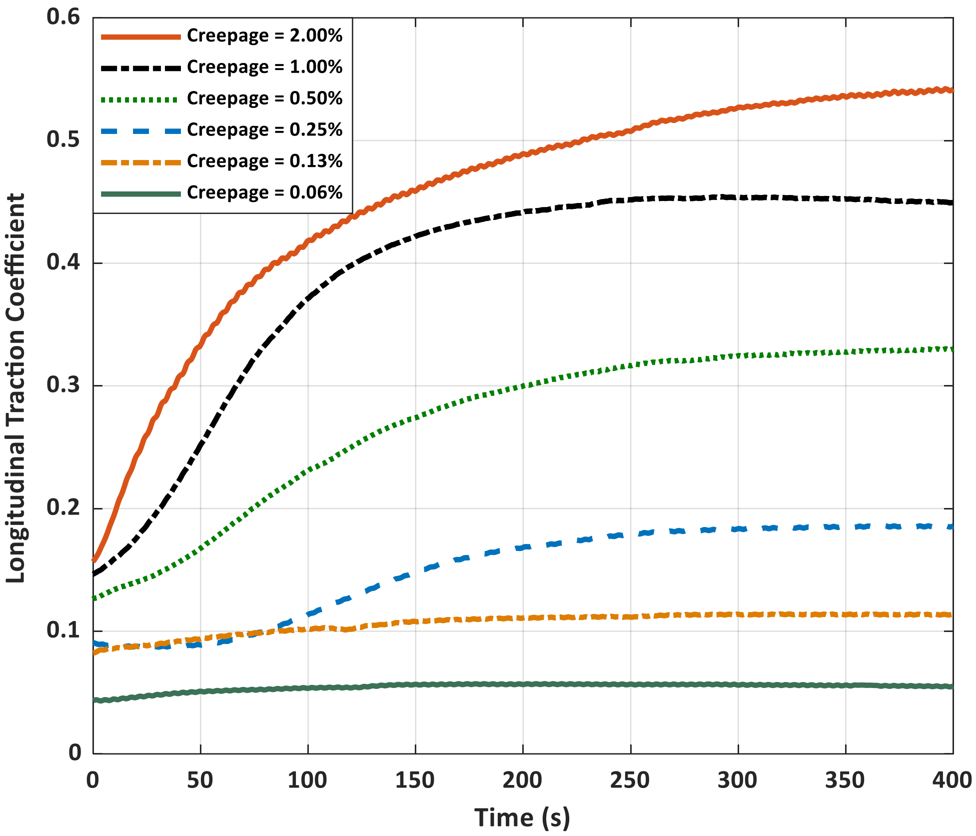

Figure 5.6 Longitudinal Traction Coefficient Behavior for Creepage-based Experiments

To analyze the transient period of traction coefficients, the difference between the maximum and minimum traction coefficients (range of traction) are considered and plotted in Figure 5.7. for smaller %creepages, the difference between the maximum and minimum traction coefficient is significantly smaller than for larger %creepages. The rate of change for the range of

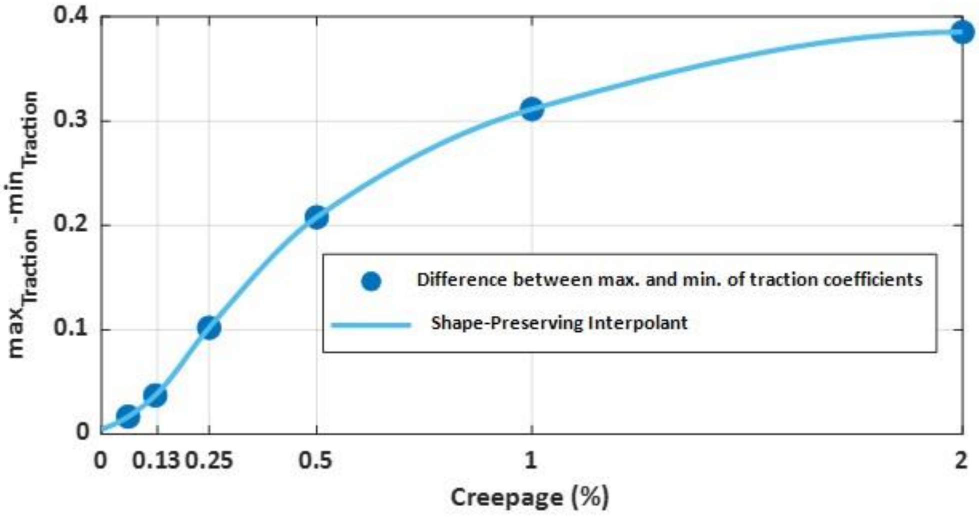

traction is far larger for smaller %creepages than higher creepages. The plot nearly reaches zero slope at 2% creepage. The plot indicates that even with higher %creepages no additional traction is gained due to the saturation of the contact patch.

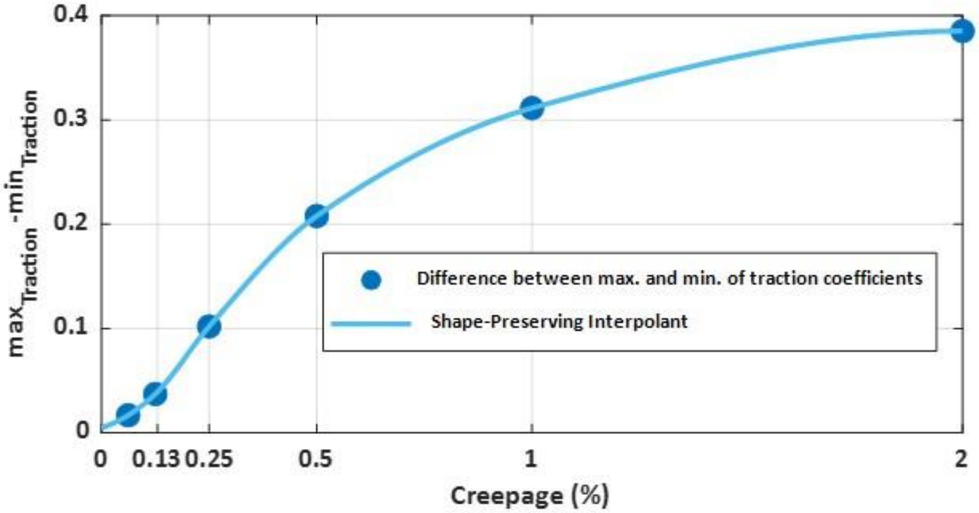

Figure 5.7 Difference Between Maximum and Minimum Traction Coefficient for Creepage-based Experiments

5.4. Case Study 3: Sweeping Creepage

A complete list of variables for this case study is included in Table 5.3. This case is designed to observe the change in longitudinal traction when %creepage sweeps from 0 to 2%. The sweep occurs gradually while a single test is run, in contrast to Case 2 for which %creepage was changed in discrete steps in separate experiments. The creepage is slowly changed according to Figure 5.8, stating at 0 linearly ramping up to 2% and ramping down back to 0, and finally ramping back to the mid-point, at 1% creepage. This amounts to one-and one-quarter cycle of sweep. The full cycle enables determining any hysteresis that may exist. The final quarter of the cycle is intended to ensure that the data is repeatable, and no changes has occurred during the sweep cycle.

Table 5.3 Test Conditions for Sweeping Creepage Study

TEST PARAMETER	VALUE
Wheel Profile	AAR-1B
Roller Profile	US-136 rail
Angle of Attack (°)	0
Cant Angle (°)	0
Field Speed (km/h)	3.0
Rig Wheel Load (kN)	9.2

Full-Scale Wheel Load (kN)	147.2
Commanded Creepage (%)	0 - 2.0
Initial Surface Condition	Accumulated with Third Body Layer

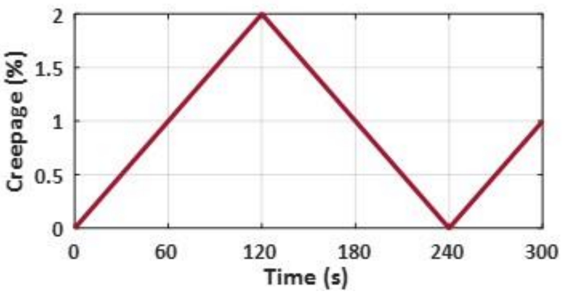

Figure 5.8 Sweeping Creepage Test Cycle

The starting point for the tests is with the running surfaces being at their steady-state condition, meaning that the worn material have reached the amount required that they do not contribute to any changes in traction coefficient. This is in contrast to the earlier cases that studied the change in traction coefficient with increased generation of worn material. For this case, the peak traction values are compare with existing theories and models.

Figure 5.9 shows the calculated longitudinal traction coefficient based on measurements during the creepage cycle. Although, longitudinal traction coefficient values are small at low creepages, the curve is steeper compared to those in high creepages. A small deviation results in larger fluctuations in longitudinal traction coefficient while testing in small creepages. There is a small difference in longitudinal traction coefficient values in each portion of cycle at the same creepages. This may be due to the small changes on the wheel surface condition, surface hardness, surface roughness, third body layers compactness and structure during testing.

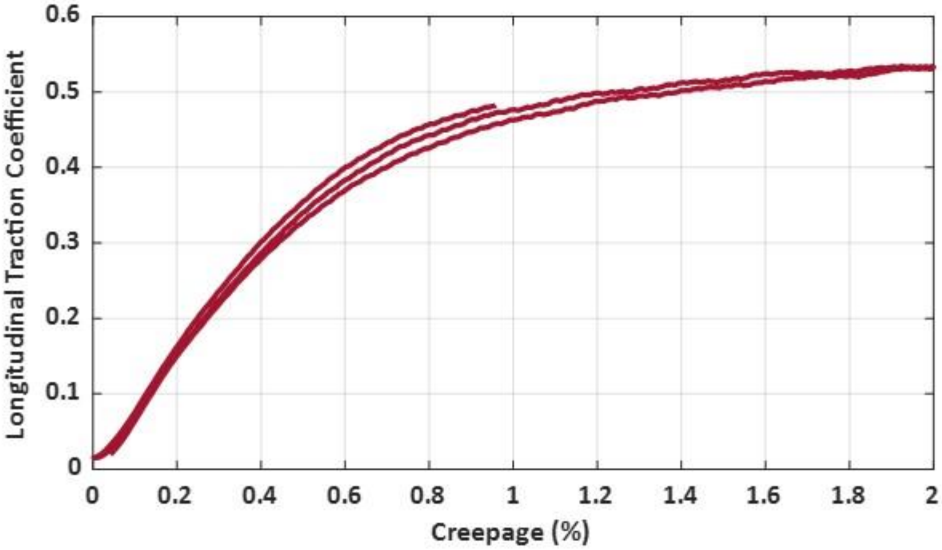

Figure 5.9 Longitudinal Traction Coefficient vs. Creepage Curve

In the last case study, the discrete creepage effect on the transient traction coefficient was investigated. The results of study can be compared with these results for steady state traction coefficient conditions. The final value of longitudinal traction coefficient in the steady-state condition is recorded and compared with the current results. In addition, a simulation is performed with CONTACT software to investigate the differences between the models and measurements on the rig. The test parameters are carefully implemented in CONTACT software and the results are co-plotted in Figure 5.10. The predictions by the model are in good agreement with the measured traction coefficients, particularly for smaller %creepages.

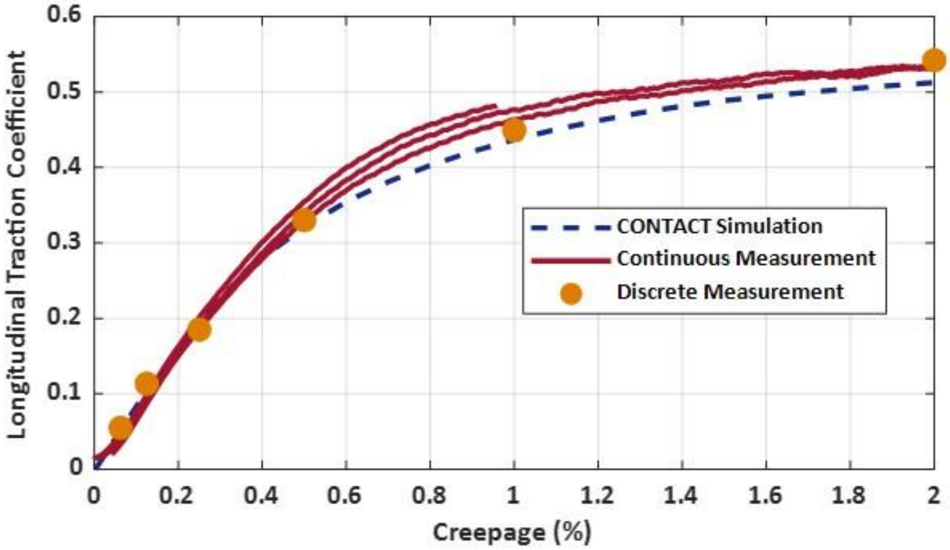

Figure 5.10 Longitudinal Traction Coefficient Comparison for Sweeping, Discrete Measurements and CONTACT software

5.5. Case Study 4: Angle of Attack

The effect of angle of attack (AOA) at the wheel and rail contact on lateral and longitudinal traction coefficient is evaluated, under precisely controlled angles. Both negative and positive AOA, up to two degrees, are studied for a 1:20 tapered wheel, representing the dynamics in a curve [52]. As shown in , during curving the angle of attack on the leading axle, α_L, is negative, and the angle of attack on the trailing axle, α_T, is positive [52]. The roller rig experiments were performed based on the conditions of the right-hand wheel on the leading axle in

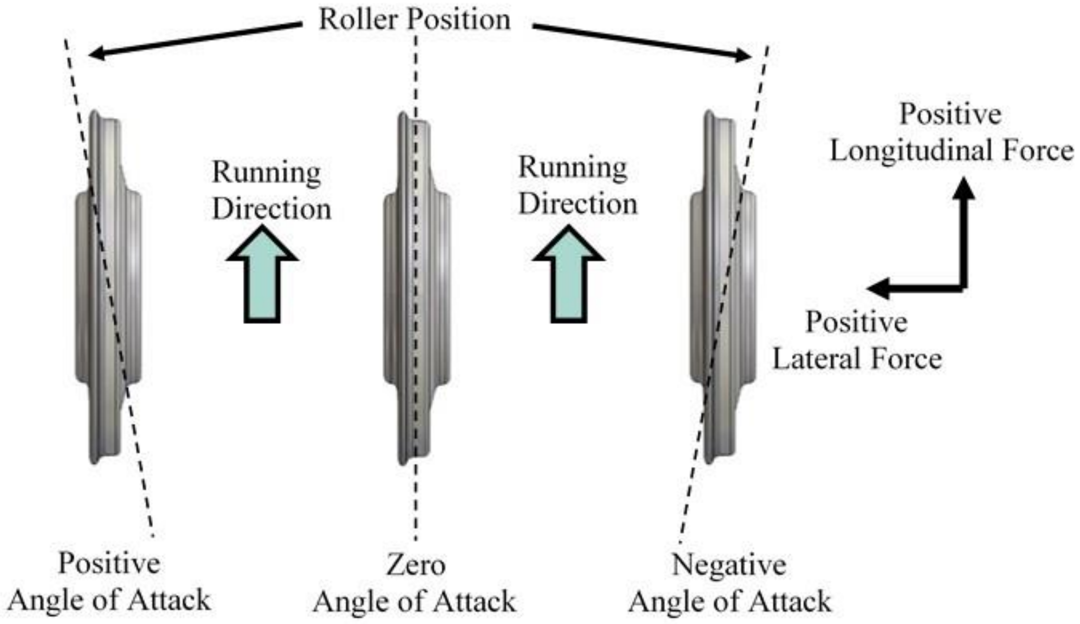

Figure 5.12 Angle of Attack Direction Definition of the VT-FRA Roller Rig

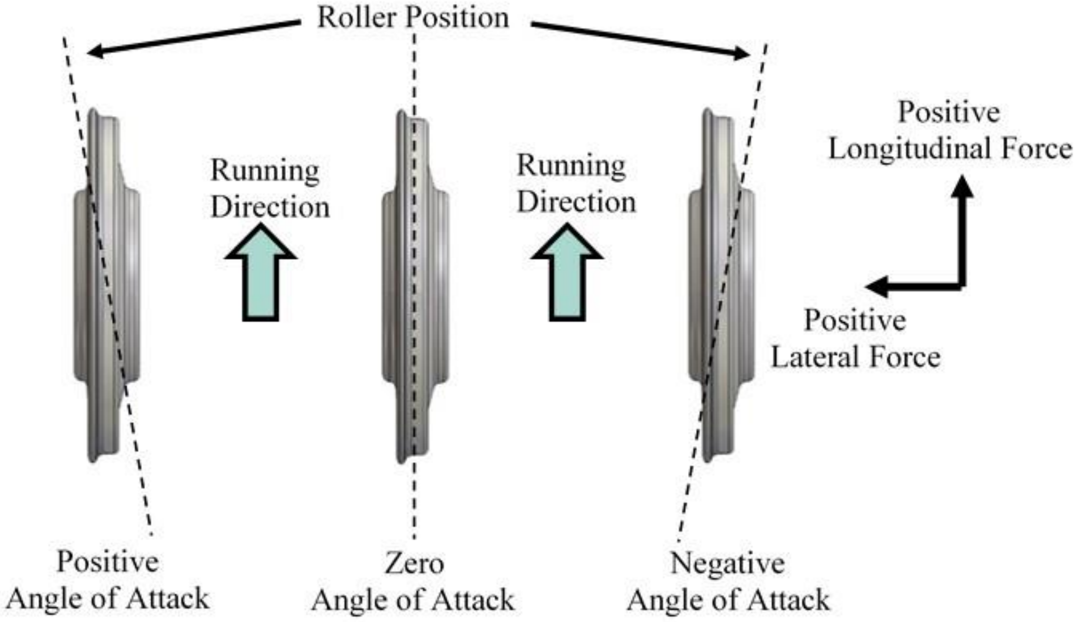

Figure 5.12 Angle of Attack Direction Definition of the VT-FRA Roller Rig

. Therefore, the relationship between the wheel-roller position and angle of attack on the rig is summarized and illustrated in Figure 5.12.

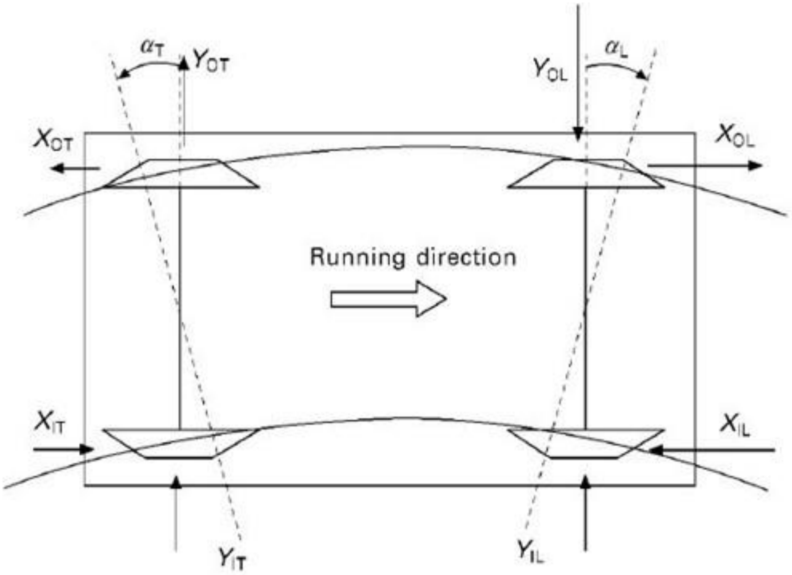

Figure 5.11 Attitude of a Railway Bogie During Curve Negotiation [52]

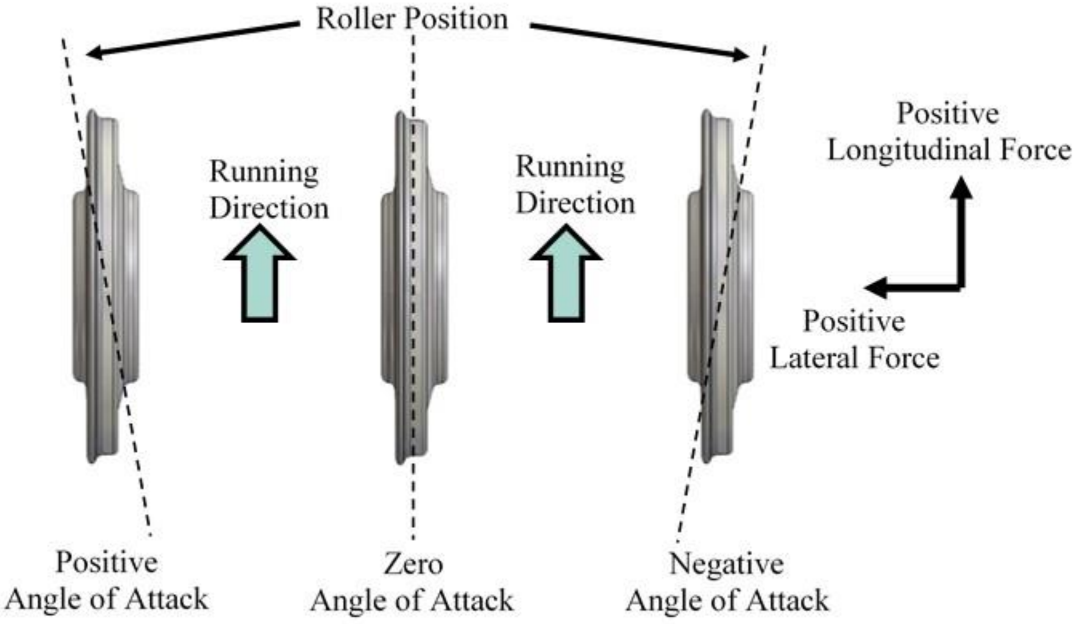

Figure 5.12 Angle of Attack Direction Definition of the VT-FRA Roller Rig

The experiments were performed using a 1/4th-scaled AAR-1B tapered wheel at $0, \pm 0.25°, \pm 0.5°, \pm 1°$, and $\pm 2°$ angle of attack. By using the tapered wheel for the experiments, negative and positive angle of attack causes different results for measured creep forces at contact, which makes it necessary to consider both negative and positive angle of attack. Test conditions under which the experiments were conducted are summarized in Table 5.4.

Table 5.4 Test Conditions for Descrete Angle of Attack Experiments

TEST PARAMETER	**VALUE**
Wheel Profile	AAR-1B
Roller Profile	US-136 rail
Angle of Attack (°)	-2 to +2
Cant Angle (°)	0
Field Speed (km/h)	3.0
Rig Wheel Load (kN)	9.6
Full-Scale Wheel Load (kN)	153.6
Commanded Creepage (%)	2.0
Initial Surface Condition	Clean and Dry

Prior to each series of tests, the wheel surface is examined to assure that it is clean and free of any dust or debris. A photo of the wheel surface condition before the start of each individual series of tests is shown in Figure 5.13.

Figure 5.13 Wheel Surface Condition Before Experimenting

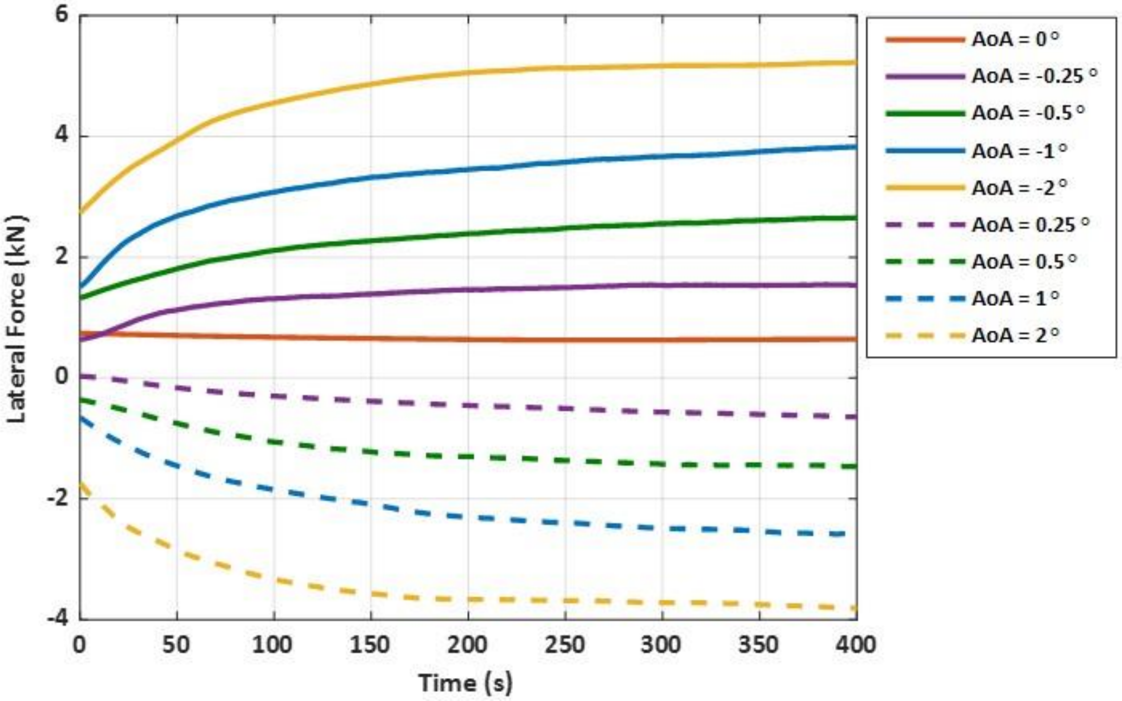

Figure 5.14 shows the lateral forces measured during all angle of attack experiments, ranging from −2° to +2°. The figure clearly shows that positive and negative angle of attack has different effects on the lateral force results. Positive angle of attack result in lateral forces lower than 0° angle of attack curve, and lateral force curves for negative angle of attack are larger than 0° angle of attack lateral force curve. Using a tapered wheel, the lateral force measured for the experiment with 0° angle of attack has a positive offset; however, the generation of natural third body layers has almost no effect on the behavior of the curve.

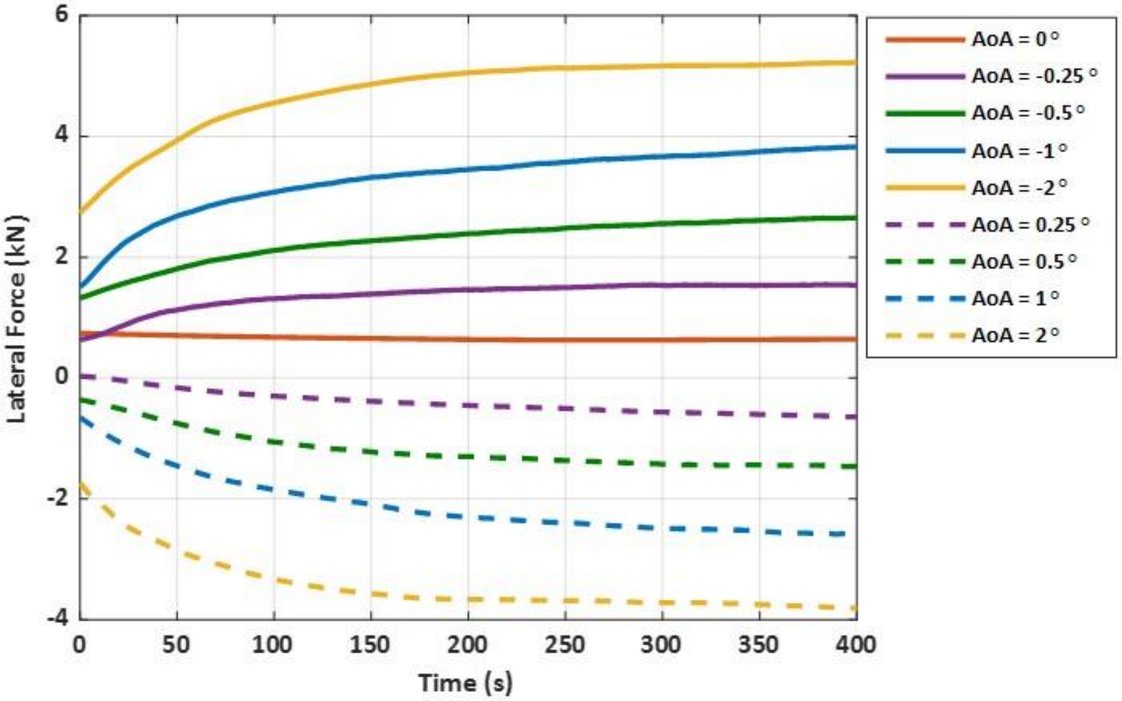

Figure 5.14 Lateral Forces Measured During All Angle of Attack Experiments

At the beginning of each test, the initial value of the lateral force is greatly influenced by the angle of attack, in a direct relationship. Larger AOA results in a larger initial lateral force. This indicates that the surface condition does not influence the initial value of the lateral force, but AOA does significantly.

Based on the lateral force data measured on the rig, it is possible to calculate the lateral traction coefficient. Figure 5.15 provides the lateral traction coefficient curves for the angle of attack experiments. As shown in the figure, angle of attack changes the wheel-rail interface dynamics significantly. The angle of attack parameter results in different lateral traction coefficient curves. By increasing angle of attack, the lateral traction coefficient rises abruptly due to the lateral projection of creep forces at contact. It is noteworthy to point out that there is almost no change where the angle of attack is zero because all the creep forces in the contact patch are increasing in the longitudinal direction.

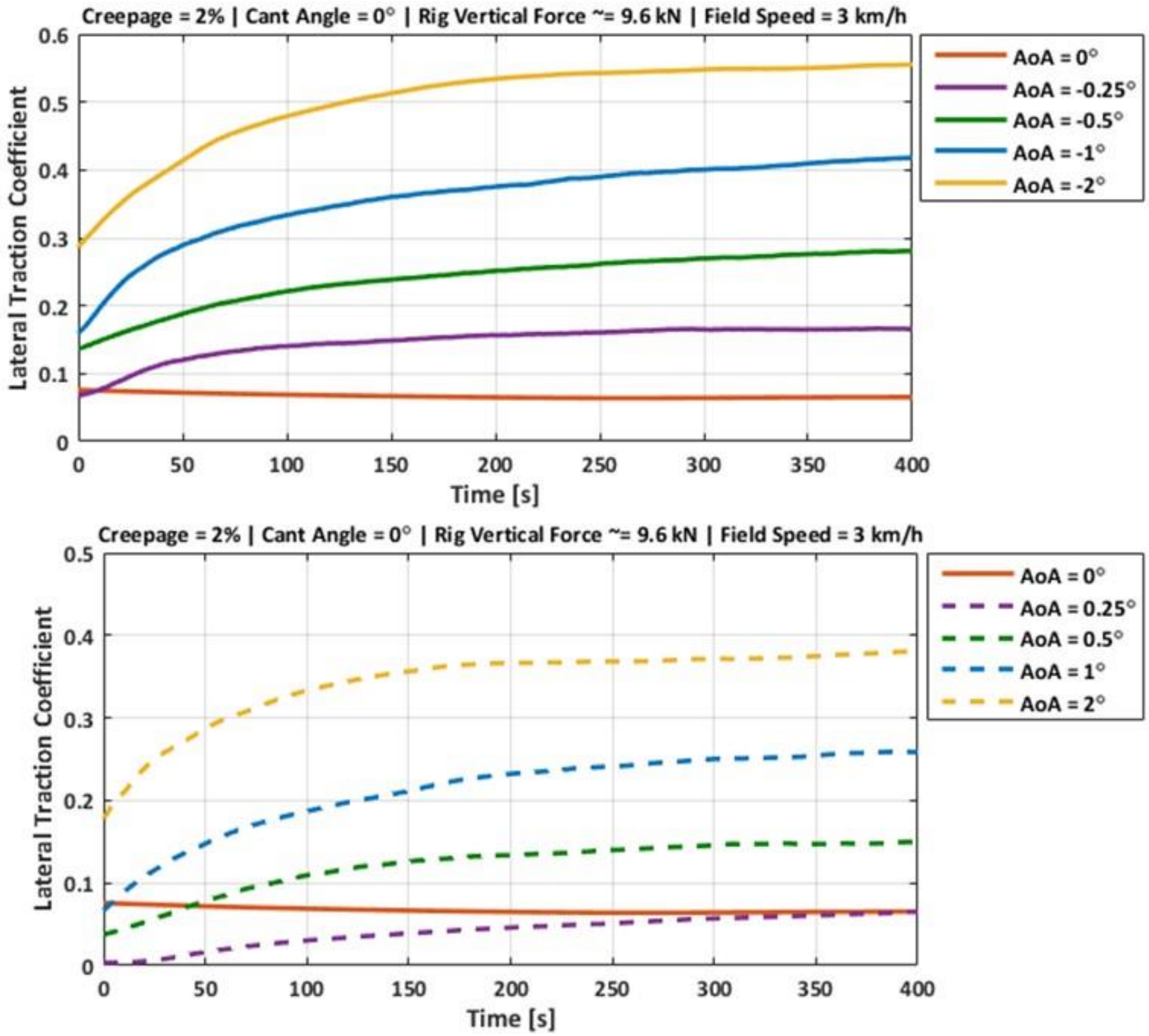

Figure 5.15 Lateral Traction Coefficient Curves for Discrete Angle of Attack Experiments – Negative Angle of attack (Top), Positive Angle of attack (Bottom)

As shown in Figure 5.14, for the angle of attack between +0.25° and +2°, the lateral creep force curve is lower than 0° angle of attack. Therefore, the lateral traction coefficient curves for positive angle of attack intersect the 0° angle of attack curve. Also, for larger angle of attack, the curves have steeper rises as the resulting creep force at contact patch has a bigger projection in the lateral direction.

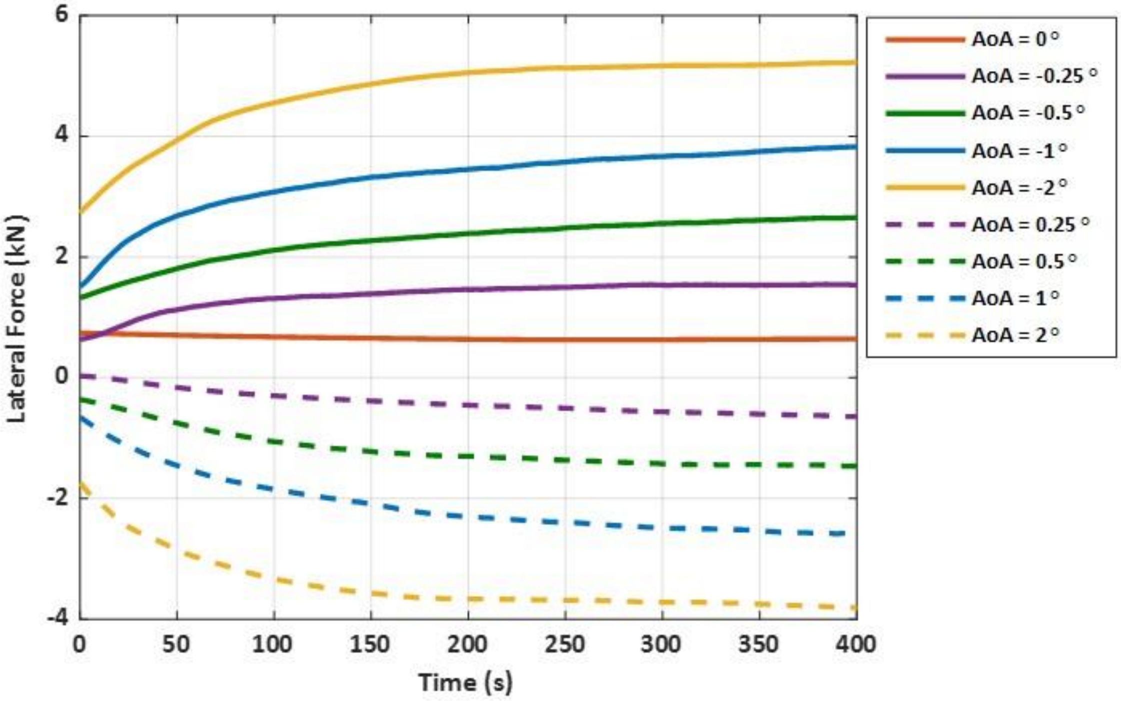

Due to the running direction of the wheel and the roller, it is expected that the longitudinal creep forces are in the positive direction for all angle of attack experiments. Besides, the wheel load in which all the experiments are performed is the same. Therefore, analyzing the longitudinal traction coefficient curves would be the same as interpreting the longitudinal creep force behaviors.

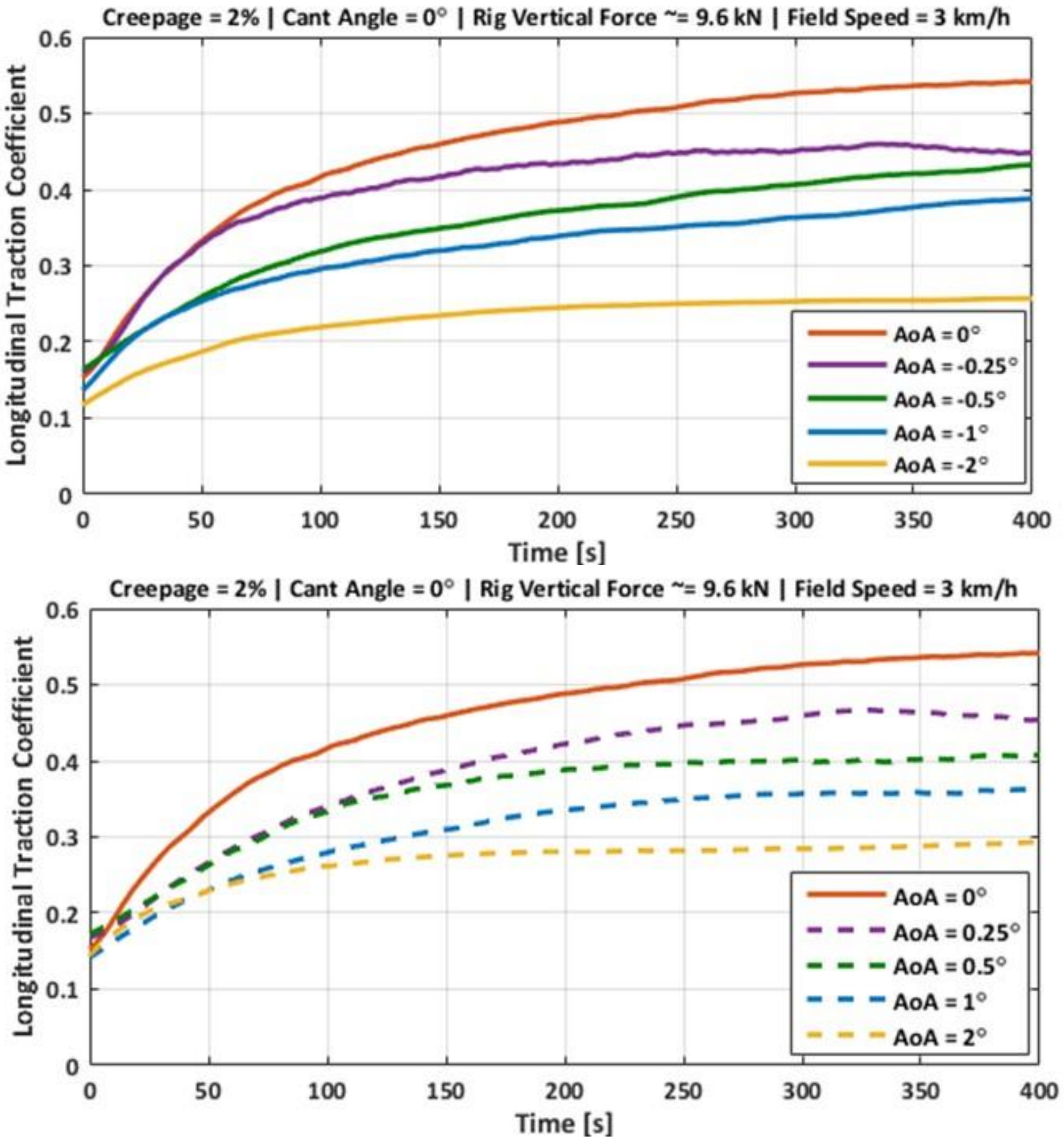

Figure 5.16 Longitudinal Traction Coefficient Curves for Discrete Angle of Attack Experiments – Negative Angle of attack (Top), Positive Angle of attack (Bottom)

Figure 5.16 shows the longitudinal traction coefficient curves for all angle of attack experiments. The results have some similarities and differences with the lateral traction coefficient results. As expected, the longitudinal traction coefficient for large angle of attack plateau at a lower value. The resulting creep force at the contact patch has a greater projection in the lateral direction, which makes the longitudinal creep force smaller.

Figure 5.16 shows that all the longitudinal traction coefficients start at nearly the same traction coefficient, which means that angle of attack has a small effect on the longitudinal traction coefficient when the wheel is still in clean condition. During experimenting, it seems that generation of natural third body layers influences the longitudinal tractions significantly. At the end of the tests (at 400 seconds), each curve reaches a different value resulting in a wider longitudinal traction range.

To better compare the lateral traction coefficient curves, the measurements of positive and negative angle of attack are co-plotted in Figure 5.17. There is an offset between positive and negative angle of attack measurements with the same absolute value. One of the factors causing this difference is the taper of the wheel; however, the offset value is not the same for all experiments. For example, the difference between steady-state lateral traction coefficients for $-2°$ and $+2°$ angle of attack is larger than the difference value for $-0.25°$ and $+0.25°$.

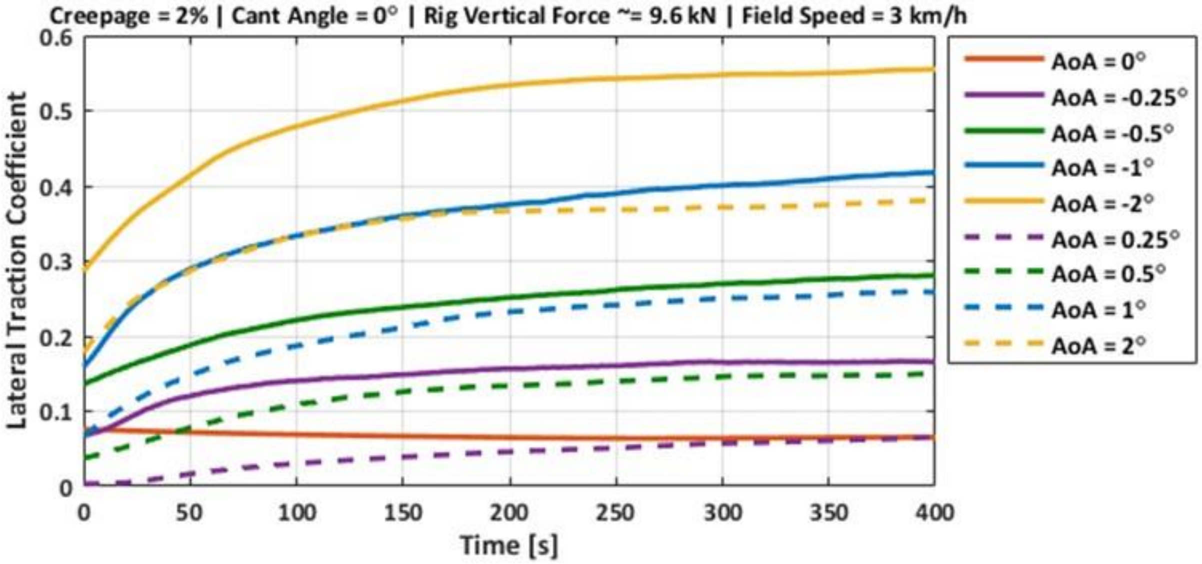

Figure 5.17 Lateral Traction Coefficients Measured During All Angle of Attack Experiments

If the offset value of the 0° angle of attack (due to the wheel taper) is deducted from all the lateral traction coefficients, the lateral traction coefficient curves with the same angle of attack absolute value get closer to each other, shown in

Figure 5.18. Based on the results, it may be concluded that the effective conicity influences the traction coefficient behavior for positive and negative angle of attack remarkably. However, eliminating the influence of effective conicity at zero AoA caused the curves with the same absolute value of angle of attack to get closer to each other, but measurements for larger angle of attack indicate a larger difference between the curves.

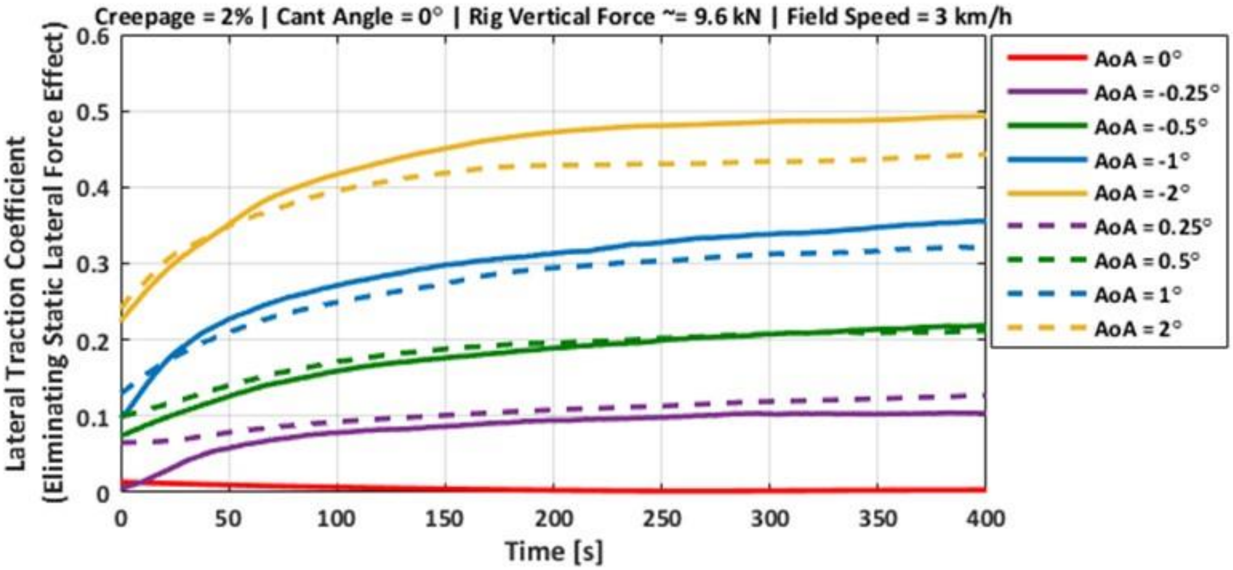

Figure 5.18 Lateral Traction Coefficient Curves for all Angle of Attack Experiments without the Effect of **0**° Angle of Attack Static Lateral Force

Figure 5.19 shows a 3D plot of lateral traction coefficient for all angle of attack experiments. To generate the 3D plot, a linear interpolation between the lateral traction coefficients is used. It seems that negative angle of attack result in more lateral traction coefficients due to the wheel conicity. As expected, lower values of lateral traction coefficient occur at smaller values of angle of attack; however, the minimum value of the lateral traction coefficient is obtained at a value other than 0° angle of attack. Besides, the figure shows that the rate of increasing lateral traction coefficient for negative angle of attack is higher.

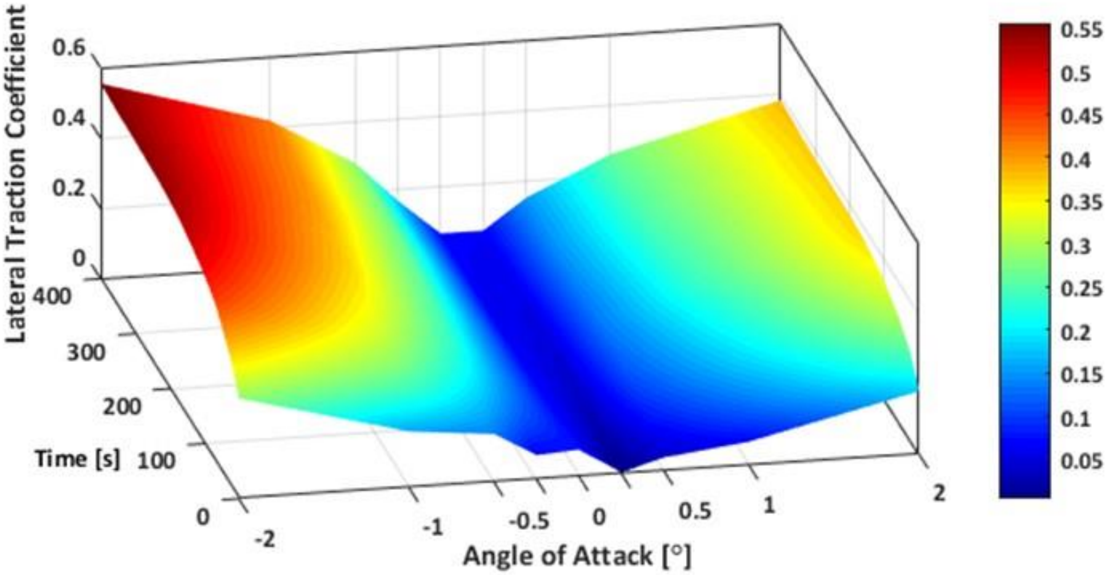

Figure 5.19 Lateral Traction Coefficient for Angle of Attack Experiments - 3D Plot

Figure 5.20 indicates the lateral traction coefficient values for various angle of attack at certain time points (100, 200, 300, and 400 seconds). The lateral traction coefficients for small angle of attack is small at all time points compared to high positive and negative angle of attack. Besides, the 300-second and 400-second curves are close to each other, which means that the rate of changing the lateral traction coefficient is too small after 400 seconds of performing the experiments, and the maximum lateral traction value that can be obtained is close to the lateral traction coefficient value at the 400-second point. The minimum lateral traction coefficient for each curve occurs at a small positive angle of attack due to the taper of the wheel. The difference between lateral traction coefficient between the 100-second curve and 400-second curve for large angle of attack is bigger compared to small angle of attack experiments. It means that the natural third body layer, which generates during the experiments seems to have a stronger effect on the lateral traction coefficient for the large angle of attack.

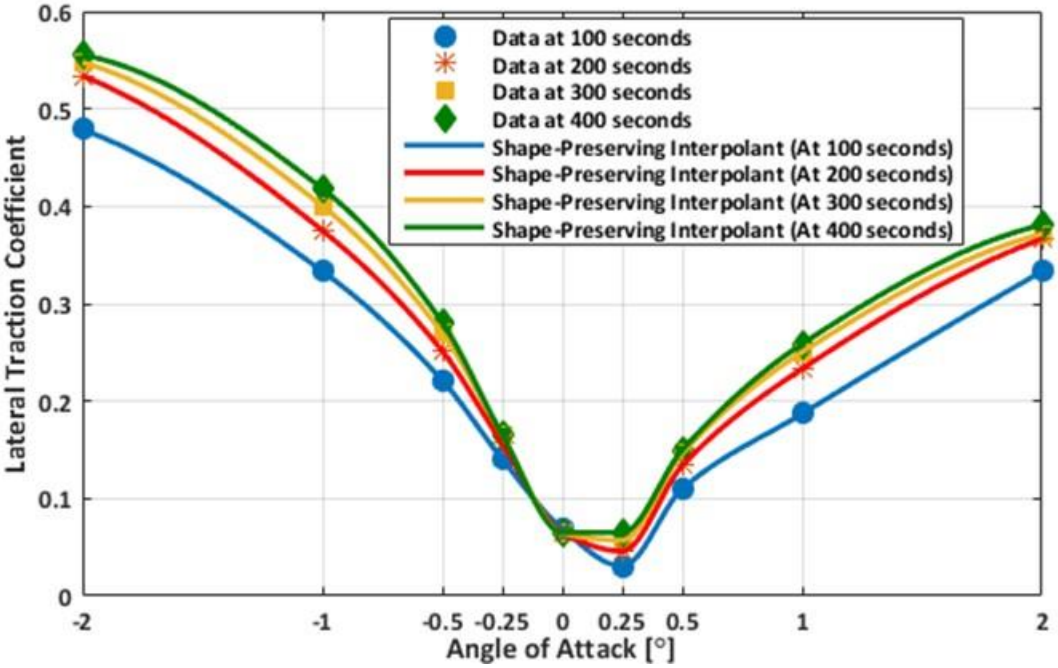

Figure 5.20 Lateral Traction Coefficient Values at Several Time Points

Similar to the 3D plot illustrated for lateral traction coefficient, another 3D plot can be constructed for longitudinal traction coefficient. Figure 5.21 shows that longitudinal traction coefficient is almost similar for all the angle of attack experiments at the beginning of the experiment. During the experiments, it seems that the generation of natural third body layers increases the longitudinal traction coefficient, however, smaller angle of attack results in steeper rise due to the larger projection of creep forces in longitudinal direction at the contact patch.

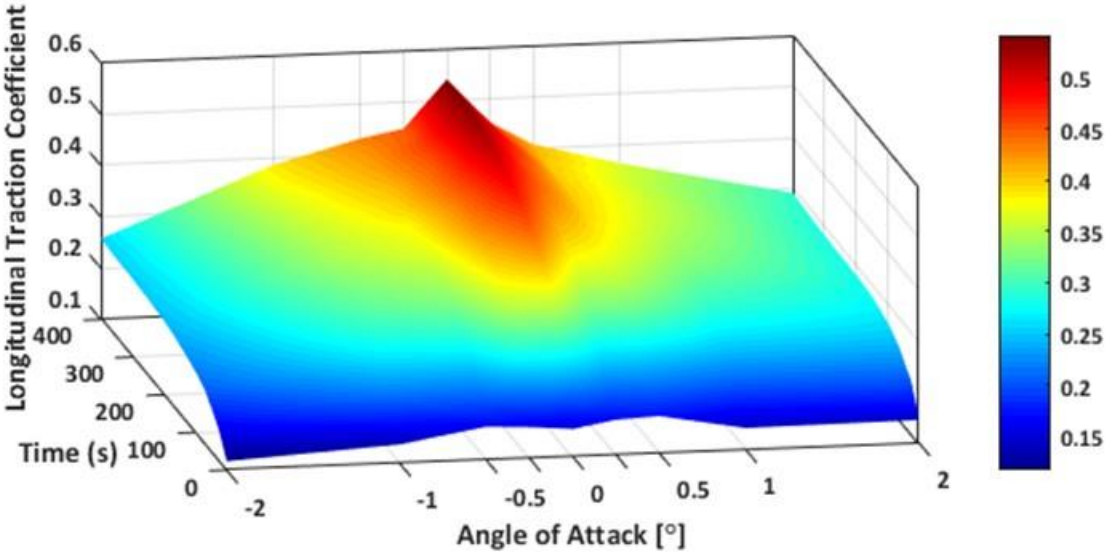

Figure 5.21 Longitudinal Traction Coefficient for Angle of Attack Experiments - 3D Plot

Figure 5.22 indicates the longitudinal traction coefficient values for various angle of attack after performing the experiments for 100 seconds, 200 seconds, 300 seconds, and 400 seconds. The longitudinal traction coefficient is relatively large for small angle of attack, which means that the resulting creep force has a smaller projection in the lateral direction. Comparing the results of 300-second and 400-second experiments shows that the rate of changing the longitudinal traction coefficient becomes smaller as the experiment continues.

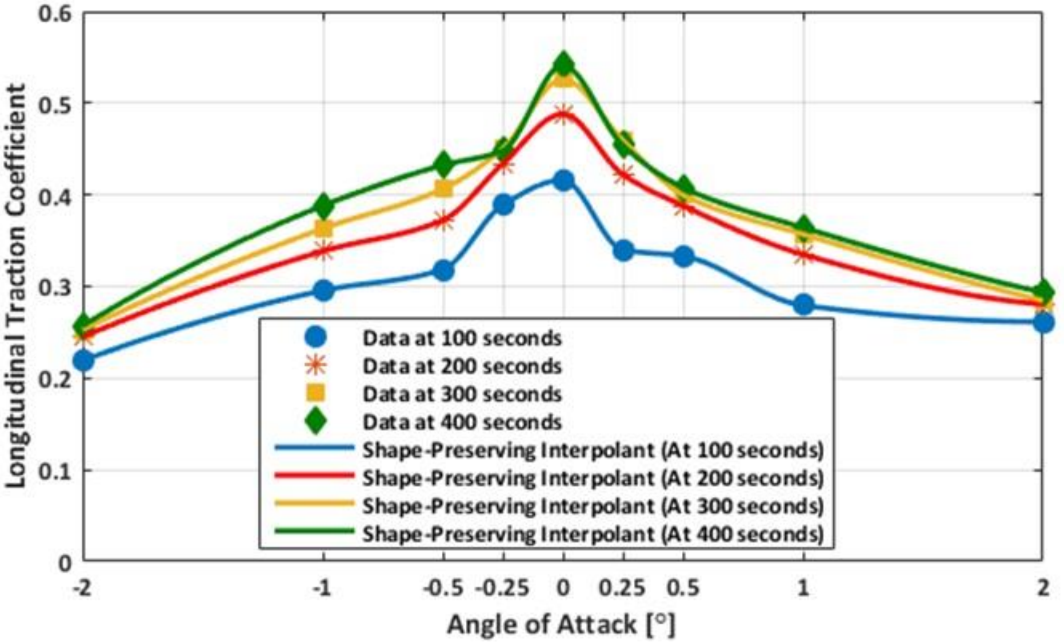

Figure 5.22 Longitudinal Traction Coefficient Values at Several Time Points

5.6. Case Study 5: Sweeping Angle of Attack

In this section, instead of changing the angle of attack in discrete steps and maintain them constant throughout the 300 seconds of the experiment, they are slowly changed starting from -2 to 2 degrees with a constant sweep rate. Three experiments, presented in Figure 5.23, were performed to evaluate the effect of wheel load, wheel type, and angle of attack on the lateral traction coefficients. The first experiment was performed on the tapered wheel with a wheel load of 9.6 kN. The wheel load was decreased to 2.4 kN for the second experiment. The third experiment was conducted on a cylindrical wheel at 2.4 kN wheel load. Comparing the results provides a good estimation of the influence of the angle of attack on the tapered and cylindrical wheel under a range of small to large angle of attack.

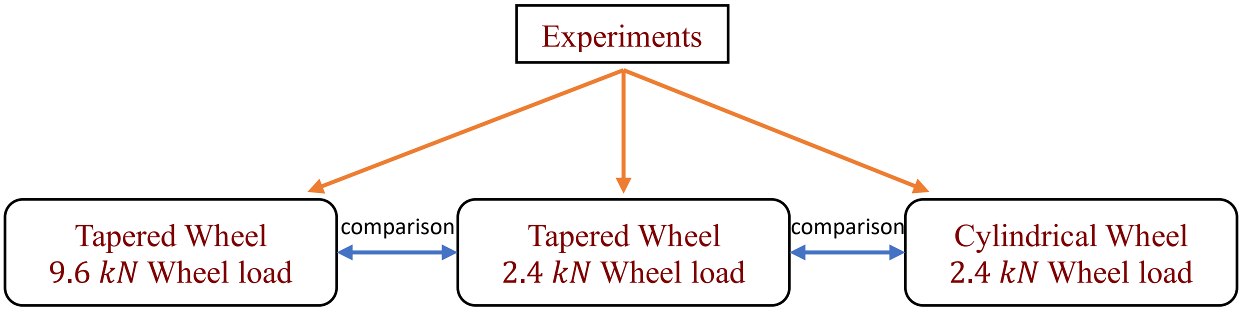

Figure 5.23 Swept Angle of Attack Experiments

For these experiments, the wheel was positioned the same as the left wheel of the leading axle presented in . Therefore, the lateral force at 0° angle of attack is negative, unlike the experiments performed in the previous section for discrete angle of attack.

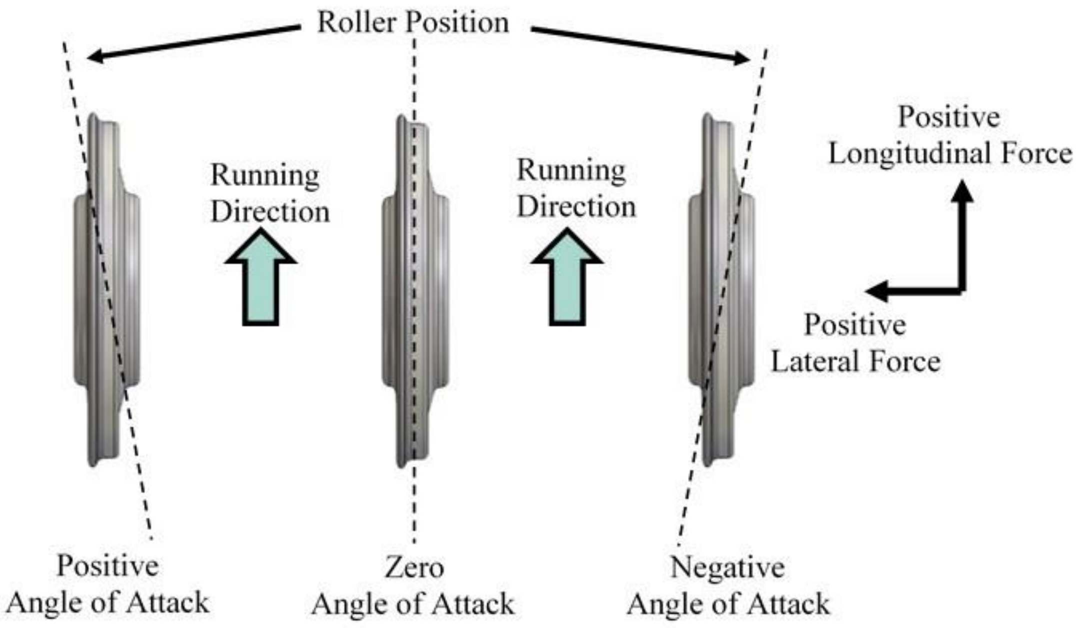

Figure 5.12 Angle of Attack Direction Definition of the VT-FRA Roller Rig

During experiments, the angle of attack was changed continuously at a slow sweep rate in the range of $-1°$ to $1°$. Before experimenting, the roller rig was run for a couple of minutes to assure that the wheel and roller surfaces are covered by third body layers. Therefore, the initial surface condition for these three experiments was considered to be accumulated with third body layers, i.e., the effect of generation of third body layers on the traction coefficient data as a remarkable factor was minimized. Hence, it is possible to analyze the effect of angle of attack on the traction coefficient data more precisely.

The angle of attack was changed based on two cycles. One of the cycles has a quarter portion more than the other one, which makes it possible to analyze any hysteresis that may exist as well as the repeatability of the data. Also, testing in two cycles, starting at different angle of attack provides information about the dependency of test outputs on running cycles. Figure 5.24 shows the test cycles considered for the experiments.

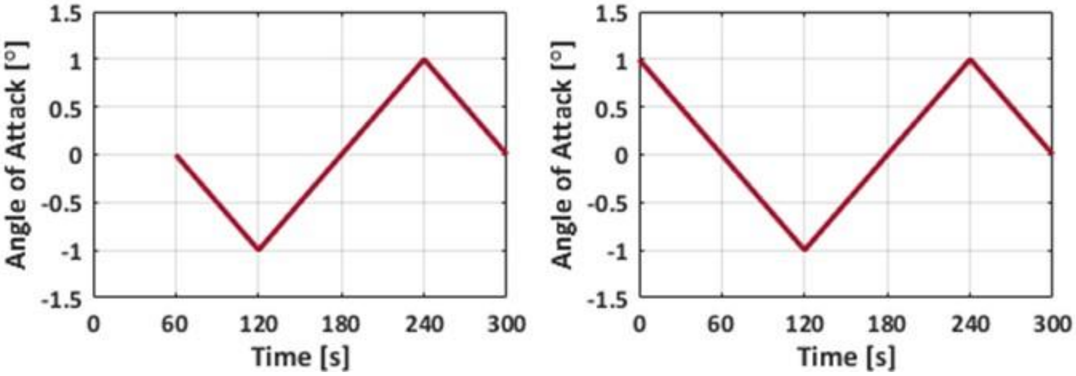

Figure 5.24 Tapered Wheel ($\mathbf{9.6}\ \boldsymbol{kN}$) Test Cycle (Left), Tapered and Cylindrical Wheels ($\mathbf{2.4}\ \boldsymbol{kN}$) Test Cycle (Right)

The other test conditions were the same for all experiments. They were performed under $0°$ cant angle, 3 km/h field speed, and 2.00% creepage. A summary of the test condition is provided in Table 5.5.

Table 5.5 Test Conditions for Swept Angle of Attack Experiments

TEST PARAMETER	VALUE
Wheel Profile	AAR-1B (Tapered) - Cylindrical
Roller Profile	US-136 rail
Angle of Attack (°)	-1 to +1
Cant Angle (°)	0
Field Speed (km/h)	3.0
Rig Wheel Load (kN)	2.4 - 9.6

Full-Scale Wheel Load (kN)	38.4 - 153.6
Commanded Creepage (%)	2.0
Initial Surface Condition	Accumulated with Third Body Layer

All the lateral force curves for the experiments are shown in Figure 5.25. The following observations are made:

- $2.4\ kN$ wheel load experiments have a quarter cycle of 60 seconds at the beginning of the experiments.
- For the cylindrical wheel, the lateral force is almost zero at $0°$ angle of attack; however, for the tapered wheels, DC offsets appears due to the influence of effective conicity. The red dots show the DC offset of the lateral force curves. For $2.4\ kN$ and $9.6\ kN$ wheel load experiments with the tapered wheel, the DC offsets are approximately $200\ N$ and $800\ N$, respectively. The lateral force over wheel load ratio at $0°$ angle of attack represents the taper of the wheel, which is $\frac{1}{12}$ in this case.
- For the cylindrical wheel, the absolute maximum lateral force is almost the same for the negative and positive angle of attack; however, the tapered wheel results are shifted by a DC offset.
- The green points demonstrate the intersection of the tapered wheel lateral forces, which represents the effect of taper. The intersection point is at zero lateral force, and the angle of attack offset from zero ($-0.18°$ and $-0.15°$) is the point in which the lateral force generated by the angle of attack opposes the lateral force due to the taper of the wheel. The difference between $-0.18°$ and $-0.15°$ shows the wheel wear and effective conicity influence on the lateral force data. A small change in the wheel surface condition due to the wheel wear may have changed the effective conicity of the wheel slightly, i.e., the lateral forces are affected. Besides, the wheel wear and change in effective conicity have shifted the intersection point between zero lateral force line and cylindrical wheel lateral force measurement at 180 seconds.
- The change rate of the lateral force during the experiments strongly depends on the wheel load. Therefore, the rates of lateral force changes for $2.4\ kN$ wheel load experiments conducted on both cylindrical and tapered wheels are the same; however, for $9.6\ kN$ wheel load, the change rate of lateral force is more significant.
-

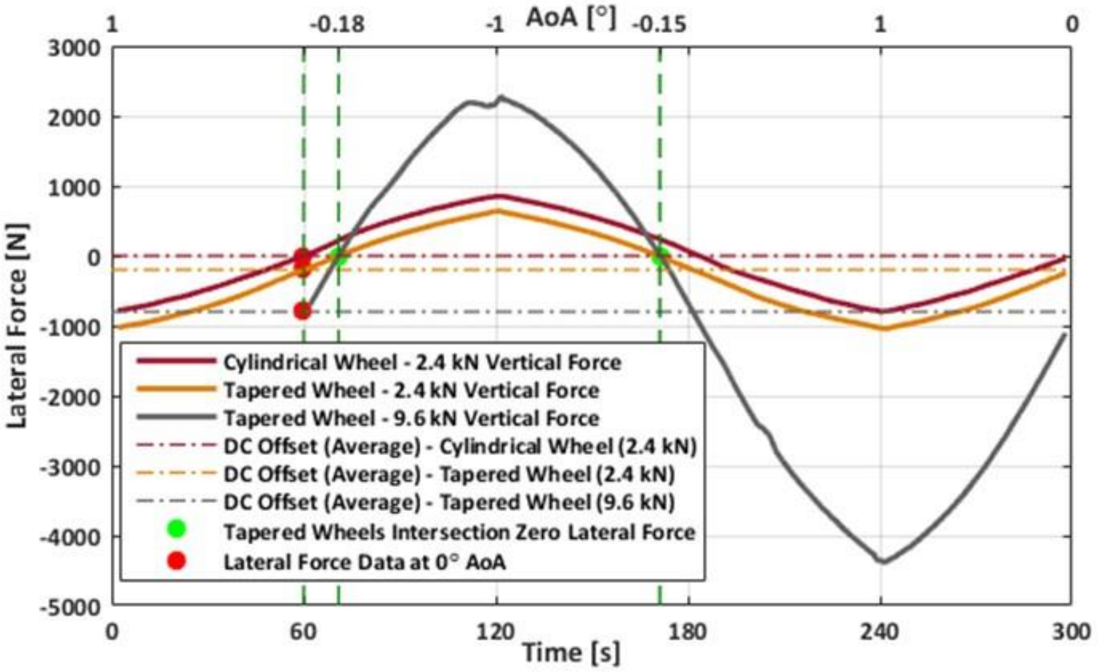

Figure 5.25 Lateral Forces Measured During the Experiments

Based on the lateral force measurements, the lateral traction coefficients can be calculated and analyzed. Figure 5.26 shows the lateral traction coefficient curves for the experiments. For the tapered wheel experiments, the lateral traction coefficient curves are almost on top of each other, which means that the lateral traction coefficient is independent of the applied wheel load at contact. At $-1°$ angle of attack, where the taper of the wheel opposes the effective conicity, the lateral traction coefficient is smaller than the maximum lateral traction coefficient at $+1°$ angle of attack. For the cylindrical wheel, the lateral traction coefficient is almost the same at $-1°$ and $+1°$ angle of attack; however, the maximum lateral traction coefficient is smaller than the tapered wheel.

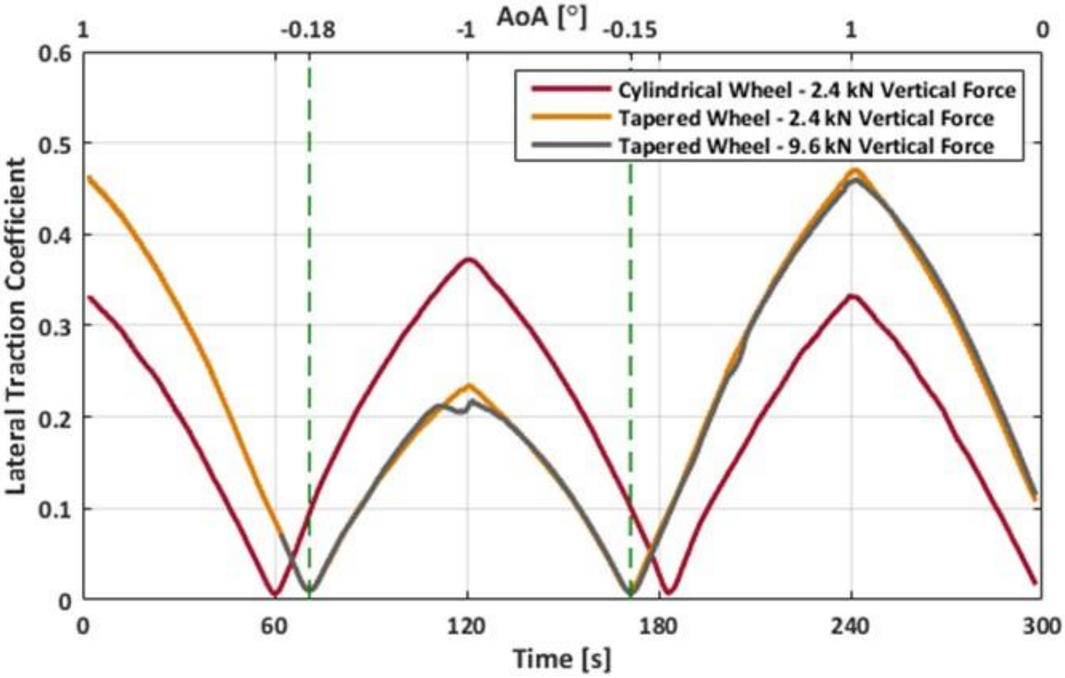

Figure 5.26 Lateral Traction Coefficient Calculated for Swept Angle of Attack Experiments

Figure 5.27 presents the lateral traction coefficient curve versus angle of attack. Comparing the results for tapered wheel experiments shows that the quarter cycles added to $2.4\ kN$ experiment has not influenced the behavior of lateral traction curve, and the results are almost the same. The figure clearly shows the offset in the minimum lateral traction coefficient for the tapered wheel. It also shows that the minimum is the same for both tapered wheel tests, indicating that it is independent of wheel load. The increase in the rate of lateral traction coefficient for positive angle of attack is more significant than negative AOA, which makes the maximum lateral traction coefficient for tapered wheel experiments extensive.

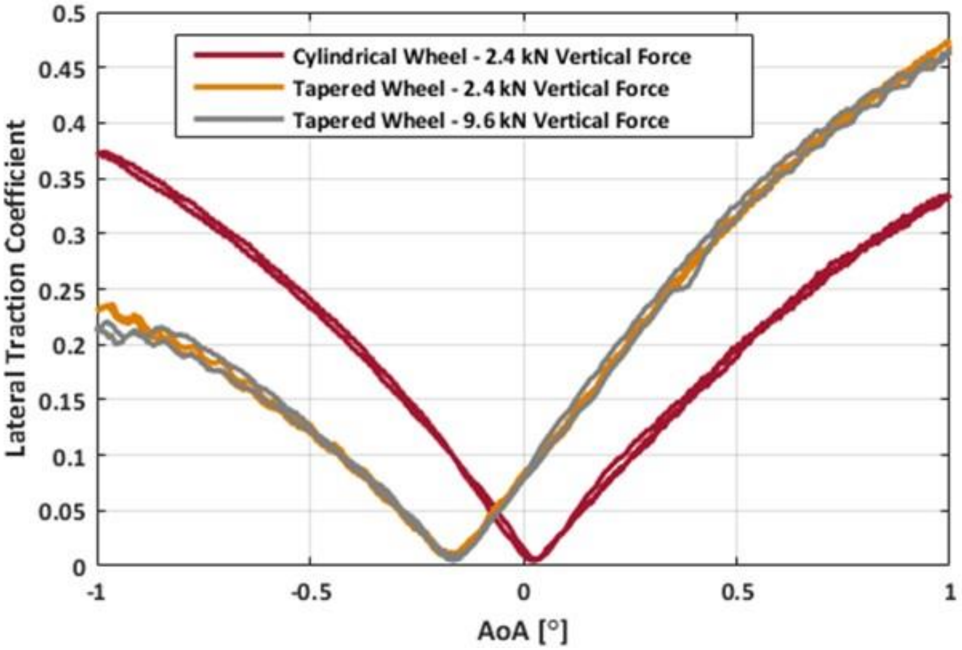

Figure 5.27 Lateral Traction Coefficient vs. Angle of Attack for Swept Experiments

5.7. Case Study 6: Sweeping Angle of Attack under Several Creepages

In this section, the results of several experiments on changing angle of attack continuously at various creepages are provided. Creepages as small as 0.25% and as large as 2.00% are considered for this study. At each creepage the angle of attack is continuously increased and decreased based on a cycle with minimum of $-1°$ and maximum of $1°$. Before performing experiments, the wheel surface was redressed properly to eliminate the wear band formed previously. For this study, both longitudinal and lateral traction coefficients are considered and evaluated since angle of attack and creepage contribution results in significant effect in both longitudinal and lateral directions. In addition, the total traction coefficients of tests are calculated and compared.

The cylindrical wheel is used for this study. The angle of attack was changed continuously at a slow sweep rate in the range of $-1°$ to $1°$ while experimenting. Before testing, the roller rig was run for a couple of minutes to assure that the wheel and roller surfaces are covered by third body layers. Therefore, the initial surface condition for these experiments was considered to be accumulated with third body layers to eliminate the effect of generation of third body layers on the traction coefficient. Hence, it is possible to analyze the effect of angle of attack and creepage on the traction coefficient data more accurately in a fully saturated condition.

The angle of attack was changed based on the cycle shown in Figure 5.28. The cycle has a quarter portion more than the other one, which makes it possible to analyze any hysteresis that may exist.

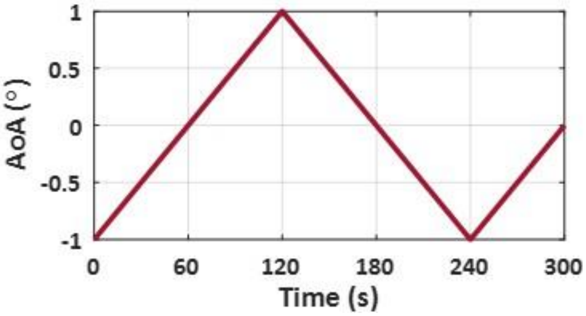

Figure 5.28 Angle of Attack-Creepage Experiment Cycle

Four tests are conducted at low and high creepages, 0.25%, 0.50%, 1.00%, and 2.00%. The other test conditions were the same for all experiments. They were performed under $0°$ cant angle, and $3\ km/h$ field speed. A summary of the test condition is provided in Table 5.6.

Table 5.6 Test Conditions for Angle of Attack-Creepage Experiments

TEST PARAMETER	VALUE
Wheel Profile	Cylindrical
Roller Profile	US-136 rail
Angle of Attack (°)	-1 to +1
Cant Angle (°)	0
Field Speed (km/h)	3.0
Rig Wheel Load (kN)	2.4
Full-Scale Wheel Load (kN)	38.4
Commanded Creepage (%)	0.25 to 2.00
Initial Surface Condition	Accumulated with Third Body Layer

To prepare the wheel surface for the test, first, the wheel surface was redressed using sandpaper to remove any groove formed on it. Then, the wheel and roller were rotated on each other to ensure enough third body layer is accumulated on the wheel surface. Figure 5.29 demonstrates the redressed wheel surface image, profile, and corresponding surface roughness calculations as well as an image of the wheel surface before performing the main experiment (right).

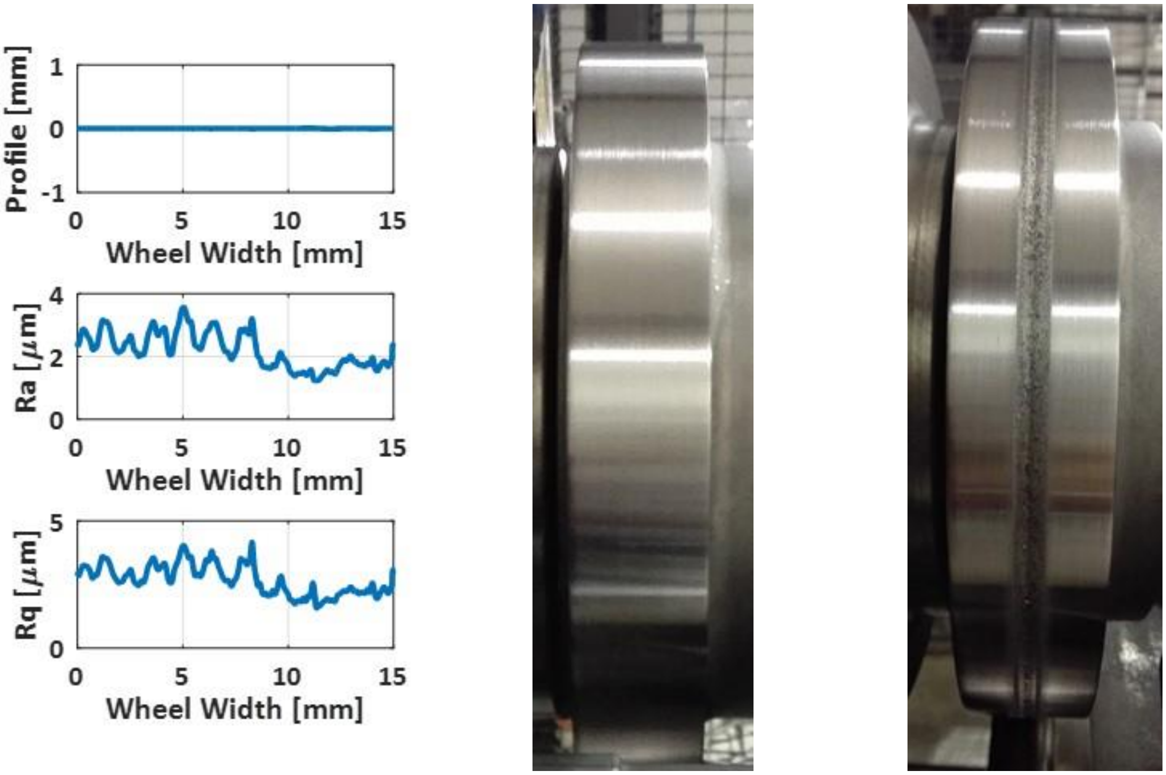

Figure 5.29 Redressed Wheel Surface Profile, and Surface Roughness, Ra, and Rq (left), Redressed Wheel Image (middle), Initial Wheel Surface Condition Before Test (right)

Since both creepage and angle of attack are factors influencing the creep forces, both longitudinal and lateral forces are important to study. All the longitudinal and lateral force curves for the experiments are shown in Figure 5.30. From the figure, it can be illustrated and interpreted that:

- The experiments with lower creepage show more nonlinearity in measure forces since the rate of change in longitudinal and lateral forces are higher at small creepages.
- Since the cylindrical wheel is used, the lateral force is almost zero at 0° angle of attack. The rate of change in lateral and longitudinal forces is almost the same while increasing and decreasing angle of attack for each test.
- At 0° AoA, longitudinal and lateral forces curves are steeper for small creepages.
- More creepage resulted in more longitudinal force, as expected overall the test duration.

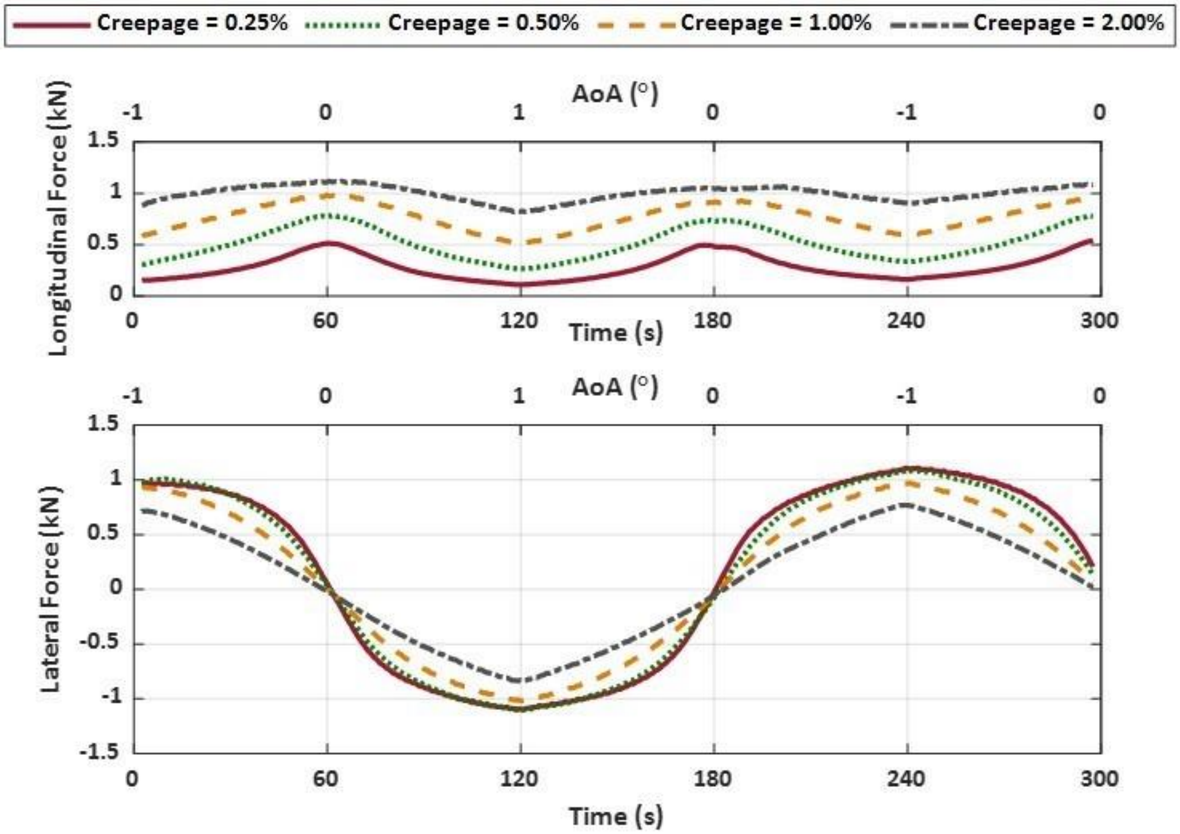

Figure 5.30 Longitudinal and Lateral Forces Measured During the Experiments

Figure 5.31 shows the creep force plots based on angle of attack. The longitudinal force curves are almost symmetric with respect to 0° AoA, and the lateral force curves are approximately symmetric with respect to zero force and 0° AoA point. In addition, the figure clearly shows that the rate of longitudinal and lateral force changes is lower at high creepages.

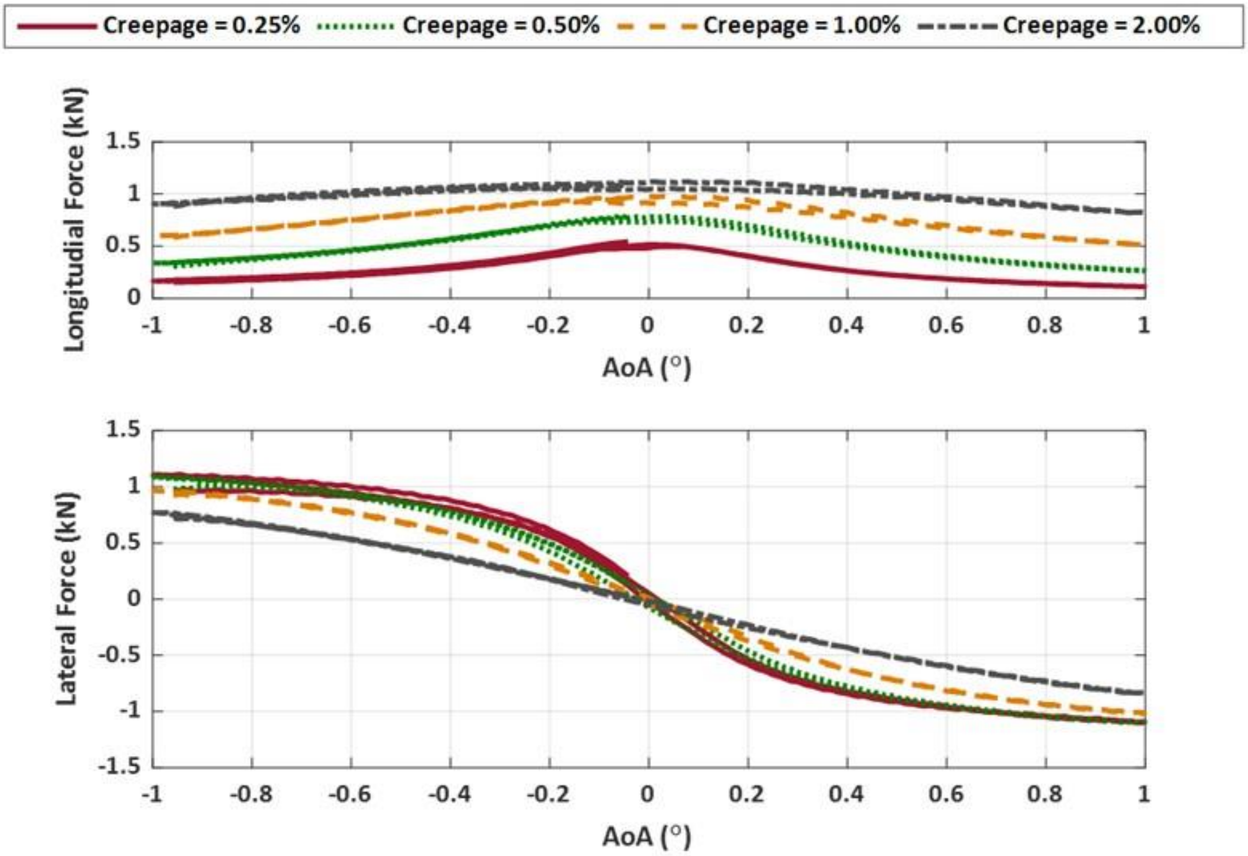

Figure 5.31 Longitudinal and Lateral Forces based on Angle of Attack

Based on the creep force measurements, the longitudinal and lateral traction coefficients can be calculated and analyzed. Figure 5.32 shows the longitudinal and lateral traction coefficient curves for the experiments. Maximum longitudinal traction coefficient and minimum lateral traction coefficients are approximately at 0° AoA since the cylindrical wheel is used. The traction coefficient plots are almost symmetric with respect to zero with a small skew toward the positive angle of attack, which may be as a result of a small taper on the wheel surface. The 1° angle of attack is enough to increase the lateral traction coefficient to a maximum of 0.46 at small creepages.

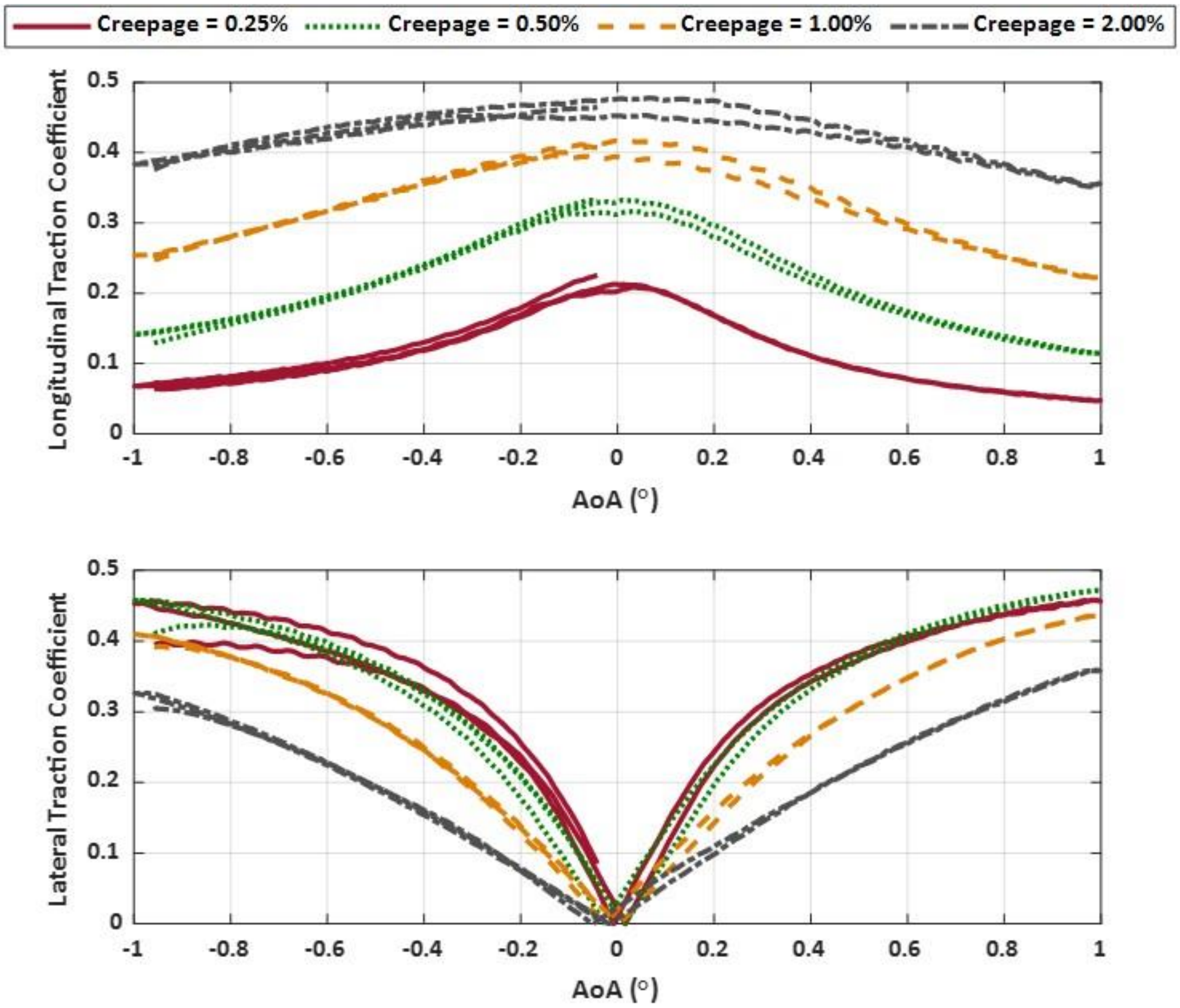

Figure 5.32 Longitudinal and Lateral Traction Coefficients

Figure 5.33 presents the total traction coefficient calculated based on the projected longitudinal and lateral traction coefficients. The figures are provided based on time and angle of attack. At small creepages, the difference between maximum and minimum traction coefficient is significant due to the small longitudinal traction coefficient at 0° AoA. The traction coefficient at 2.00% creepage does not change significantly. This is because of high longitudinal traction coefficient and small rate of change while sweeping AoA. In addition, the maximum traction coefficient is obtained at high angle of attack, where both longitudinal and lateral traction coefficients are contributing.

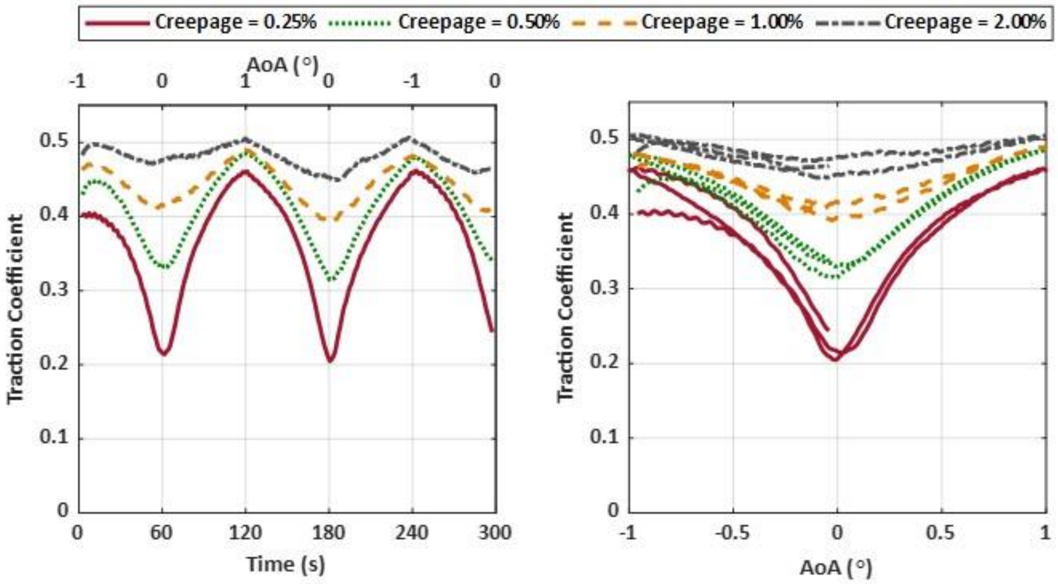

Figure 5.33 Lateral Traction Coefficient vs. Angle of Attack for Swept Experiments

5.8. Summary

In this chapter, the effects of various parameters on creep forces and traction coefficients are investigated. Several experiments were performed under various load and creepage conditions to analyze the effect of wheel load and creepage on the generation of the third body layers and creep forces at contact. The results show that the transient traction coefficient has a steeper rise for larger wheel loads. The larger the wheel load, the higher the rate of generating third body layers at contact, i.e., more longitudinal traction coefficient. The peak for traction coefficient is directly proportional to %creepage. A higher %creepage results in larger creep forces. For small creepages, there is a slight rise in traction coefficient, indicating that the existence of natural third body layers does not have a significant influence.

The angle of attack experiments are performed in two categories, discrete and sweep. Before conducting the discrete angle of attack experiments, the angle of attack is set to the desired value, and the tests are done under clean wheel condition. For the sweeps, the angle of attack is changed continuously during the 300 seconds of the test. The lateral force data is recorded for both a tapered and cylindrical wheel with 2.4 kN and 9.6 kN wheel loads. Results indicate that the wheel load does not influence the lateral traction coefficient data for the same wheel type; however, the lateral traction coefficients strongly depend on the type of the wheel, cylindrical or tapered.

6. Estimating the Wheel Wear and Third Body Layer Accumulation

6.1. Introduction

VT-FRA roller rig is a precise piece of equipment in measuring contact forces. Besides the capabilities of the rig mentioned before in chapter 3, a new feature is currently added to the rig to measure the wheel surface topography. The rig is equipped with a 3D laser scanner, which provides accurate measurements of the wheel surface.

In this chapter, measurements by the laser scanner are presented initially. The outputs are related to the surface asperities, surface roughness, and average wheel profiles. Wheel wear, which is one of the top interests among the researchers and industry can be precisely estimated using the laser scanner. Comparing average wheel profiles gives a reasonable estimate of the influence of wear on the wheel surface. A baseline experiment is performed to evaluate the wheel surface condition before and after experimenting. The average wheel profile is analyzed, and the amount of accumulation of the third body layer is measured.

As discussed in the previous chapters, third body layers have a strong effect on the behavior of creep forces and traction coefficients. Therefore, it is necessary to understand how they behave and generate while performing experiments. A series of experiments were designed in order to estimate the third body layer accumulation using the laser scanner. The results show that the accumulation of the third body layer reaches a plateau after passing a transient section; however, the wheel wear continuous at a slow rate. One of the reasons might be pushing of excessive amount of generated third body layers out of the contact. At the end, the correlation between the third body layer thickness and traction coefficient is studied. Although the results are not linear, a high correlation of the traction coefficient and the third body thickness is observed.

6.2. The 3D Laser Scanner Specifications

Measuring the wheel surface profile accurately in micron levels, measurement range, and sampling frequency are among essential factors in choosing the right profile measurement unit for the rig. After some discussions with experts, utilizing two different laser scanners from two companies, the LJ-V7060B high-speed 3D laser scanner from Keyence company was chosen. The laser provides non-contact measurements using a laser leading to prevent damaging to the wheel surface that may occur in contact-type measuring sensors. The high-speed sampling rate of the scanner provides continuous measurement capability while experimenting. The scanner can accurately measure surfaces even in cases where black surfaces, inclines with low reflectivity and metallic surfaces with high reflectivity are mixed together under the same optical axis [53].

The laser light is projected in a horizontal line by the cylindrical lens and diffusely reflects on the target object. This reflected light is focused on the HSEE^3-CMOS, and by detecting changes in position and shape, displacement and shapes can be measured [53]. Some of the laser scanner specifications are summarized in Table 6.1. The related parameters are presented in Figure 6.1.

Table 6.1 A Summary of Keyence LJ-V7060B Laser Scanner Specifications

PARAMETER	VALUE
Clearance Distance	52 mm
Measurement Range	16 mm
Near Field of View (FOV)	13.5 mm
Far Field of View (FOV)	15 mm
Repeatability Z-axis (height)	0.4 μm
Repeatability X-axis (width)	5 μm
Linearity Z-axis (height)	$\pm 0.1\%$ of $\mathrm{F.S.}$
Profile Data Interval X-axis (width)	20 μm

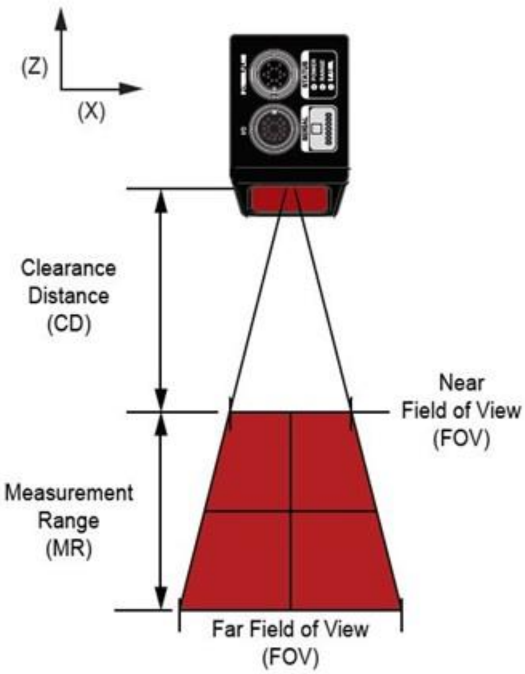

Figure 6.1 Laser Scanner Parameters [54]

The system is equipped with a laser sensor to trigger the scanner and start measuring the wheel surface. It provides a capability of measuring the wheel surface from almost the same position for each measurement. Therefore, it is possible to see the effect of test parameters on any section of the wheel by comparing the wheel surface before and after experimenting. A photo of the laser scanner and laser sensor is shown in Figure 6.2.

The laser scanner positioning system consists of two precise rail sliders. By using the sliders, the laser scanner position can be adjusted in a 2D plane. One of the sliders moves the camera along the wheel axis to be able to capture the desired portion of the wheel. The other one can be used to adjust the distance between the wheel and the laser camera, i.e., position the wheel in the measurement range. The positioning system is shown in Figure 6.2.

After positioning the laser camera precisely and start rotating the wheel, the laser scanner triggers to capture the wheel surface by using the laser sensor output. Sometimes, it is needed to measure a portion of the wheel instead of capturing the whole wheel surface to increase measurement accuracy, e.g., contact patch geometry studies. In this case, the laser scanner can be triggered manually to measure any portion of the wheel.

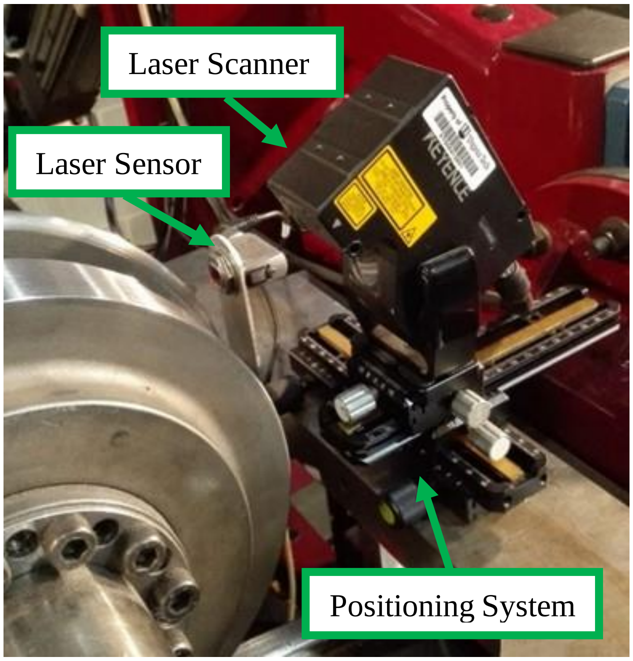

Figure 6.2 Laser Scanner System Mounted on the Rig

Some applications of the laser scanner on the roller rig are:

- Measuring the wheel surface height,
- Studying the effect of test parameters on groove dimensions,
- Analyzing the plastic deformation of the wheel for contact patch studies,
- Measuring the third body layer accumulation,
- Calculating the surface roughness of the wheel surface,
- Evaluating the wheel roundness,
- Detecting any defect or flat spots that may exist on the wheel surface,
- Measuring the wheel surface profile.

6.3. Wheel Surface Measurements and Surface Roughness Calculations

The 3D wheel surface topography describes the micro-scale features of the wheel surface. It can be achieved efficiently by capturing the 3D spatial coordinates of points on a surface using the laser scanner. Besides, any defects that may exist on the wheel surface can be observed clearly on the 3D surface. Figure 6.3 (left) illustrates a 3D wheel surface topography. The image shows the asperities and valleys on the wheel surface in micron levels.

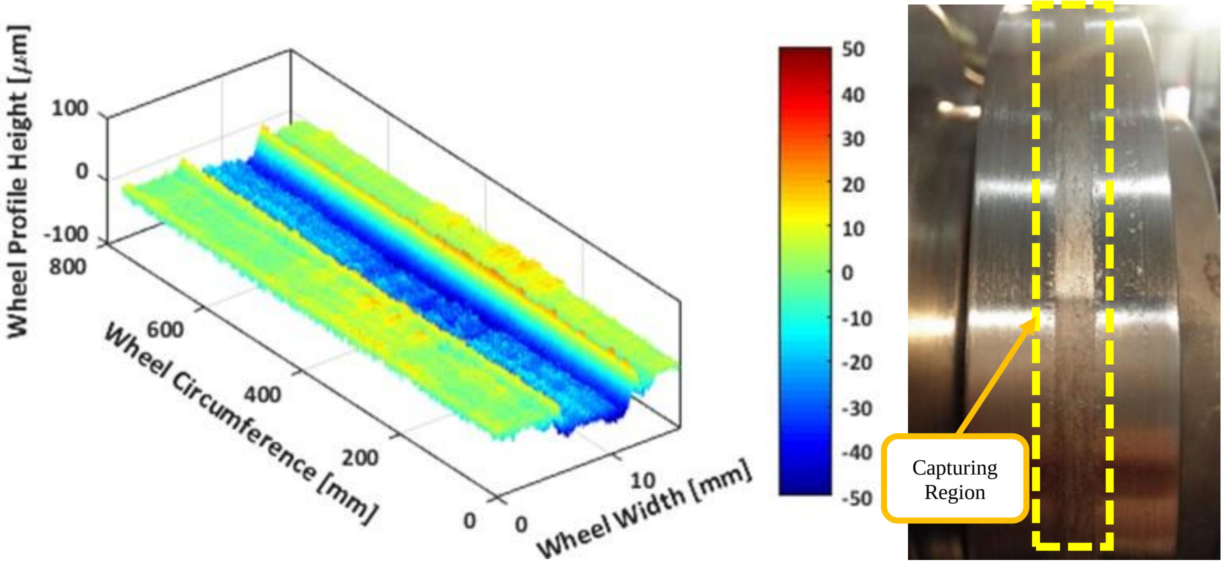

Figure 6.3 3D Wheel Surface Metrology (Left) - Actual Wheel Image (Right)

The blue region, which corresponds to the wear band after several successive runs, shows the groove formed on the wheel surface. The red and yellow colors are related to the peaks and regions with higher heights. The 3D surface topography is presented along the wheel circumference for one complete revolution.

The wheel surface profile can be calculated by averaging all the data along the wheel circumference. It means that all data points with the same distance from measurement gauge are averaged and considered as the wheel profile datum for the corresponding point. After calculating all data for each point in the wheel width direction, the average wheel profile is derived. The wheel profile, which is shown in Figure 6.4, can be used as a representative of the wheel surface condition for further analysis. A 2D image of the wheel surface is generated and provided in Figure 6.4. The peaks and bottoms of the wheel surface can be identified by considering hot and cold colors.

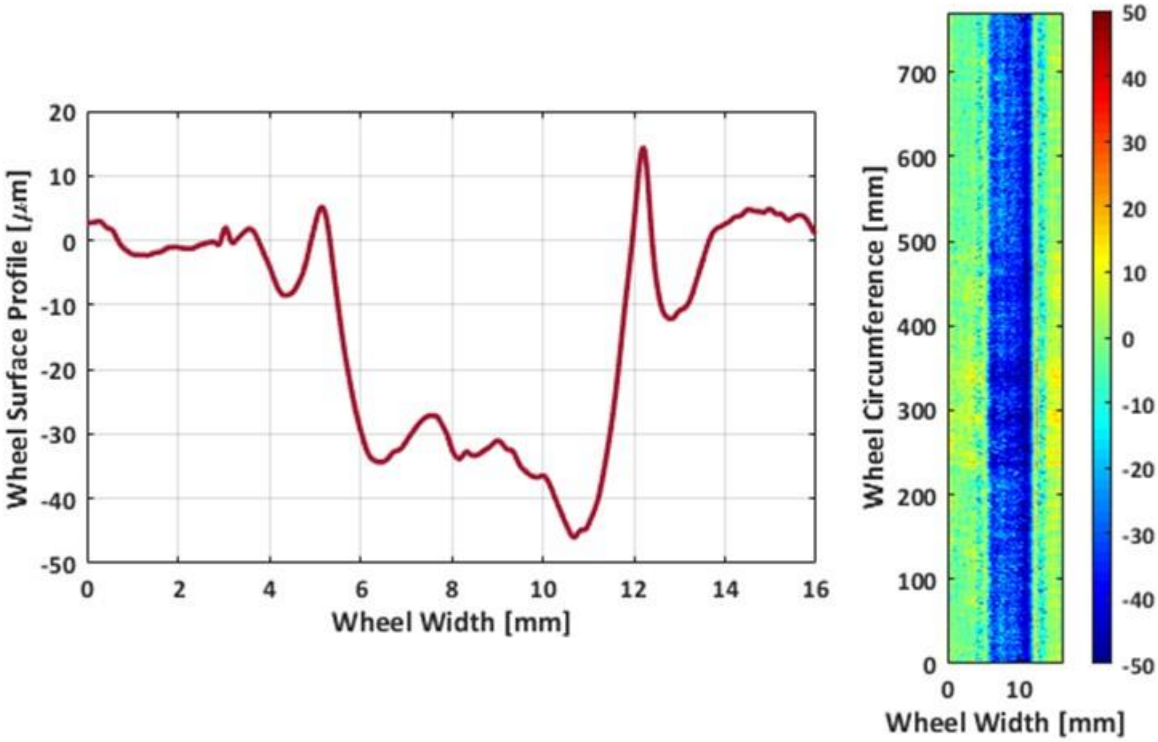

Figure 6.4 Wheel Surface Profile (Left) - 2D Wheel Surface Image (Right)

Roughness is an essential factor in determining how the wheel will interact with the roller and how it affects the creep forces and traction coefficients. Since all the surface data is available, the surface roughness of the wheel can be assessed using several methods such as R_a and R_q. There are many different parameters to evaluate the surface roughness of a surface, but R_a is the most common. R_a, which is the arithmetical mean deviation of the profile is provided in (6-1).

$$R_a = \frac{1}{n}\sum_{i=1}^{n}|y_i| \tag{6-1}$$

where y_i is the vertical distance from the mean line to the i^{th} data point and n is the total number of points, which are equally spaced along the trace. R_q is another representation of the surface roughness. It is calculated as the square root of the arithmetic mean of the square of the vertical deviation from the mean line provided in (6-2).

$$R_q = \sqrt{\frac{1}{n}\sum_{i=1}^{n}{y_i}^2} \tag{6-2}$$

At each data point on the wheel width direction, the surface roughness representatives, R_a and R_q, are calculated and plotted in Figure 6.5.

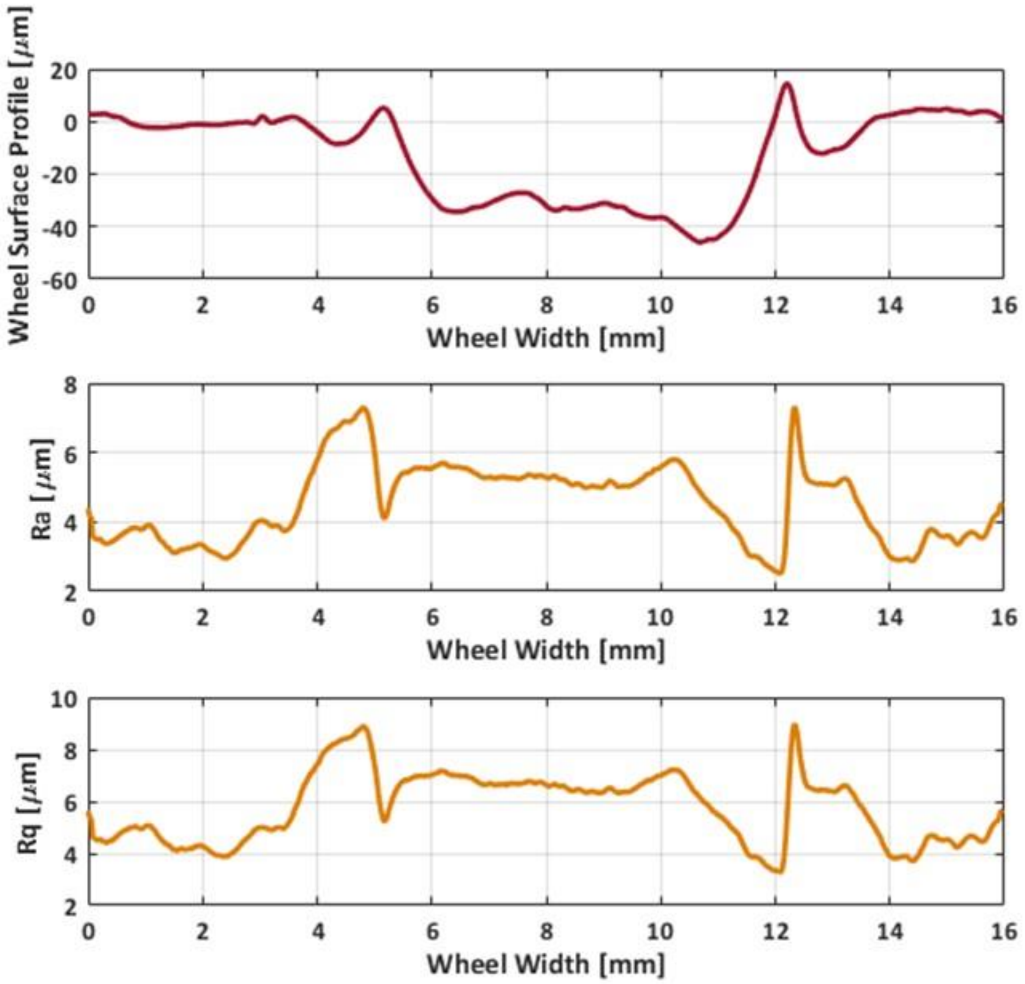

Figure 6.5 Wheel Profile (Top) - R_a (Middle) - R_q (Bottom)

6.4. Evaluating the Wheel Surface Evolution for a Baseline Experiment

One experiment was designed and performed on the roller rig to evaluate the wheel surface evolution. The experiment has been conducted based on baseline conditions using a cylindrical wheel. The experiment conditions are provided in Table 6.2. The wheel surface topography is provided using the laser scanner in three different steps of the experiment. Before experimenting, the wheel surface was captured when the surface was clean with no dust or debris. After experimenting, the wheel surface was measured in two steps, with third body layer accumulation at contact, and after cleaning. Comparing the wheel surface profiles in these three steps provides valuable information about the wheel surface evolution, the amount of third body layers generated at contact, and the level in which the wheel is worn.

Table 6.2 Test Conditions for Wheel Surface Evolution Study

TEST PARAMETER	VALUE

Wheel Profile	Cylindrical
Roller Profile	US-136 rail
Angle of Attack (°)	0
Cant Angle (°)	0
Field Speed (km/h)	3.0
Rig Wheel Load (kN)	9.6
Full-Scale Wheel Load (kN)	153.6
Commanded Creepage (%)	2.0
Initial Surface condition	Clean and Dry

Figure 6.6 shows the wheel surface images captured by the laser scanner before experimenting. The cylindrical wheel was previously used in several experiments for different purposes. The wheel surface consists of sections of asperities and valleys. Valleys show the part of the wheel that the most wear has occurred. Probably most of the experiments have been performed in these regions previously. On the other hand, fewer runs are conducted in the range of three to ten millimeter of the wheel width, which is shown in Figure 6.6. For this experiment, the roller was placed in a way that the trace of the roller locates in this range in order to visualize the experiment results better.

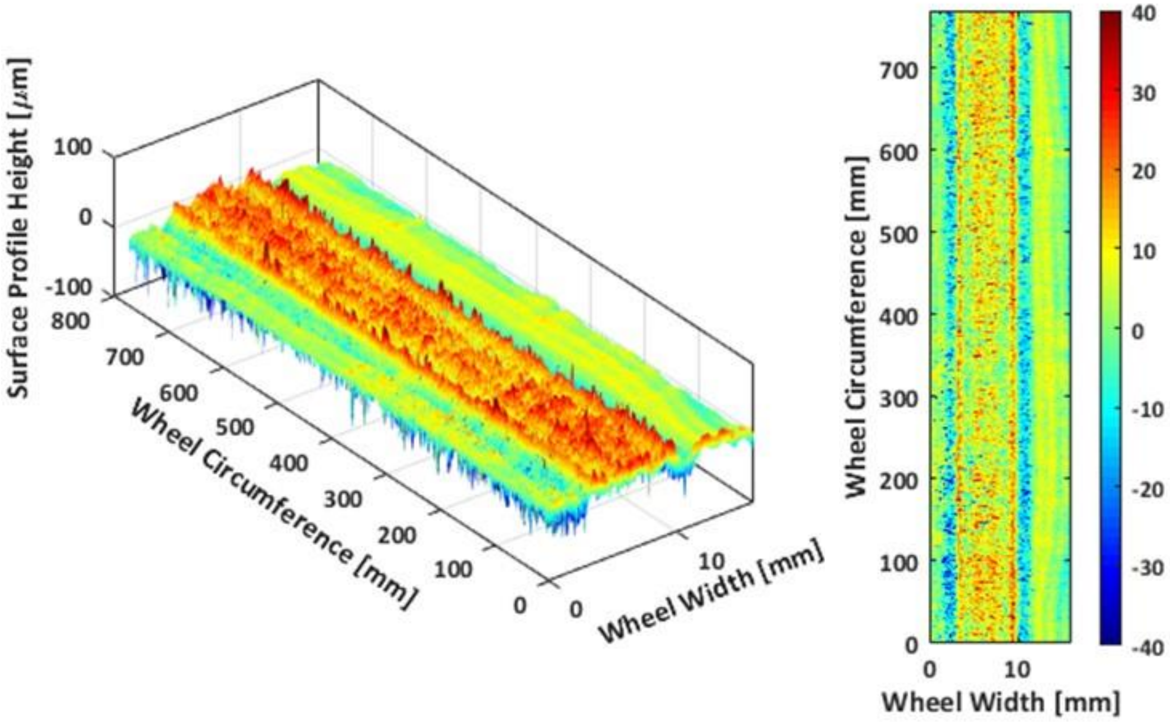

Figure 6.6 Wheel Surface Images Before Experimenting, 3D (Left), and 2D (Right)

The experiment is conducted for 500 seconds. During experimenting, the worn materials and oxides are accumulated at contact. As discussed in the previous chapters, it seems that the worn materials and oxides, which are called third body layers, act like friction modifiers and change the behavior of the creep forces and traction coefficients at contact. The traction coefficients tend to increase while third body layers are built up at contact during the experiment. Figure 6.7 shows the wheel surface topography after performing the experiment when the wheel is still covered by the third body layer. As discussed, the roller was located in the region of high asperities of the wheel. Therefore, this portion of the wheel is covered with third body layers due to successive runs of wheel on the roller. Red colors in the middle region show the amount of third body layers accumulated on the wheel surface. Calculating the wheel profile for the second step, after experimenting with third body layer, provides valuable estimation of the accumulation of the third body layers after conducting an experiment under baseline conditions. The wheel profile is provided in Table 6.2.

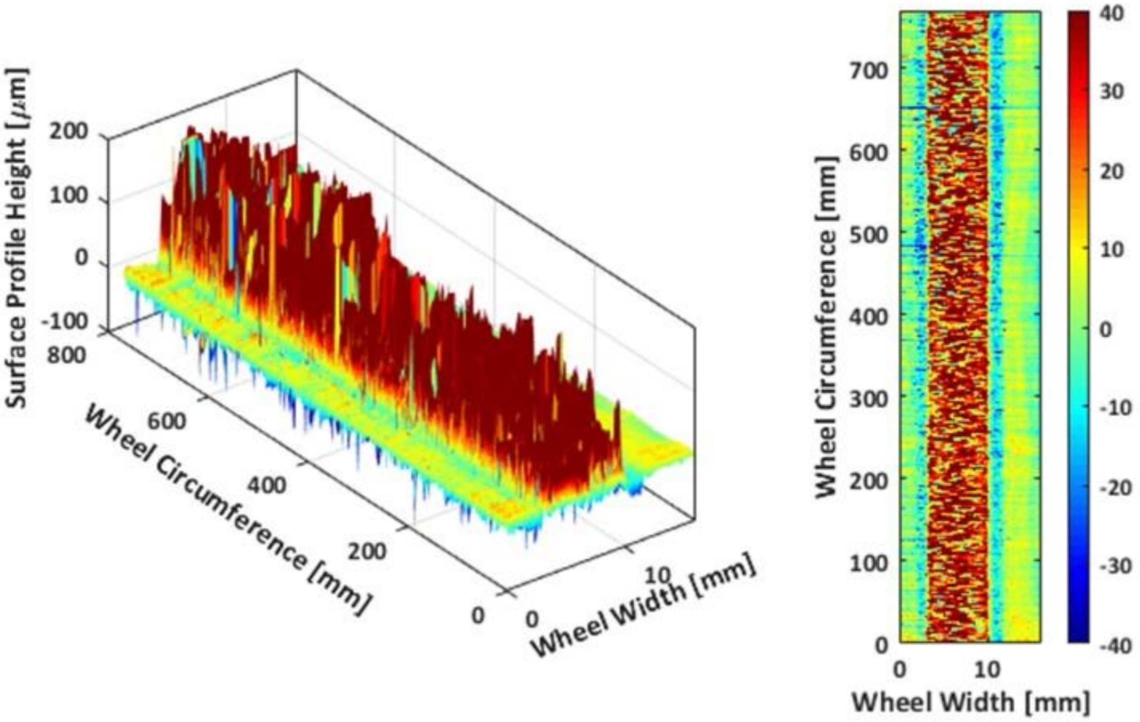

Figure 6.7 Wheel Surface Images After Experimenting Covered with Third Body Layer, 3D (Left), and 2D (Right)

Besides the information that can be obtained from the previous steps, the wheel wear can be estimated after cleaning the wheel surface and comparing the results with the first step of capturing the wheel surface. Therefore, the final profile of the wheel surface is calculated based on the wheel surface metrology obtained after cleaning the wheel surface and removing any debris and third body layers that existed at contact. The groove shape is another important feature of the experiments, which affects the creep forces. It is possible to analyze the change in groove shape by comparing the results of the first and third steps when the wheel is clean. The first step provides information about the wheel profile before experimenting, and the third step presents data to evaluate the wheel profile after experimenting. Figure 6.8 shows 3D and 2D images of the wheel surface topography after performing the experiment and cleaning the surface.

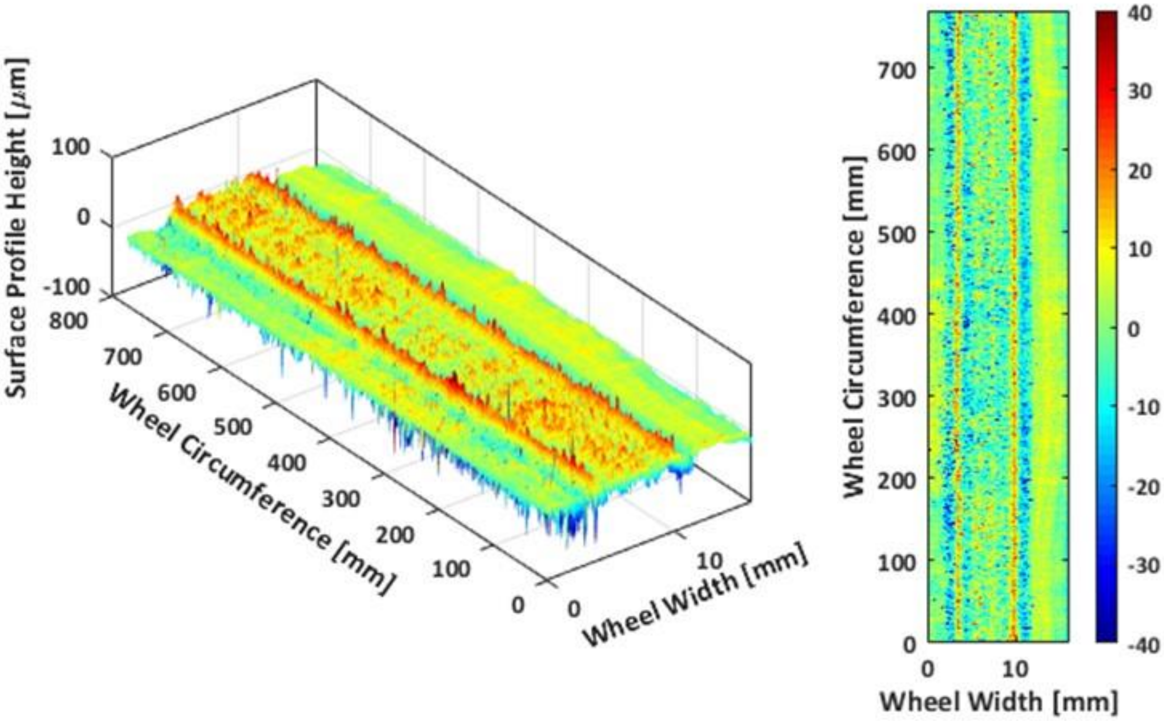

Figure 6.8 Wheel Surface Images After Experimenting under Clean Condition, 3D (Left), and 2D (Right)

The wheel profiles calculated in three steps are presented in Figure 6.9. The solid orange curve is related to the wheel surface profile before experimenting. At this step, the wheel is clean with no dust or debris. After experimenting, the wheel surface is accumulated with third body layer shown with a gray dashed curve. The final profile, which is a dot-dashed maroon curve illustrates the wheel surface profile formed during experiment. The difference between this curve and the initial one provides information about the wheel wear. Also, comparing wheel surface profiles after experimenting specifies the accumulation of the third body layer at contact.

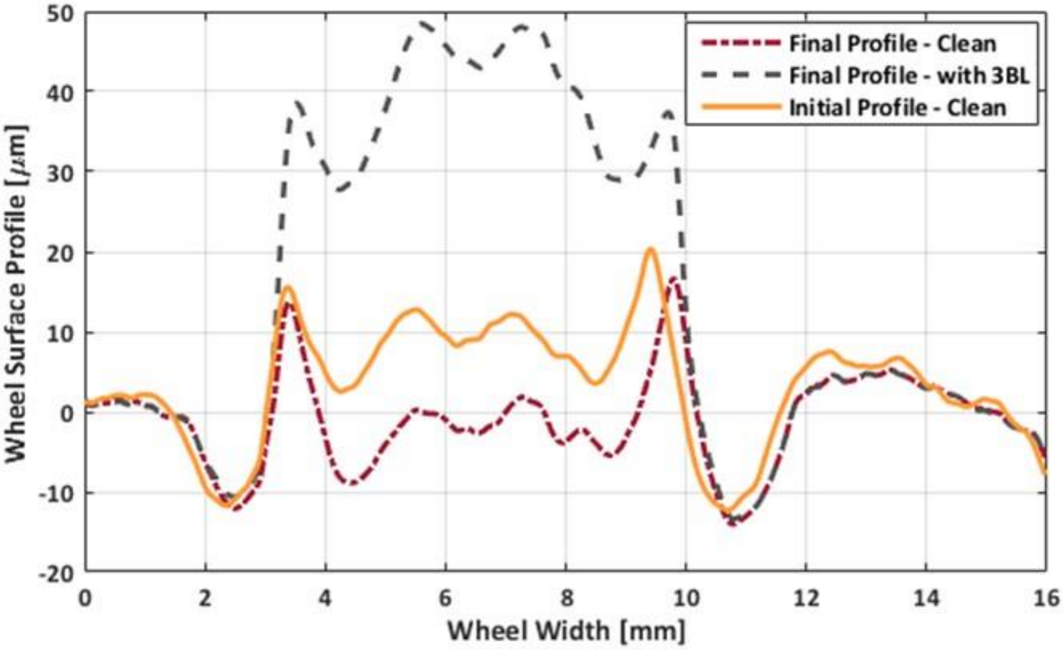

Figure 6.9 Wheel Surface Profiles for the Baseline Experiment

6.5. Estimating the Third Body Layer Thickness and its Relation to Traction Coefficient

While running an experiment, a third body layer generates between the wheel and the roller. The worn materials and oxides either accumulate on the wheel and roller surfaces or are thrown out of contact. It seems that the oxides and debris, which remain on the wheel and roller surfaces are vital factors in changing the behavior of creep forces and traction coefficients. In this chapter, the behavior of the third body layer thickness is estimated, and the result is correlated with the transient traction coefficient.

6.5.1. Measuring the Wheel Surface Profile Covered with Third Body Layer

An experiment is designed and performed to measure the wheel surface successively while generating worn materials and oxides. It is needed to measure the wheel surface several times during the experiment to be able to evaluate the third body layer formation. The baseline experiment under conditions mentioned in Table 6.2 is conducted for 500 seconds. The wheel surface is captured several times, before experimenting, while experimenting, and after 500 seconds. During the experiment, the wheel surface topography is assessed every 20 seconds to record any changes that occur to the wheel surface.

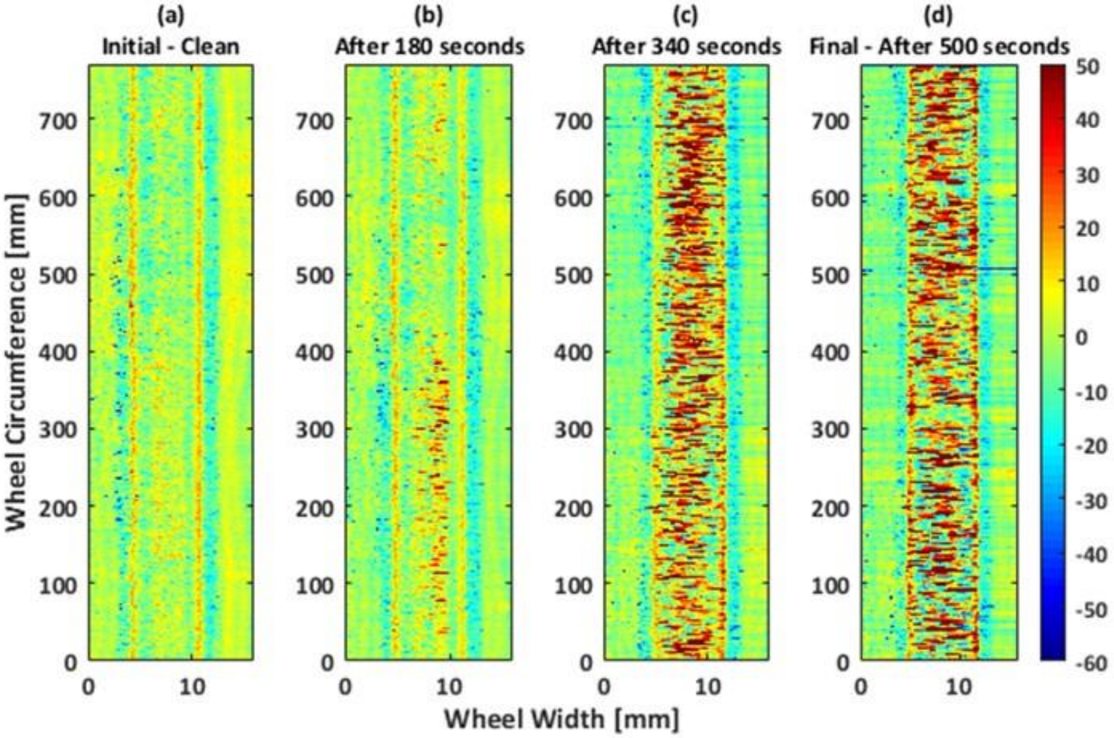

Figure 6.10 Wheel Surface Profile Changes Over Time, Covered with Third Body Layer

Figure 6.10 shows four sample captures of the wheel surface using the laser scanner. The (a) and (b) images are captured before and after experimenting. Two other sample images presented in Figure 6.10 (b) and (c) are related to the wheel surface metrology at 180 seconds and 340 seconds, respectively. The red points show the high asperities in the wheel profile due to the third body layers generated at contact. The images show the progression of the wheel profile during the baseline experiment. It is noted that the wheel surface remained unclean while capturing using the laser scanner. Furthermore, the wheel surface profile can be calculated at each measuring step and compared to the wheel profile at the beginning of the experiment.

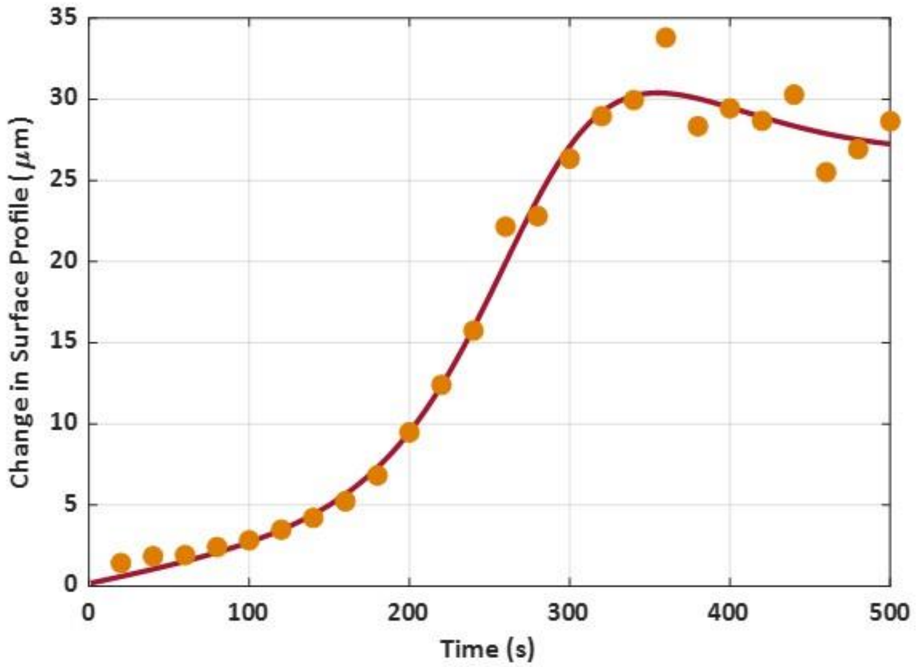

Figure 6.11 shows the evolution of the wheel surface profile relative to the initial surface at the beginning of the experiment. Each point in this figure is calculated as follow:

- The wheel surface is measured using the laser scanner.
- The average profile is calculated.
- The area surrounded by wheel surface profile and the initial surface profile in the wear band is calculated. It is shown as the green region in Figure 6.12.
- The area is normalized by the width of the wear band.

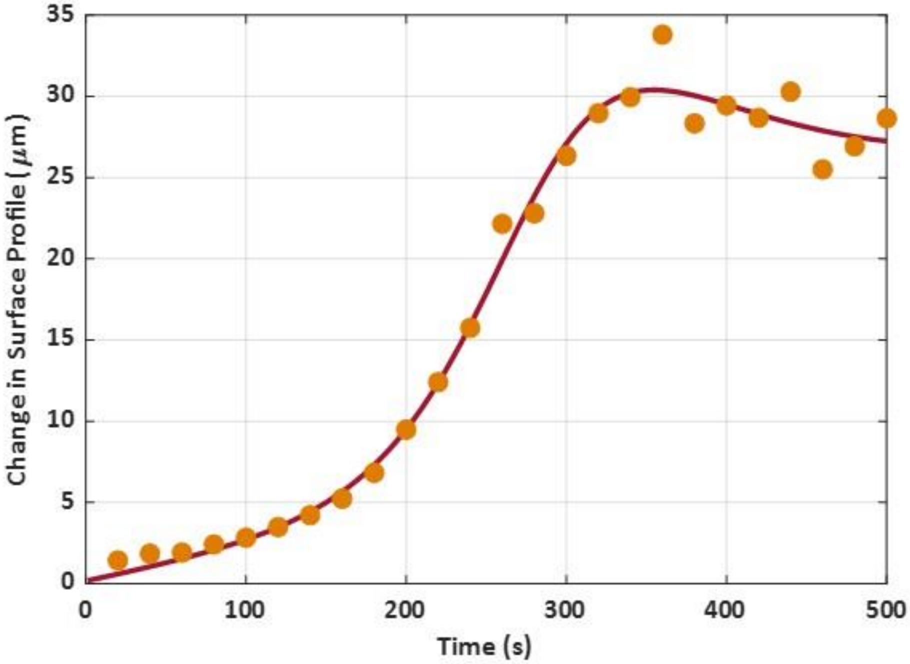

Figure 6.11 Surface Profile Change Relative to the Initial Profile

Although the difference between the profiles provides information about the wheel wear, it lacks an accurate estimation of the third body layer accumulation. Another critical information needed to accurately estimate the third body layer accumulation is the real-time amount of wheel wear. To estimate the third body layer thickness, it is essential to evaluate the area of the blue region, as well. In fact, the total area of the green and blue regions, presented in Figure 6.12, shows the accumulation of third body layers. The blue region is related to the amount of wheel wear. For the current experiment, the wheel surface remained unclean in between successive laser scanner measurements. Therefore, the wheel surface data related to the blue region was not accessible. To be able to estimate the third body layer accumulation, another set of experiments was designed in order to evaluate the blue region in the wear band.

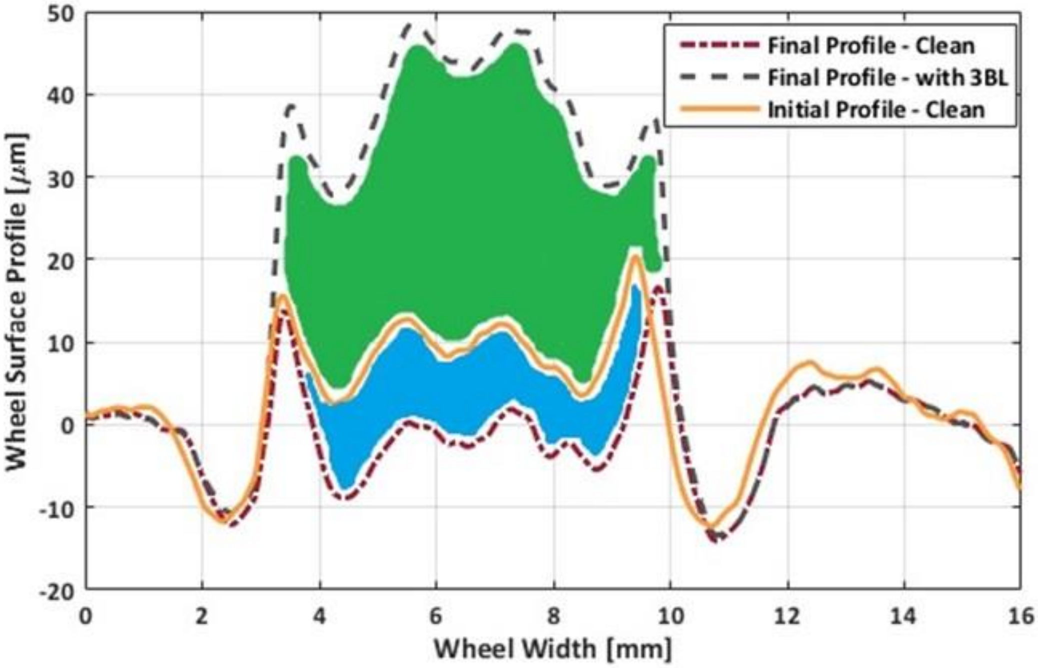

Figure 6.12 Regions Needed to be Considered to Estimate the Third Body Layer Thickness

6.5.2. Estimating the Wheel Surface Change Due to the Wheel Wear

In order to estimate the real-time wheel wear during experimenting, the wheel surface should be cleaned before capturing the surface using the laser scanner. The experiment duration was increased progressively from one surface measurement to another to record wheel wear for each test duration. Therefore, twenty-five experiments are conducted under the same conditions as the previous experiment mentioned in Table 6.2 except for the duration of each experiment and wheel surface cleaning condition. The experiments durations are progressively increased from 20 seconds to 500 seconds with a 20-second time step, i.e., the experiments are performed at 20 seconds, 40 seconds, 60 seconds, etc. Before experimenting, the wheel surface was captured when it was clean. For each twenty-five experiments in which the laser scanner measurement is conducted, the wheel surface is measured when the wheel surface is accumulated with the third body layer and after cleaning.

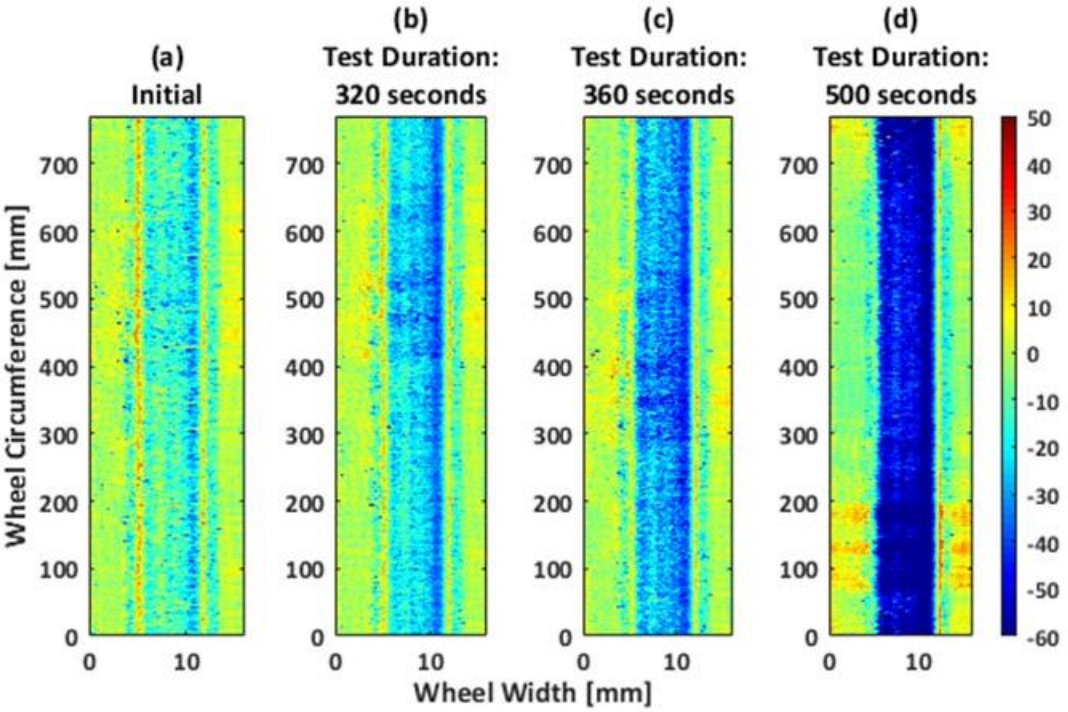

Figure 6.13 Wheel Surface Profile Changes Caused by the Wheel Wear with respect to the Test Duration

Figure 6.13 presents four samples of wheel surface topography captured when the wheel is cleaned after each experiment. Progression of blue areas shows that the groove gets deeper after some successive runs of the wheel on the roller.

Figure 6.14 shows all the wheel surface profiles calculated from the wheel surface metrology in clean conditions. The figure clearly shows the evolution of the wheel surface due to the wheel wear; however, the change in the wheel surface profile is not linear.

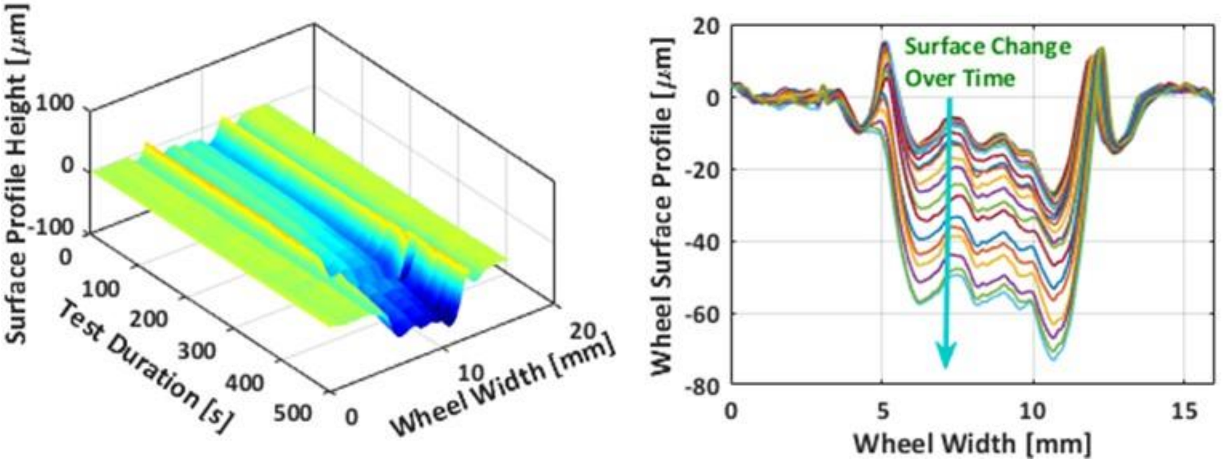

Figure 6.14 Wheel Surface Profile Change After Each Experiment – 3D Plot (Left), 2D Wheel Profile (Right)

Based on the wheel surface profiles provided in

Figure 6.14, the normalized area of the blue region, shown in Figure 6.12, over the wear band is calculated. The calculated value for each experiment is illustrated in Figure 6.15 for each test duration.

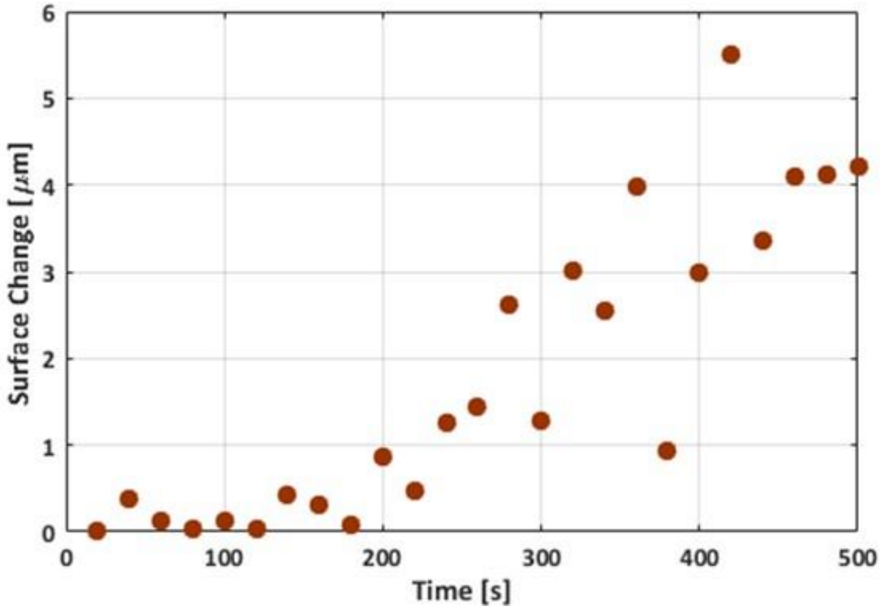

Figure 6.15 Average of the Wheel Wear on the Wheel Surface in the Running Band

As discussed, the total area of the green and blue regions in Figure 6.12 demonstrates the accumulation of the third body layer on the wheel surface. Although the data points in Figure 6.15

give a reasonable estimation of the wheel wear, the comparison of the current results with the results in

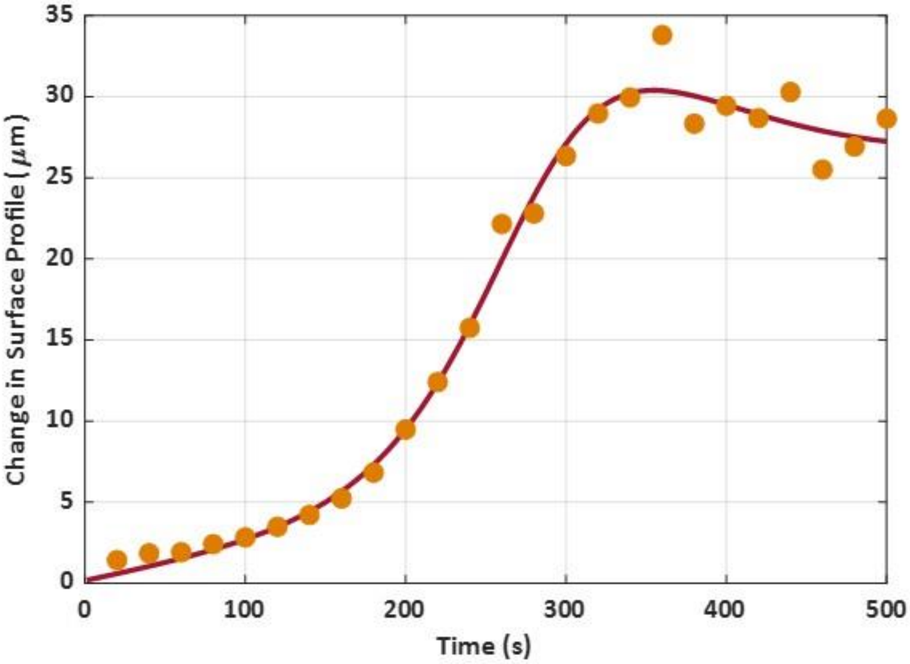

Figure 6.11 does not seem to give a reliable and accurate estimation of the third body layer accumulation. Wheel and roller surface conditions play vital roles in resulting creep forces and traction coefficients under specified test conditions. Therefore, the change in the nature of the wheel surface should be considered to accurately evaluate the third body layer accumulation during a single experiment. Each of twenty-five experiments has been performed on the wheel and roller with a slight change in the surface, which more or less affects the behavior of creep forces and traction coefficients. In other words, the results for the average wheel surface profile changes should be modified and adjusted in order to be able to evaluate the third body layer accumulation accurately.

To be able to estimate the real-time third body layer accumulation, the normalized area of the green region, shown in Figure 6.12, was selected as a representing factor for the experiments. The factor is matched in both measurements conducted on the first single experiment for determining the accumulation of third body layers and the second set of progressive experiments. On the other hand, the time in which a specific amount of wear occurs is determined based on comparing the normalized area of the green region of experiments. Figure 6.16 shows a flowchart of the process.

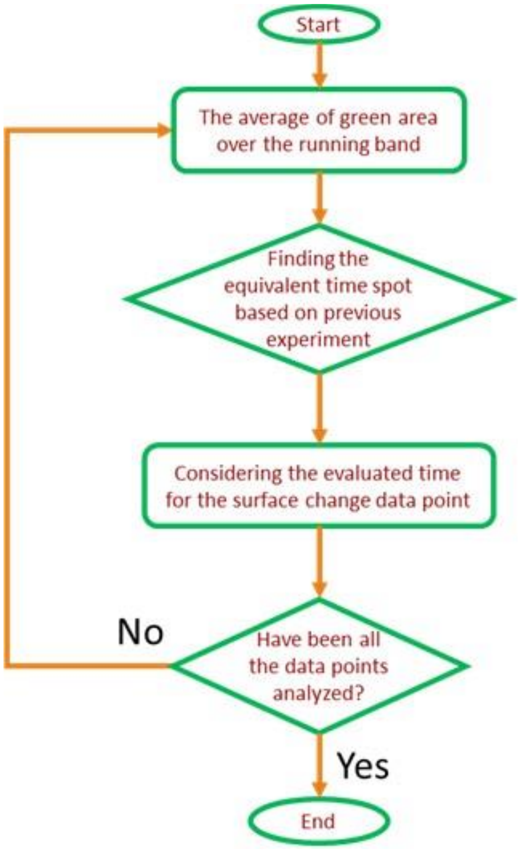

Figure 6.16 Flowchart of Determining the Time in Which a Specified Amount of Wear Occurs

After estimating the corresponding time for the wheel wear in all the twenty-five experiments, the real-time evolution of the wheel wear can be evaluated.

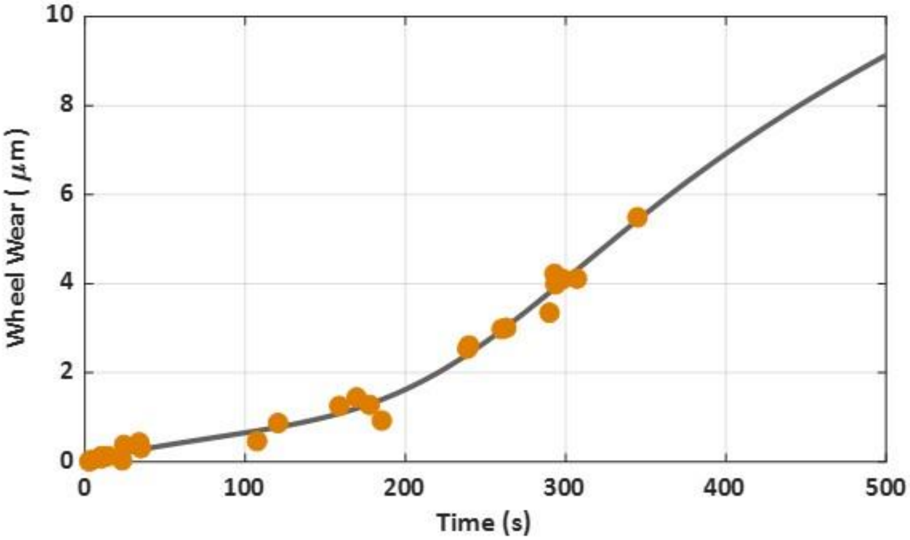

Figure 6.17 shows all the time-adjusted points of the wheel wear.

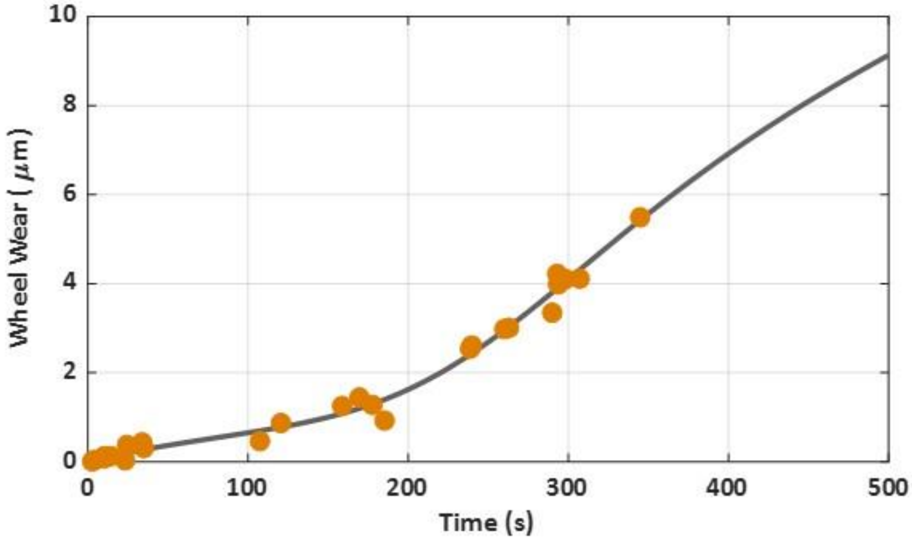

Figure 6.17 Time-Adjusted Wheel surface Change Due to the Wheel Wear

The fitted curve on the data points in

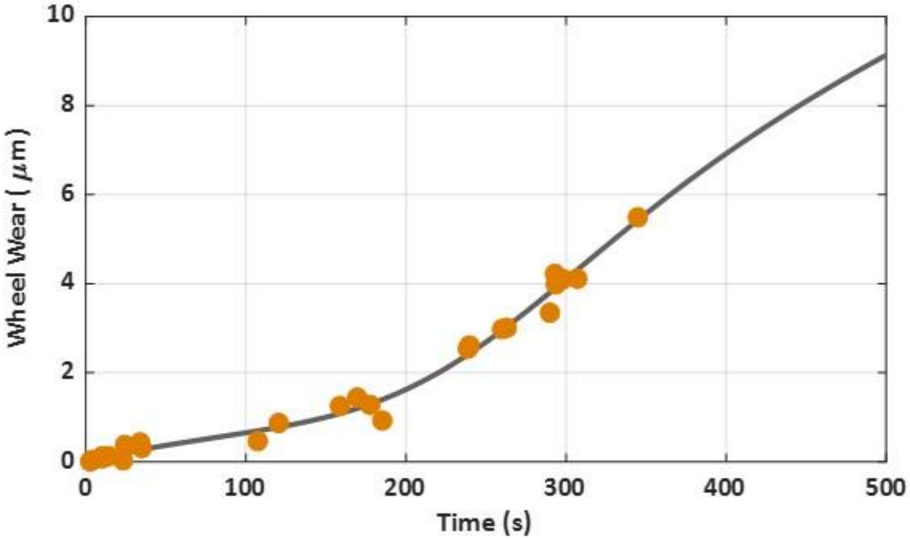

Figure 6.17 represents an estimation of the wheel wear during a single experiment with specific conditions mentioned in Table 6.2, which is an approximation of the normalized area of the blue region illustrated in Figure 6.12. The third body layer accumulation, which corresponds to the total area of green and blue regions, can be obtained by considering the results derived from all experiments performed in this section.

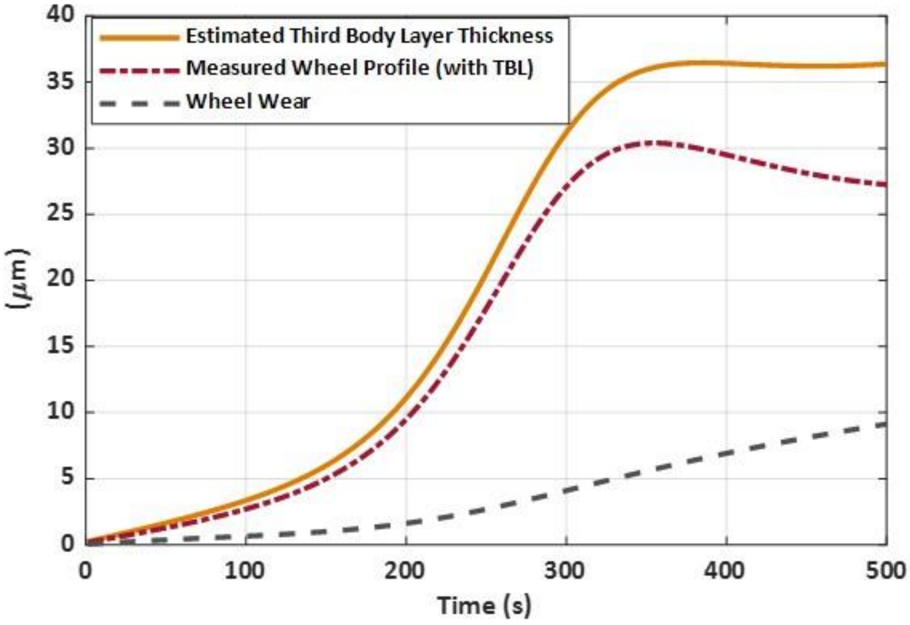

Figure 6.18 The estimation of Third Body Layer Thickness During a Single Experiment Under Baseline Conditions

The orange dash-dotted curve presented in

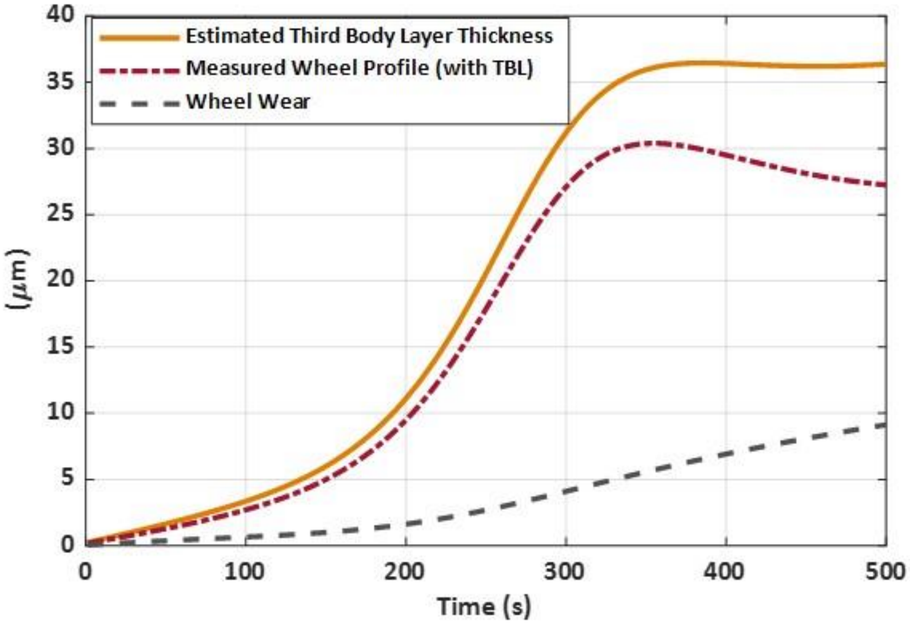

Figure 6.18 is the real-time wheel surface evolution obtained in

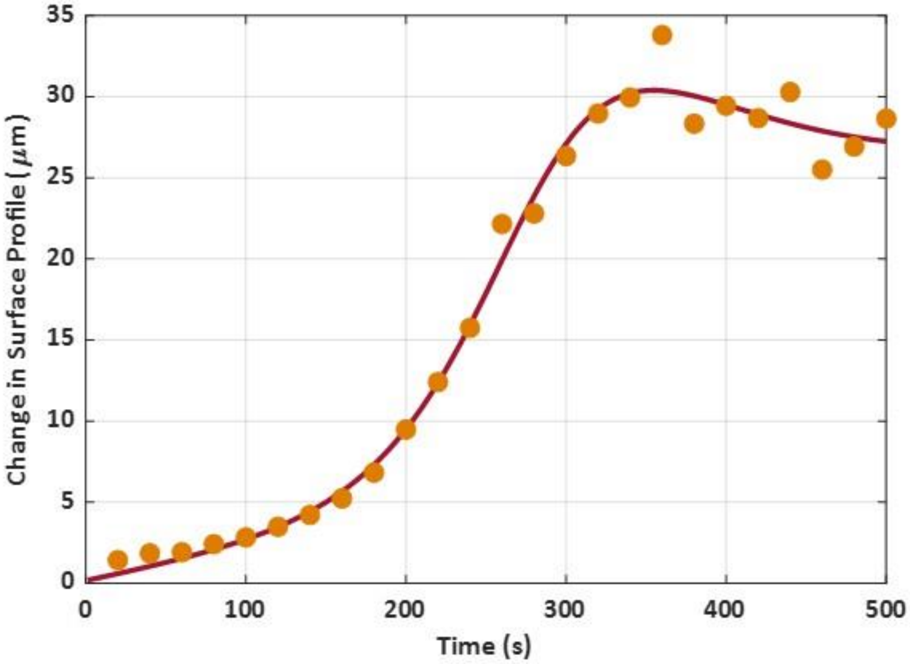

Figure 6.11. The dashed gray curve is related to the wheel wear, which was derived in

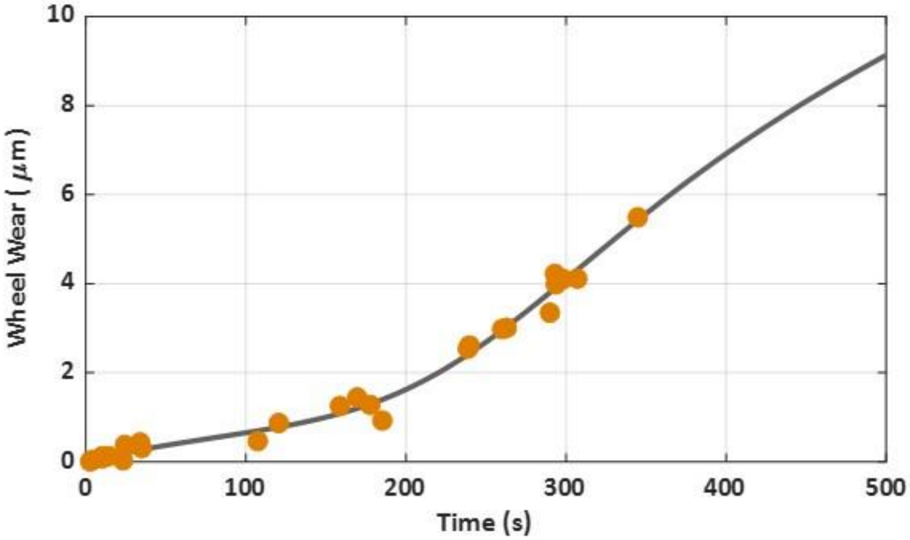

Figure 6.17. This curve shows the normalized area of the blue region within the wear band. The sum of these two curves, which is an estimation of third body layer accumulation is presented as the maroon curve. Based on the estimation, the third body layer accumulation starts to increase at a slow rate at the beginning of the experiment. It slopes up rather steeply after approximately 150 seconds, and finally it reaches a peak after a particular time.

After estimating the third body layer accumulation, the correlation between traction coefficient and third body layer thickness can be calculated. Correlation is the degree of association between two variables. The Pearson correlation was developed by Pearson in 1896. The correlation coefficient between two variables, x, and y, can be defined as equation (6-3) [55].

$$r = \frac{\sum(x_i - \bar{x})(y_i - \bar{y})}{\sqrt{\sum(x_i - \bar{x})^2}\sqrt{\sum(y_i - \bar{y})^2}} \tag{6-3}$$

where x_i and y_i are data points related to each variable. $\bar{x}$ and $\bar{y}$ are the mean of all data points for x and y, respectively. If r is the unity, there is a perfect fit with all data points. If the coefficient is zero, it means that there is no relationship between two variables.

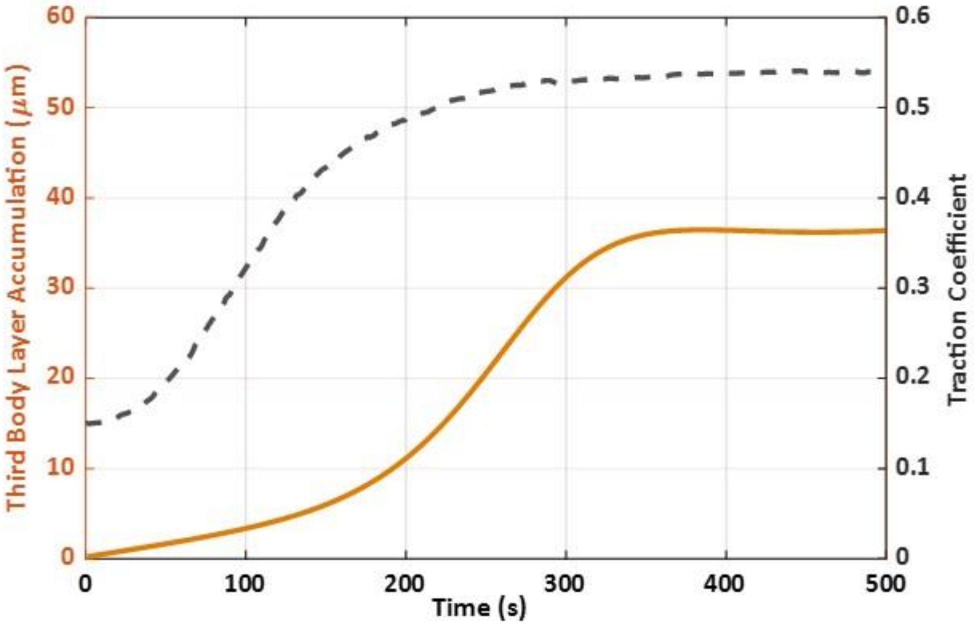

Figure 6.19 Estimated Third Body Layer Thickness and Calculated Traction Coefficient

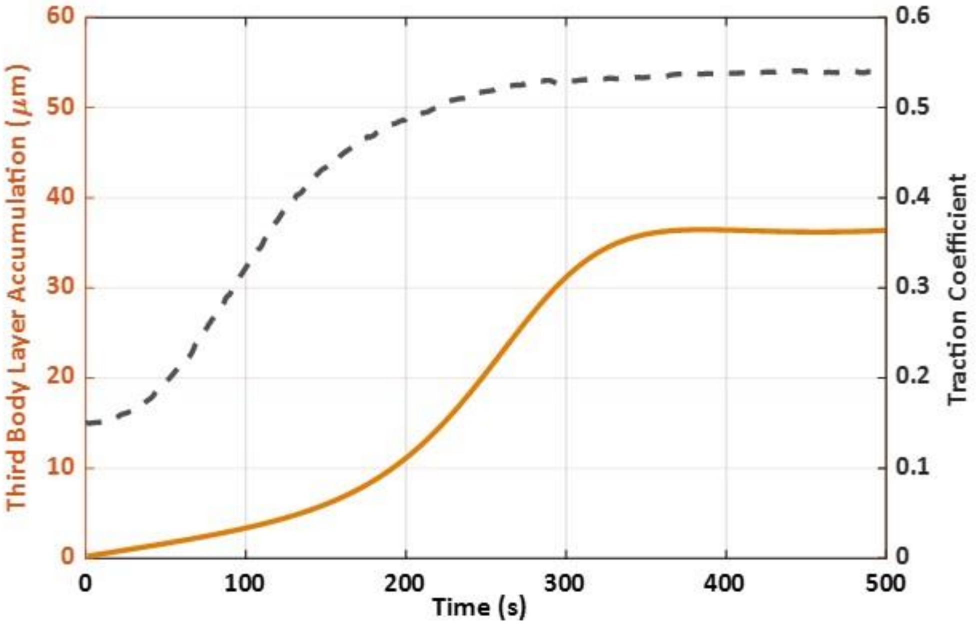

Figure 6.19 shows the real-time third body layer accumulation and calculated traction coefficient co-plotted together. At the beginning of the experiment, where a small amount of third body layer is generated at contact, the traction coefficient has a steep rise. The presence of the third body layer has affected the traction coefficient significantly and increased the coefficient to more than 0.5. The correlation coefficient for these two variables is calculated. For the total duration of the experiment, the correlation coefficient is 0.8442; however, if the transient region for third body layer is considered (between 150 seconds and 350 seconds time interval), the correlation coefficient would be 0.9237. It shows that high correlation between the third body layer thickness and traction coefficient.

6.6. Summary

In this chapter, the new feature of the rig, the laser scanner, is presented. By using the laser scanner, the wheel surface condition can be analyzed with a high level of accuracy. Presence of this remarkable feature for the rig along with precise measurements of creep forces at contact makes the VT-FRA roller rig a unique rig in the world to evaluate various scenarios in railroads. Estimating third body layer accumulation, and its effects on traction coefficients and creep forces are among the crucial topics in railroads. By using the laser scanner, an accurate measurement of the wheel surface is provided. A wheel surface profile, which is a representative of a wheel surface topography is calculated and used to study the effect of test parameters on the wheel surface change. At the end, it is concluded that there is a high correlation between the traction coefficient and the third body layer accumulation.

7. Contact Patch Shape Estimation

7.1. Introduction

In this chapter, the comprehensive analysis of the wheel-rail contact patch on the VT-FRA roller rig is provided. Hertz's theory [56] is still widely used in the railroad industry to estimate wheel-rail contact shape under several assumptions. Based on these assumptions, the wheel and roller have completely elastic behavior with no plastic deformation, and the contact surfaces are smooth, and there is no friction between them. Based on the theory, the contact geometry is estimated to be elliptical with semi-ellipsoid normal pressure distribution.

There are several parameters needed to be considered to obtain contact patch shape such as contact profiles, contact angle, normal force. To estimate the contact patch geometry on the rig, the scaled AAR-1B profile and the roller geometry are considered. The wheel and roller profiles are one-fourth scaled of actual AAR-1B wheel and AREMA-136lb rail geometries. It is assumed that contact occurs at the tapered section of the wheel profile at all contact angle conditions. The roller profile consists of several arcs with different radii. Accordingly, it is possible that a contact patch shape locates on two arcs of the roller at some contact angle ranges. Besides, contact angle changes the contact position on the wheel and the roller and causes normal force variations, i.e., it is needed to take the contact angle as an essential factor for calculations. Contact angles considered for this study are in the range of the VT-FRA roller capabilities. The rig is capable of changing the cant angle between $-6°$ and $+6°$.

Based on calculations and estimations, the relationship between average contact pressure, contact angle, and wheel load is estimated. At negative contact angles, the contact patch locates on the small radius arc of the roller, i.e., smaller contact patch area, causing the average contact pressure to increase. The contact patch ellipse has a smaller aspect ratio while contacting at the bigger profile arc radius. At small profile arc radii, the contact patch looks thinner with a higher aspect ratio.

7.2. Summary of Hertz's Theory Formulation to Estimate Contact Patch Dimensions

By using Hertz's theory, the contact patch area and contact pressure distribution can be carried out under several assumptions. Some of the key assumptions to develop Hertz's theory are [57]:

- The kinematic equations and the materials elastic properties are linear,
- Wheel and rail materials exhibit completely elastic behavior (no plastic deformation),
- Wheel and rail materials are homogeneous, and their properties are isotropic,
- The contact surfaces are perfectly smooth, and there is no friction between them,
- Contact surfaces curvature is constant within the contact patch,
- Contact surfaces radii of curvature are much larger than the dimensions of the contact patch.

The contact patch is estimated to have an elliptical shape with semi-ellipsoid normal pressure distribution. The distance between two opposing points on wheel and rail can be defined by a quadratic expression in the x-y plane, which is presented in equation (7-1).

$$D(x,y) = Ax^2 + By^2 - d \tag{7-1}$$

where

$$A = \frac{1}{2}\left(\frac{1}{R_{wx}} + \frac{1}{R_{rx}}\right) \tag{7-2}$$

$$B = \frac{1}{2}\left(\frac{1}{R_{wy}} + \frac{1}{R_{ry}}\right) \tag{7-3}$$

where R_{wx} and R_{wy} are longitudinal and lateral radii of curvature of the wheel profile at the contact point. Similarly, R_{rx} and R_{ry} are longitudinal and lateral radii of curvature of the roller profile at the contact point. d is the depth of penetration.

The major (a) and minor (b) axes of the contact ellipse are defined as [58]:

$$a = m\left(3\pi N \frac{K_1 + K_2}{4K_3}\right)^{1/3} \tag{7-4}$$

$$b = n\left(3\pi N \frac{K_1 + K_2}{4K_3}\right)^{1/3} \tag{7-5}$$

where N is the normal force at contact. K_1, K_2 are coefficients related to the wheel and roller material properties, and K_3 is a coefficient of curvatures at contact. They are defined as below.

$$K_1 = \frac{1 - \upsilon_w^2}{\pi E_w} \tag{7-6}$$

$$K_2 = \frac{1 - \upsilon_r^2}{\pi E_r} \tag{7-7}$$

$$K_3 = A + B = \frac{1}{2}\left(\frac{1}{R_{wx}} + \frac{1}{R_{wy}} + \frac{1}{R_{rx}} + \frac{1}{R_{ry}}\right) \tag{7-8}$$

where υ and E are Poisson's ratio and Young's modulus, respectively. The w and r subscripts denote to the wheel and rail. The coefficients m and n are given in Table 7.1 as a function of θ, which is defined in equation (7-9):

$$\theta = cos^{-1}\left(\frac{K_4}{K_3}\right) \tag{7-9}$$

where

$$K_4 = \frac{1}{2}\left[\left(\frac{1}{R_{wx}} + \frac{1}{R_{wy}}\right)^2 + \left(\frac{1}{R_{rx}} + \frac{1}{R_{ry}}\right)^2 + 2\left(\frac{1}{R_{wx}} - \frac{1}{R_{wy}}\right)\left(\frac{1}{R_{rx}} + \frac{1}{R_{ry}}\right)\cos(2\phi)\right]^{\frac{1}{2}} \tag{7-10}$$

where ϕ is the cant angle between the wheel and the rail.

Table 7.1 Coefficients $\boldsymbol{m}$ and $\boldsymbol{n}$ for different values of $\boldsymbol{\theta}$ [58]

$\boldsymbol{\theta}$ (deg)	$\boldsymbol{m}$	$\boldsymbol{n}$	$\boldsymbol{\theta}$ (deg)	$\boldsymbol{m}$	$\boldsymbol{n}$	$\boldsymbol{\theta}$ (deg)	$\boldsymbol{m}$	$\boldsymbol{n}$
0.5	61.4	0.1018	10	6.604	0.3112	60	1.486	0.717
1.5	36.89	0.1314	20	3.813	0.4123	65	1.378	0.759
2	27.48	0.1522	30	2.731	0.493	70	1.284	0.802
3	22.26	0.1691	35	2.397	0.530	75	1.202	0.846
4	16.5	0.1964	40	2.136	0.567	80	1.128	0.893
6	13.31	0.2188	45	1.926	0.604	85	1.061	0.944
8	9.79	0.2552	50	1.754	0.641	90	1.000	1.000
8	7.86	0.285	55	1.611	0.678			

Based on Hertz's theory, the semi-elliptic normal shape distribution over the contact area is defined in equation (7-11).

$$p(x, y) = \frac{3N}{2\pi ab}\sqrt{1 - \left(\frac{x}{a}\right)^2 - \left(\frac{y}{b}\right)^2} \tag{7-11}$$

7.3. Contact Patch Geometry Analysis Based on Wheel-Rail Contact Angle

Wheel and rail profiles play essential roles in estimating contact patch shape. The wheel and roller profiles considered for calculations are one-fourth scaled-down of actual AAR-1B wheel and AREMA-136lb rail profiles. A schematic of the wheel and the rail profiles at contact is presented in Figure 7.1.

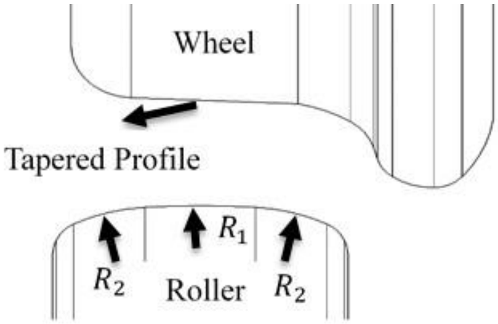

Figure 7.1 The Wheel and the Roller Profiles at Contact

Cant angle is one of the factors, which changes the normal force at contact significantly. The normal force affects the contact pressure and contact patch geometry. Therefore, it is needed to consider the cant angle limitations on the rig and estimate the regions on the wheel and roller surfaces, which tolerate contact pressures at each cant angle positioning, i.e., contact patch geometry.

In this study, it is assumed that the total contact patch shape is located on the tapered section of the wheel. For the roller, the section of the profile, which is affected by contact pressure is estimated based on cant angle limitations. According to AAR-1B wheel profile detailed drawing, the taper value can be between 1:17 to 1:23. The tapered wheel, which is mounted on the roller is has a 1:22.6 taper, which corresponds to approximately 2.5° roll angle (The angle between a line perpendicular to the taper and the vertical axis). So, if the wheel tilts 2.5° toward the vertical axis (2.5° cant angle), the normal force at contact would be equal to the wheel load.

Based on the VT-FRA roller rig capabilities, the cant angle can be adjusted between $-6°$ to $+6°$. To understand which profiles on the roller surface will be affected in the cant angle interval, the contact point was analyzed. In Figure 7.2, the maximum and minimum of cant angle are shown. The results indicate that the contact point is located in the middle profile with radius R_1, and in the right-hand roller profile with the radius of R_2.

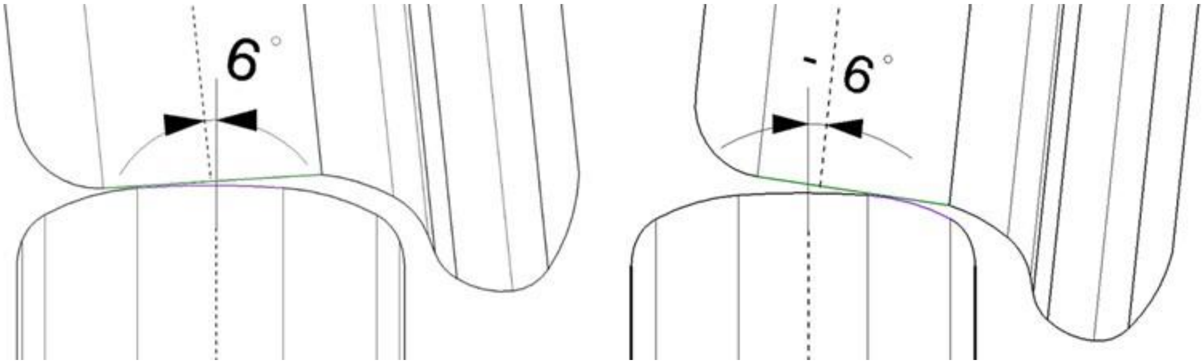

Figure 7.2 Contact Locations at $+\mathbf{6}°$ Cant Angle (Left), and $-\mathbf{6}°$ Cant Angle (Right)

Therefore, further calculations to achieve contact patch geometry are based on the tapered profile of the wheel, and the middle profile (with radius R_1) and right-hand profile (with radius R_2) of the roller. These profiles are shown in Figure 7.3.

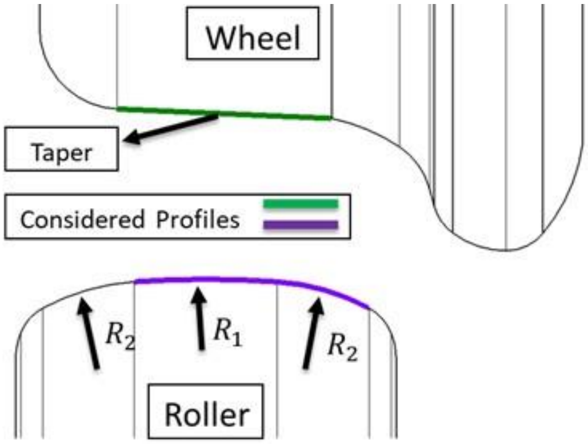

Figure 7.3 The Wheel and the Roller Profiles Considered for Contact Patch Study

7.4. Contact Patch Shape and Pressure Estimation on the VT-FRA Roller Rig

Based on the VT-FRA roller rig parameters, and contact profiles analyzed in the previous section, the parameters needed for Hertz's theory estimation can be derived. These parameters, presented in Table 7.2, are related to the wheel and the roller curvatures at contact, the normal force, and material properties required for estimating the contact patch geometry. Besides, the same material properties are assumed for the wheel and the roller.

Table 7.2 Parameters Considered for Contact Patch Geometry Estimation

Parameter	Symbol	Value
Longitudinal radius of the wheel curvature $(in.)$	R_{wx}	4.74
Lateral radius of the wheel curvature $(in.)$	R_{wy}	∞
Longitudinal radius of the roller curvature $(in.)$	R_{rx}	22.10
Lateral radius of the roller curvature $(in.)$	R_{ry}	$R_1 = 2.00$ & $R_2 = 0.44$
Module of elasticity (GPa)	E	210
Poisson ratio	υ	0.28
Normal force at contact (N)	N	Various Normal Forces

As stated in Table 7.2, the contact point can be located in both R_1 and R_2 sections of the roller profile, which is directly related to the cant angle. The cant angle for which the contact point locates in either R_1 or R_2 profiles are investigated.

For cant angles between $-6°$ and $-1.5°$, the center of the ellipse (contact patch shape) is located at R_2 region of the roller. As R_2 radius is smaller than R_1 radius, a smaller contact patch with higher contact pressure is expected. For cant angles between $-1.5°$ and $+6°$, the center of the ellipse is located at R_1 region leading to contact patch shapes with smaller axes aspect ratio compared to R_2 region. The contact point at two cant angles (0° and $-6°$) are shown in Figure 7.4.

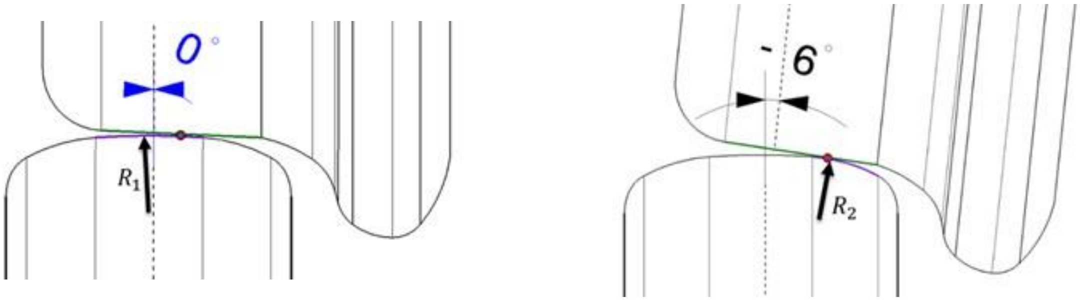

Figure 7.4 Contact Point at **0**° Cant Angle (Left), and $-$**6**° Cant Angle (Right)

For 0° and $-6°$ cant angles, the whole contact patches are located in R_1 and R_2 regions, respectively. The dimensions of the contact patches are illustrated in Figure 7.5. As the contact patch related to 0° cant angle is in the R_1 region, the contact patch area is bigger, and the resulting ellipse aspect ratio is smaller than the contact patch at $-6°$ cant angle, which leads to smaller contact pressures. Table 7.3 presents the contact area and contact patch aspect ratios for 0° and $-6°$ cant angles.

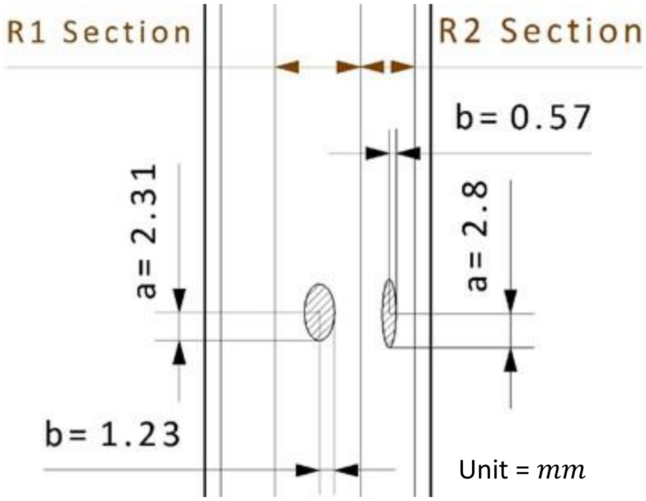

Figure 7.5 Contact Patch Dimensions at **0**° (Left) and $-$**6**° (Right) Cant Angles

Table 7.3 Contact Area and Aspect Ratio for **0**° and $-$**6**° Cant Angles

Cant Angle (°)	Contact Area (mm^2)	Contact Patch Aspect Ratio
0	8.93	1.88

-6	5.01	4.91

As discussed, the roller is comprised of several splines. For some contact points, the whole contact patch is located in the same region, either R_1 and R_2, e.g., $0°$ and $-6°$ cant angles. At some cant angles, the contact point is near the boundary between R_1 and R_2 regions, i.e., the contact patch lies in both regions. In this section, it is assumed that the contact patches near to the boundaries are formed based on both contact regions, i.e., any portion of contact patch geometry obeys the spline specification related to the region that contact patch shape lies. Figure 7.6 (left) illustrates the contact pressure versus cant angle and wheel load. For $10\ kN$ wheel load, the contact pressure is constant in approximately $0°$ to $5°$ cant angle interval, which means that the whole contact patch is in R_1 region. In addition, the contact pressure does not change for cant angles lower than $-4.5°$. For this range of cant angles, the contact patch is located in the R_2 region, i.e., it has the most significant contact pressure. For cant angles between $0°$ and $-4.5°$, the contact patch lies on both R_1 and R_2 regions. Therefore, the contact pressure is lower than contact pressure in R_2 region, and bigger than contact pressure in R_1 region.

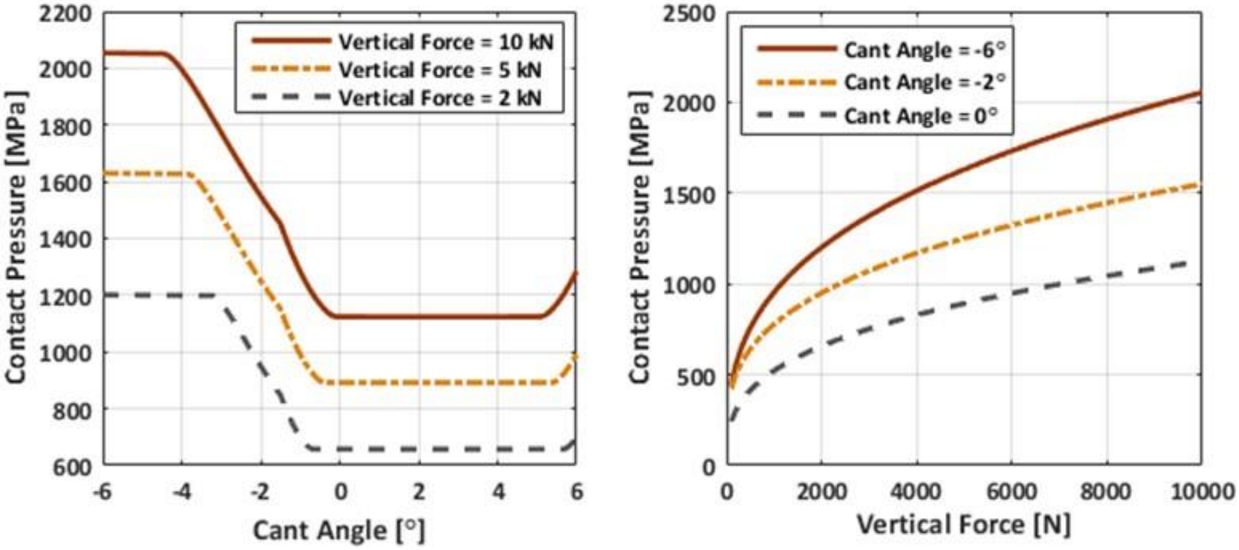

Figure 7.6 Contact Pressure vs. Cant Angle (Left) and Wheel load (Right)

The contact pressure relationship to wheel load is directly proportional to the contact area. Figure 7.6 (right) shows the contact pressure with respect to wheel load. At the small wheel loads, the slope of changing contact pressure is steeper than high wheel loads. It means that the contact area change rate is smaller for lower wheel loads resulting in higher contact pressures.

Figure 7.7 illustrates the 3D plot of contact pressure with respect to cant angle and wheel loads. For low wheel loads, the contact patch is smaller, i.e., the range in which the contact patch is located on both regions is smaller. As the wheel load increases, the difference between the minimum and maximum contact pressures, which occur in R_1 and R_2 regions, increases leading to the smaller cant angle range where contact pressure is constant.

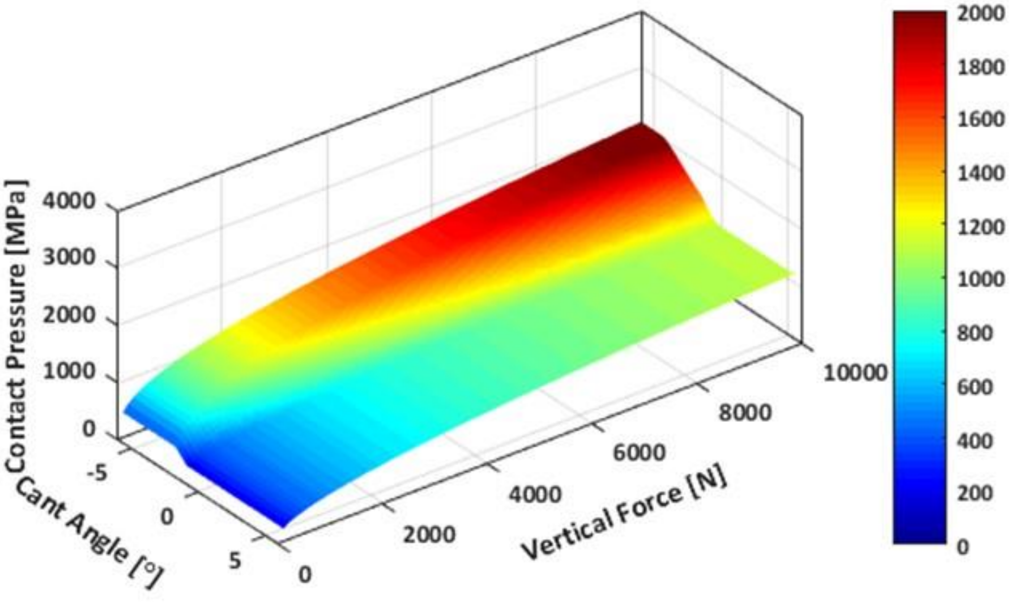

Figure 7.7 Contact Pressure vs. Cant Angle and Wheel load (3D Plot)

7.5. Contact Patch Geometry Measurement Using Pressure Sensitive Films

A practical way to measure the contact patch shape is to utilize pressure sensitive films. The films can be put in between the wheel and the roller, and the resulting contact geometry can be derived statically. The pressure sensitive films contain a layer of tiny microcapsules. The applied force on the film causes microcapsules to rupture, producing an instantaneous and permanent high-resolution topographical image of pressure variation across the contact area [59]. The color intensity of the pressure sensitive films indicates the amount of pressure applied to it. The higher the pressure, the more intense the color [59]. There are various films with different measurement ranges. Three types of pressure sensitive films provided in Table 7.4 are used to measure the contact patch geometry on the roller rig.

Table 7.4 Pressure Sensitive Film Types, Pressure Ranges, and Thickness [59], [60]

Film Type	Pressure Range	Thickness
Super Low	$70 - 350\ psi\ (0.5 - 2.4\ MPa)$	Two-Sheet: $90\ \mu m$ each
High	$7100 - 18500\ psi\ (49.0 - 127.6\ MPa)$	Mono-sheet: $110\ \mu m$
Super High	$18500 - 43200\ psi\ (127.6 - 297.9\ MPa)$	Mono-sheet: $110\ \mu m$

Super Low film, which consists of two sheets, is presented in Figure 7.8 (top). When the pressure is applied to the film, the microcapsules are broken, and the color-forming material transfers to the color-developing material and reacts, thereby generating a red color [60]. High and Super High films, which are shown in Figure 7.8 (bottom), are mono-sheet type. By applying the pressure, the microcapsules are broken, and the color-developing material absorbs the color-forming material and reacts, which generates a red color.

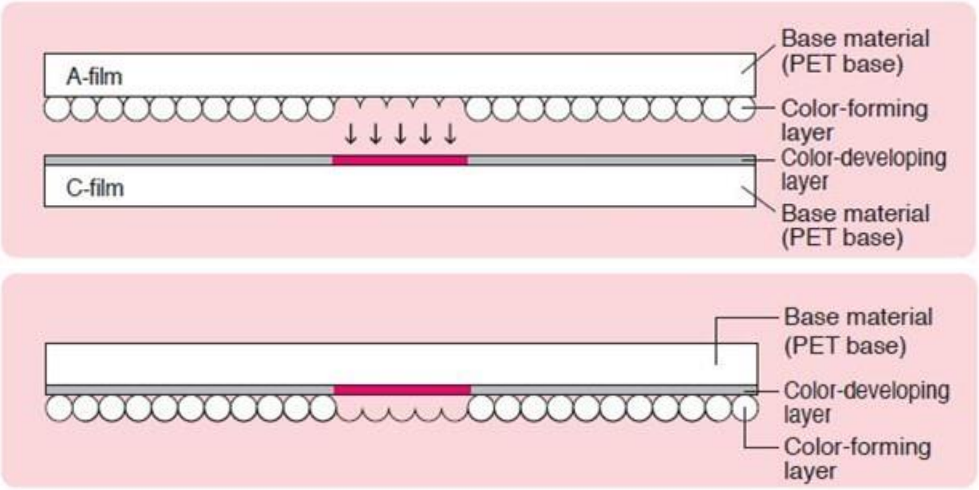

Figure 7.8 Super Low Sheet Type (Top) High and Super High Sheet Type (Bottom)

7.5.1. Repeatability of Pressure Sensitive Film Measurements

It is important to know how one measurement differs from another measurement under the same conditions. Repeatability of measurements provides metrics to know the tolerance and standard deviation of measurements. Fifty experiments were performed using Super-Low pressure sensitive film. For each experiment, the pressure sensitive film was taped on the wheel surface and the desired load was applied. It is worth to note that all measurements are taken in the static mode where the wheel and roller are stationary. As seen in

Figure 7.9, a specified section on the wheel and roller surfaces are considered for this study and all the tests were conducted at the same wheel and roller locations.

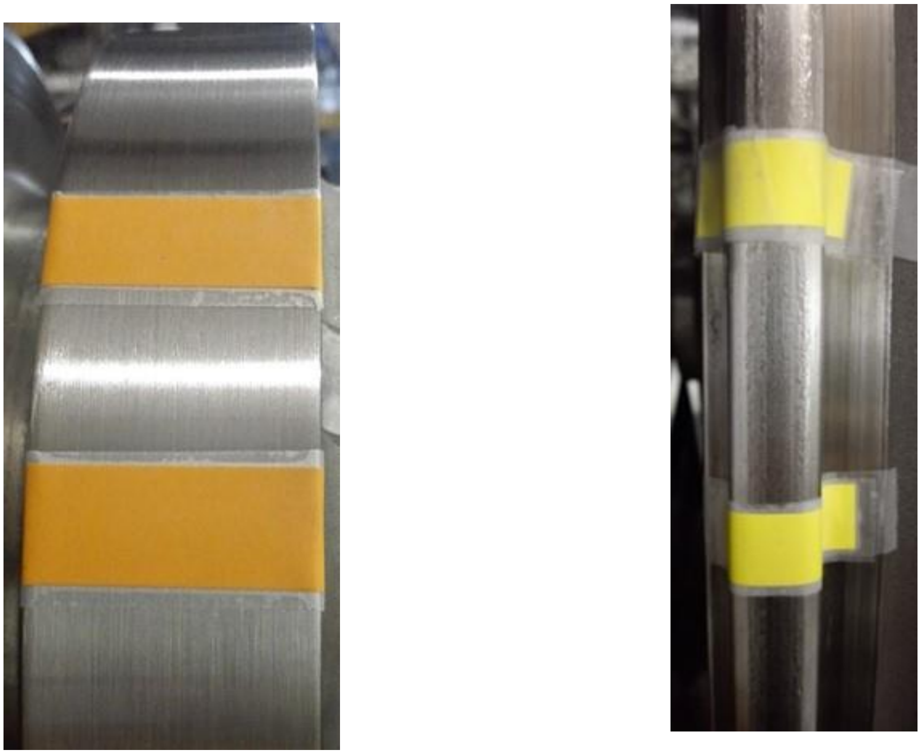

Figure 7.9 Measurement Section, Wheel (left), Roller (right)

The cylindrical wheel is used for this study and load of 10 kN was applied for each measurement. A summary of the test conditions is provided in Table 7.5.

Table 7.5 Test Conditions - Repeatability of Pressure Sensitive Films

TEST PARAMETER	VALUE
Wheel Profile	Cylindrical
Roller Profile	US-136 rail
Angle of Attack (°)	0
Cant Angle (°)	0
Rig Wheel load (kN)	10.0
Full-Scale Wheel Load (kN)	160.0
Measurement Type	Static
Film Type	Super-Low

Since both contact shape and contact area are important to evaluate, Figure 7.10 is provided to show each single measurement.

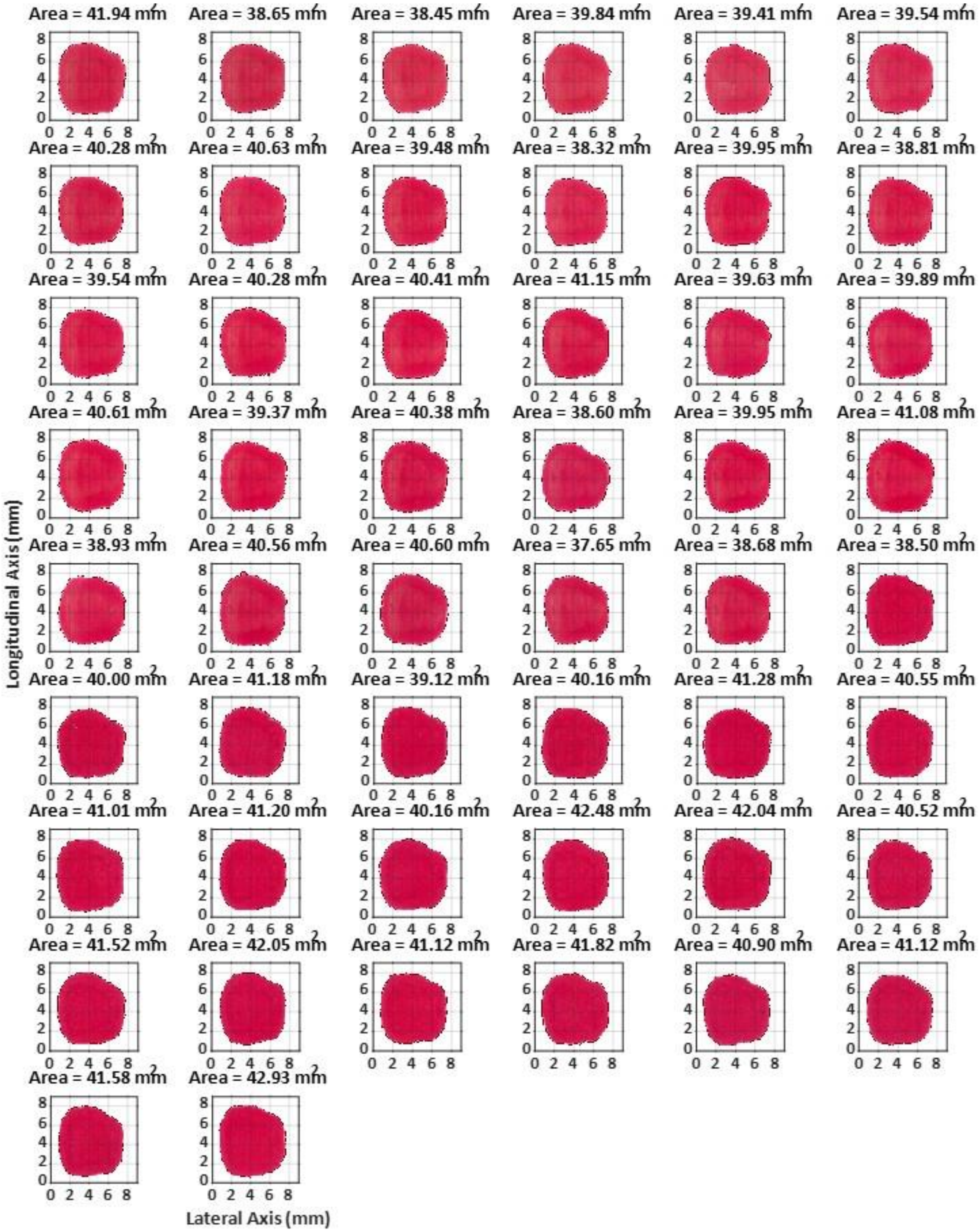

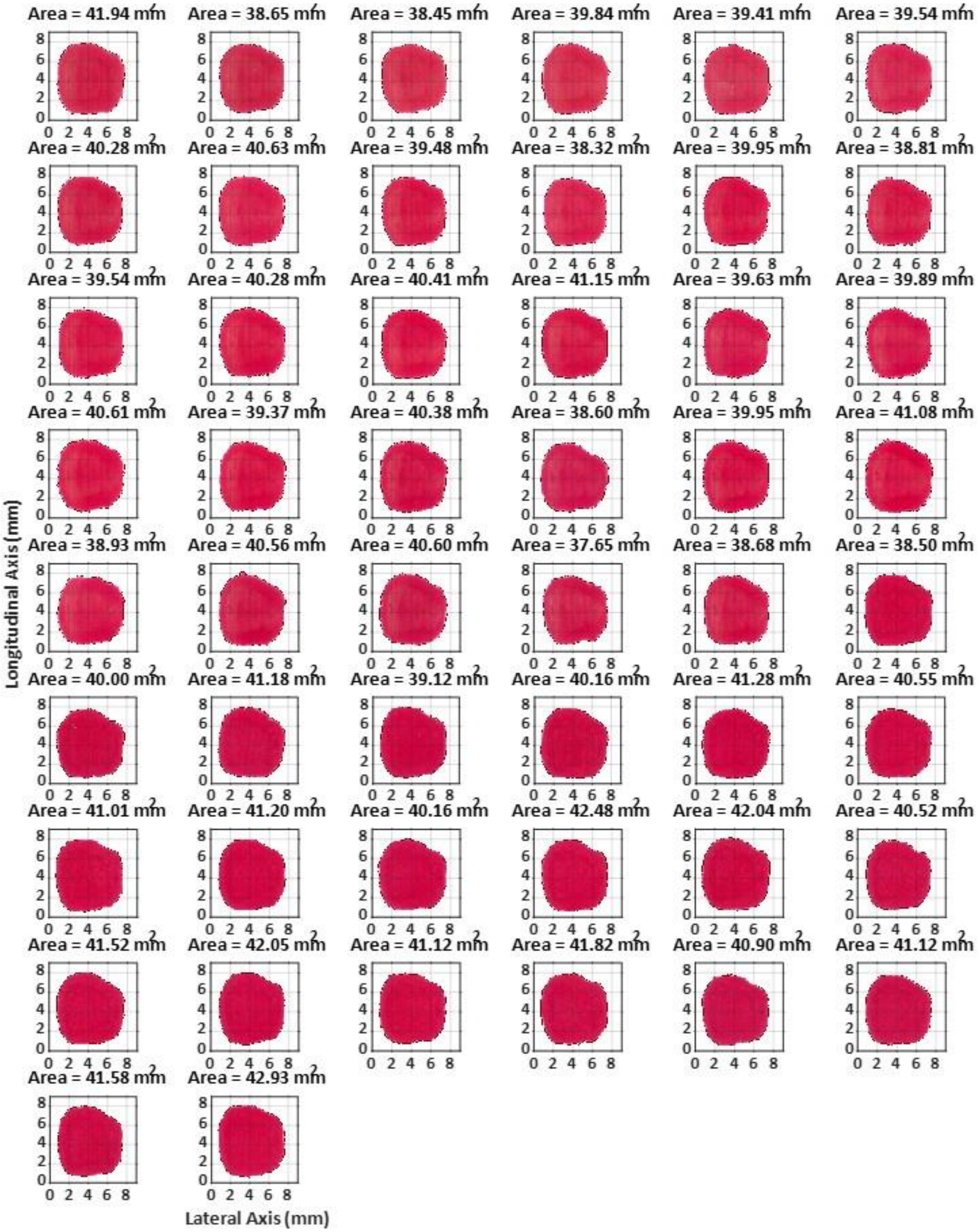

Figure 7.10 All Fifty Measurements – Repeatability of Pressure Sensitive Films

Based on Figure 7.11, it can be observed that the data distribution follows a normal distribution with a mean of 40.28 mm^2 and standard deviation of 1.18 mm^2.

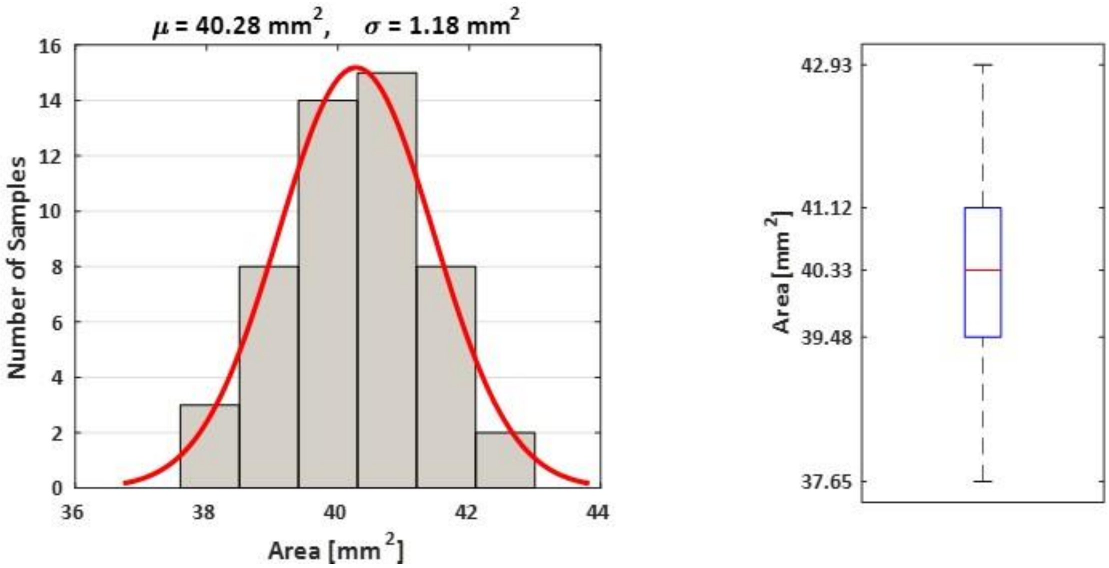

Figure 7.11 Fitted Gaussian Distribution (left), Box Plot of Measurements (right)

7.5.2. Contact Patch Results – Pressure Sensitive Film Measurements

The experiments are conducted at four different wheel loads, 2 kN, 4 kN, 7 kN, and 10 kN, on the cylindrical wheel. The wheel and the roller contact points are the same for all experiments to be able to compare the results with each other. The pressure sensitive films are placed in between the wheel and the roller one by one in the static mode without rotating the wheel and the roller. Then, the desired wheel load is applied accurately using the linear actuators. A summary of the test conditions is presented in Table 7.6.

Table 7.6 Contact Patch Study Test Conditions

TEST PARAMETER	VALUE
Wheel Profile	Cylindrical
Roller Profile	US-136 rail
Angle of Attack (°)	0
Cant Angle (°)	0
Rig Wheel load (kN)	2.0 to 10.0
Full-Scale Wheel Load (kN)	32.0 to 160.0
Measurement Mode	Static

A schematic of testing performed on the VT-FRA roller rig is presented in Figure 7.12 (a). Figure 7.12 parts (b) and (c) show the pressure sensitive films that are taped on the wheel surface before and after applying the pressure.

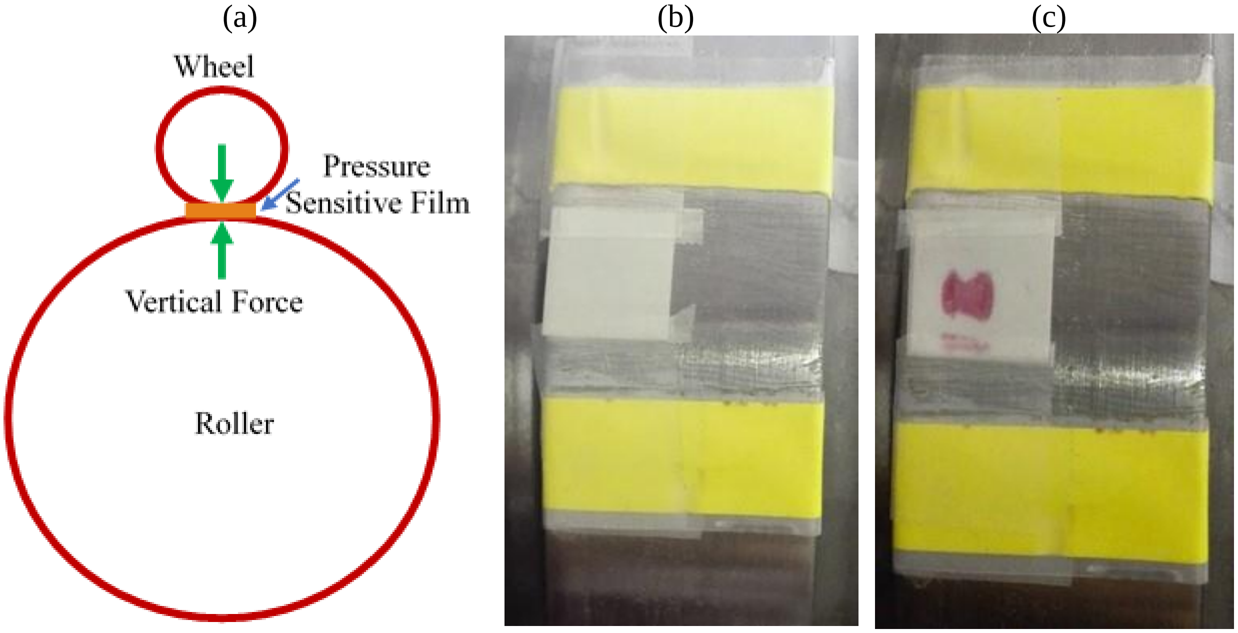

Figure 7.12 Schematic of Contact Patch Experiment

All the measurements obtained are presented in

Figure 7.13. Measurements in the same column are obtained by experimenting on the same film type. Each row in the figure provides information about the measurements in the same wheel load condition. The longitudinal axis shown in the figure is in the running direction of the wheel on the roller. On the other hand, the longitudinal axis demonstrates the direction on which the wheel and roller planes lie. Accordingly, the lateral axis shows the perpendicular axis to the longitudinal direction in the contact patch plane.

The area captured by Super High films is smaller than the other films since Super High films are indicating the pressures not lower than $127.6\,MPa$. The area, which is measured by Super Low sensitive film can be considered as an approximation for the total contact area as Super Low films can indicate pressures as low as $0.5\,MPa$. The wheel and roller surface conditions have substantial effects on the contact patch test results. Each contact area demonstrates two regions of high pressures. Under low wheel loads, these two regions are better recognizable. It may be due to the change in the wheel surface over time. The results indicate that the wheel surface profile may have been changed to a concave one over successive test runs conducted on the rig. Another reason that may address the contradictory results with Hertz's theory is the roller surface profile, which may have been affected by experiments performed on the rig over time. The small change in the contact area measurements between High and Super High films provides valuable information on the rate of changing pressure. It means that in a small area the pressure changes from $49.0\,MPa$ to $127.6\,MPa$ abruptly. The light and dark colors in the contact patch images show the pressure distribution over the area; however, the darkest area in each measurement is related to the pressures that exceed the maximum pressure range of each film type.

Looking at the measurement under $10\ kN$ wheel load shows that most of the region has exceeded the maximum pressure range of the film types. Therefore, it is needed to make some assumptions and provide an estimation of the region with higher contact pressures. Utilizing pressure sensitive films with higher pressure ranges would help more to estimate the maximum contact pressure and pressure distributions at contact accurately.

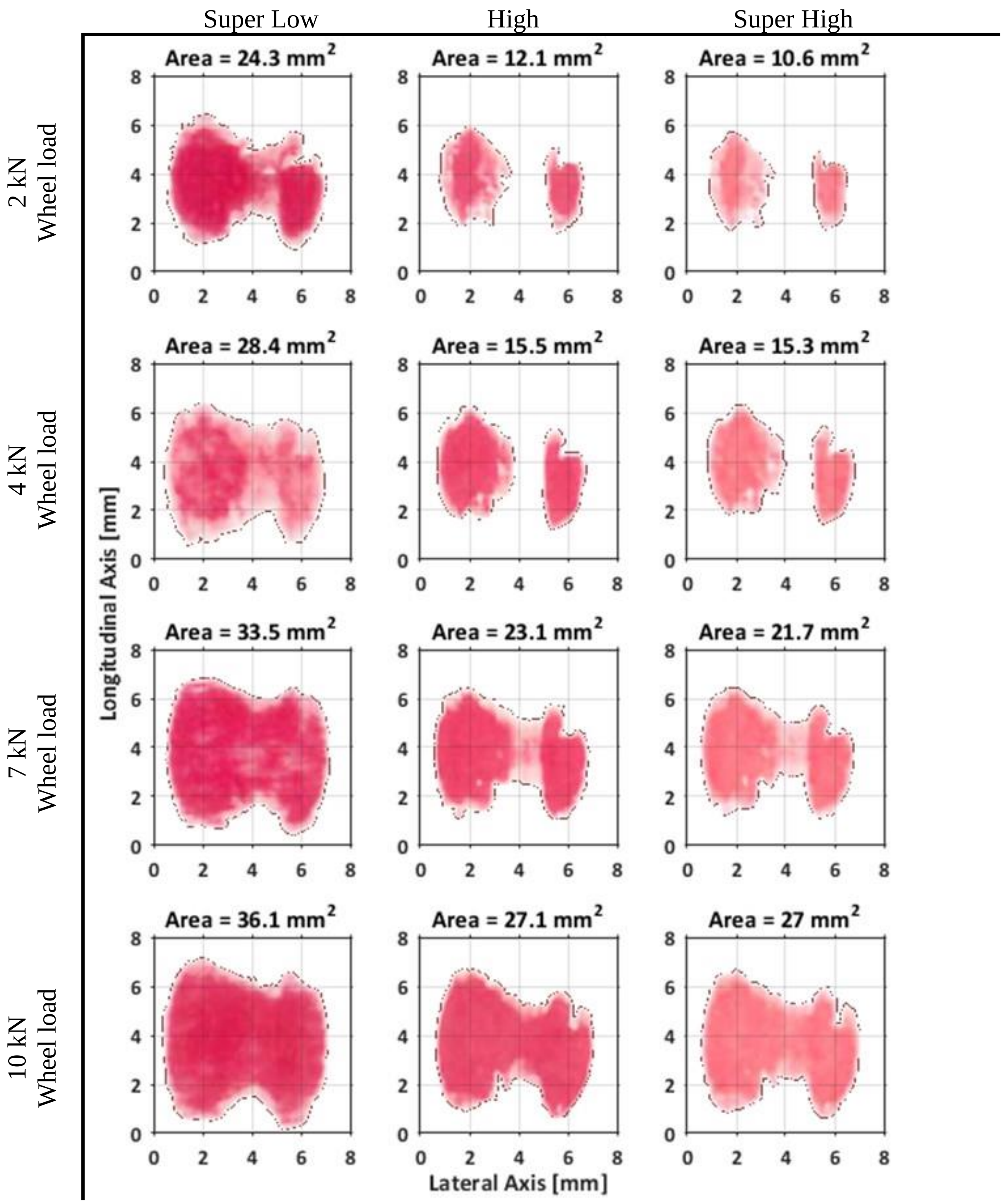

Figure 7.13 Contact Patch Measurements Using Pressure Sensitive Films

For each set of experiments under the same wheel load condition, the contact pressure distribution can be estimated by putting all the pressure sensitive films on top of each other and analyze the area in between each film type. Figure 7.14 shows the pressure sensitive films measurements, which are put on top of each other for each set of wheel load experiments. For low wheel load experiments, a considerable portion of the contact patch is under low pressures. As the wheel load goes up, the high-pressure regions, High and Super High measurements, take the most portion of the contact area. It means that increasing the force tends to increase the contact pressure more rather than increasing the contact area.

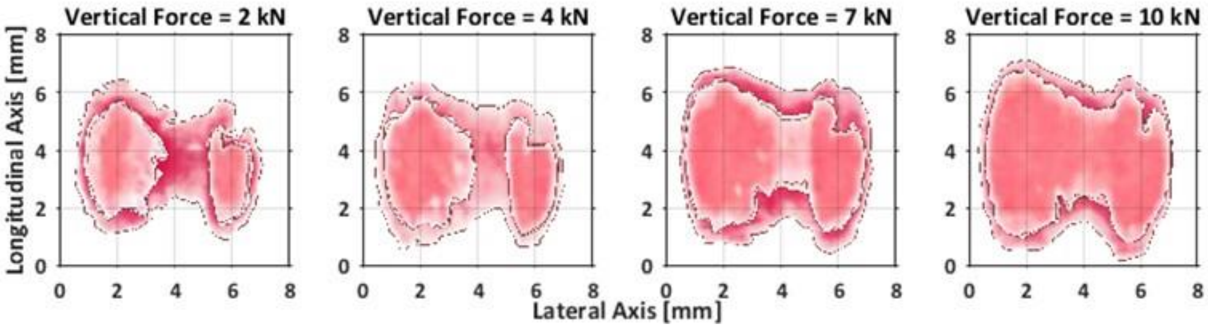

Figure 7.14 Putting Pressure Sensitive Film Measurements on top of Each Other

To better analyze the contact pressure, each film type measurement is colored differently. Figure 7.15 demonstrates the colored regions of the contact patch. The measurements obtained by Super Low film type is shown by the blue color, i.e., the blue areas are related to the pressure ranges between 0.5 to 49.0 MPa. The green area, which is captured by the High film type illustrates the regions with pressures in the range of 49.0 to 127.6 MPa. The Super High film measurements are shown by yellow and red colors. The red region is determined based on the original pressure distribution over the contact patch. In other words, the red regions are defined visually when the darkest possible color for the Super High sensitive film is observed, i.e., it is assumed that the pressure is exceeded the Super High pressure range in the specified red areas. Therefore, the yellow regions are estimated to show the pressure ranges in 127.6 to 297.9 MPa interval, and the red regions are assumed to be the area with the pressure higher than 297.9 MPa.

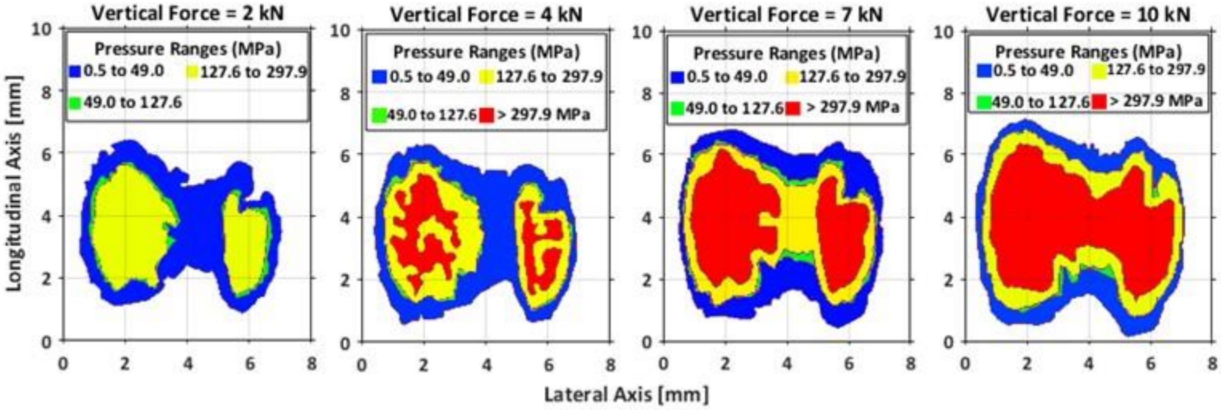

Figure 7.15 Contact Pressure Distribution over the Contact Patch

Based on the pressure analyses performed in Figure 7.15, it is possible to calculate the area related to each color, i.e., the areas with different pressure ranges. The maximum pressure of the contact patch is estimated by assuming linear pressure distribution over each region. Figure 7.16 shows the pressure sensitive films areas, average pressure, and estimated maximum pressure under each wheel load condition. The curves have a linear behavior; however, the maximum pressure seems to have a steeper rate of increase relative to the average pressure.

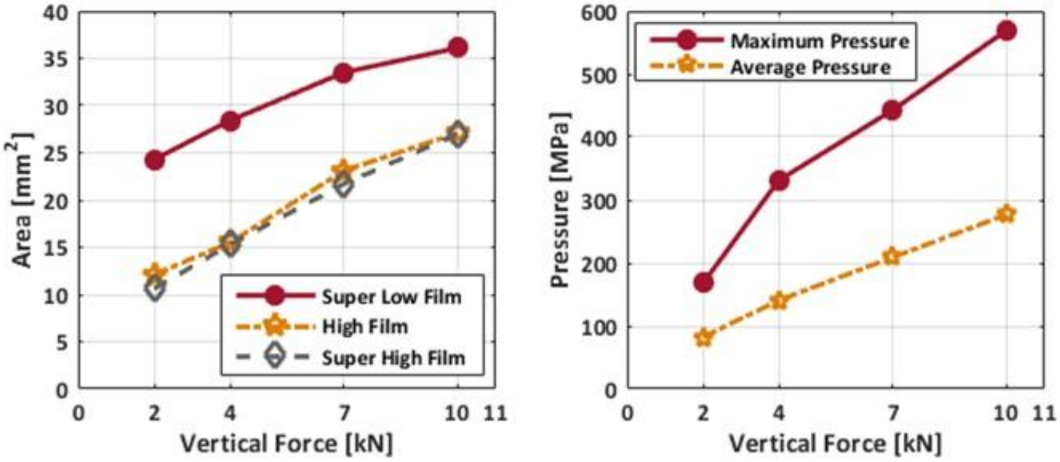

Figure 7.16 Contact Area, Wheel load, and Contact Pressure Relationships

Based on the results observed in Figure 7.15, the area in which a range of pressures applied can be calculated. Figure 7.17 shows the area portions related to each pressure range for all wheel load experiments. The color of each curve is the same as the color of regions in Figure 7.15. Comparing blue and red curves, which are corresponding to low- and high-pressure regions indicate that increasing wheel load tends to increase the portion of high-pressure areas rather than increasing the total contact patch area.

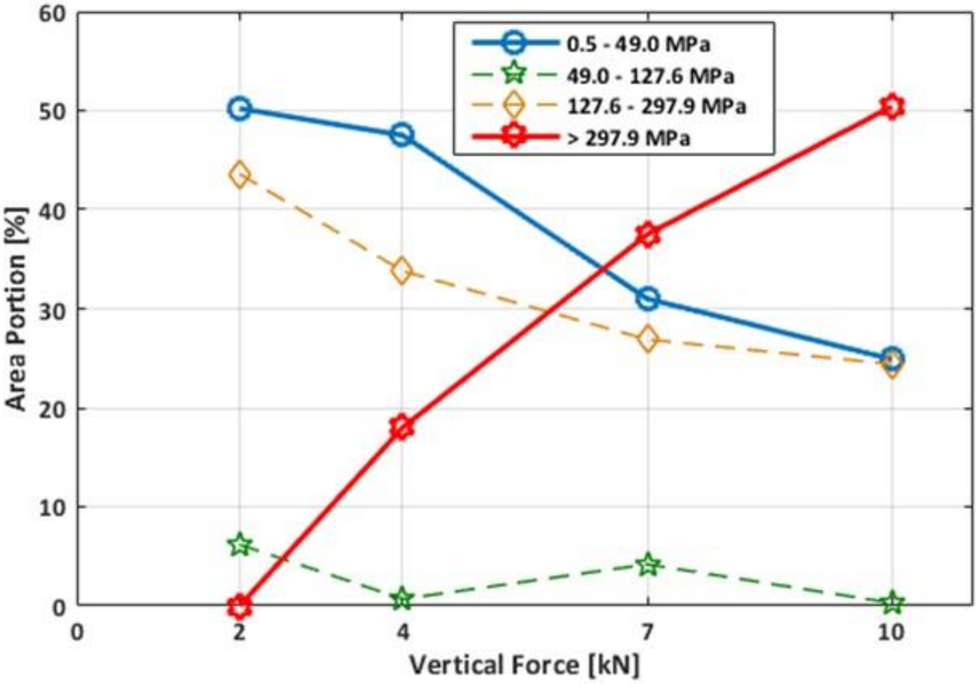

Figure 7.17 Area Portions Calculated for Each Pressure Range

7.6. Simulation of Contact Patch

In this section, a simulation of contact patch shape, contact area, and pressure distribution is provided. The models are separated into two sections, in the presence of pressure sensitive film, and pure wheel-roller contact.

7.6.1. Pure Wheel-Roller Contact

Considering contact between two cylinders, as shown in Figure 7.18 , the force is linearly proportional to the penetration depth according to the following equation [61].

$$d \approx \frac{4}{\pi}\frac{F}{E^{*}L}, \quad \frac{1}{E^{*}} = \frac{1-{\nu_1}^{2}}{E_1} + \frac{1-{\nu_2}^{2}}{E_2} \tag{7-12}$$

where d is the penetration depth, F is the applied load, E is the module of elasticity, ν is the Poisson ratio, and L is the length of contact.

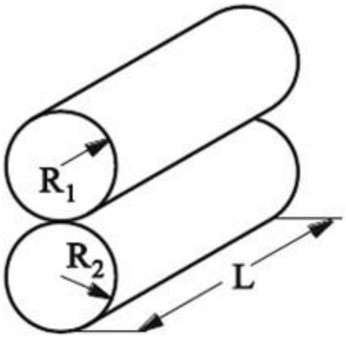

Figure 7.18 Contact between Two Cylinders with Parallel Axes [61]

Based on the calculated penetration depth, the half of the contact width (a) is given through the following equation [61]

$$a \approx \sqrt{Rd}, \quad \frac{1}{R} = \frac{1}{R_1} + \frac{1}{R_2} \tag{7-13}$$

In this model, it is assumed that the wheel and roller are formed by slices of cylinders with the length of the laser scanner resolution in x-direction. A typical shape of this method and slices of cylinders are shown in Figure 7.19. This assumption allows us to use the actual wheel and roller surface profiles for simulations. The wheel and roller surface profiles used for this study are provided in Figure 7.20. These profiles are measured by the laser scanner, which was introduced in the previous section.

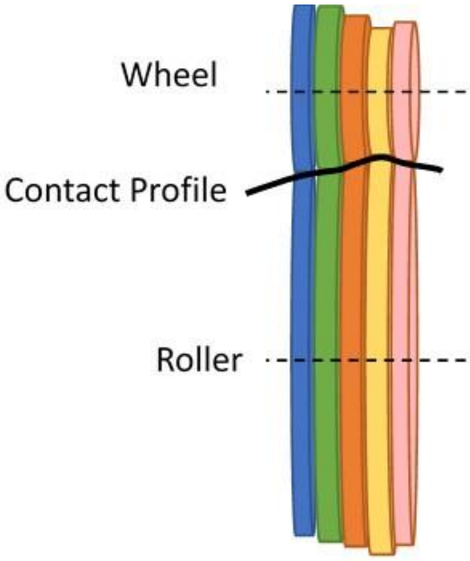

Figure 7.19 Slices of Cylinders Method

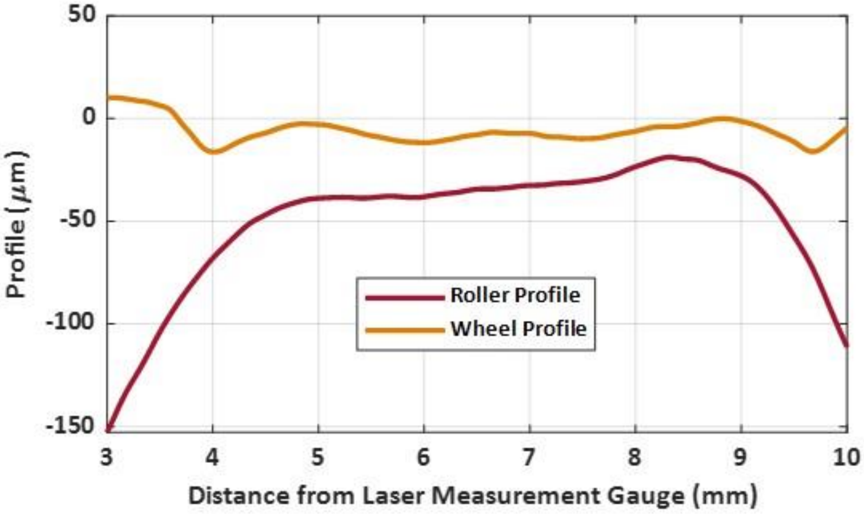

Figure 7.20 Wheel and Roller Surface Profiles Used for Contact Patch Simulation

An algorithm was employed to estimate the penetration depth and length of contact. The algorithm is based on the area of penetration. Considering penetration depth equation, it can be concluded that the product of penetration depth and length of contact results in a constant value considering the same load. Therefore, the penetration area was selected as a metric to simulate the penetration depth and length of contact. A summary of the algorithm is presented in Figure 7.21. Based on this algorithm, the wheel profile gets closer to the roller profile at each step, and the penetration area is calculated. If the penetration area is close enough to the estimated penetration depth and length of contact, the algorithm would be terminated, and the resulting penetration depth and length of contact would be provided. Figure 7.22 demonstrates the wheel-roller profile penetrations under 10 kN Load. The parameters used for this study is provided in
Table 7.7.

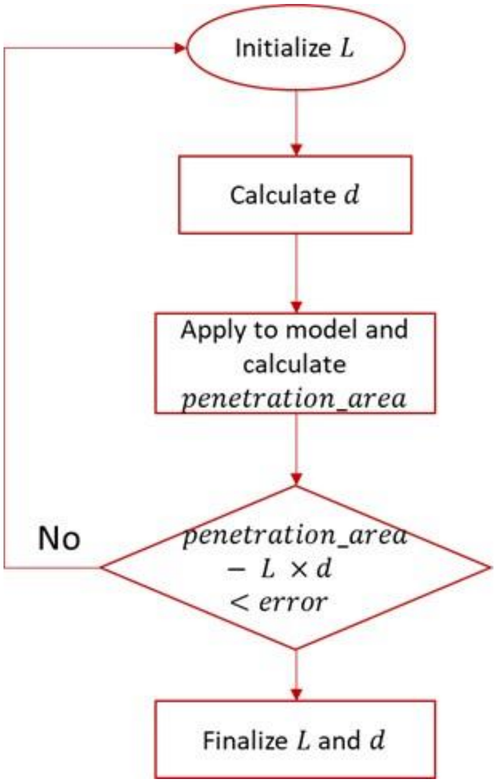

Figure 7.21 Penetration Depth-Length of Contact Algorithm

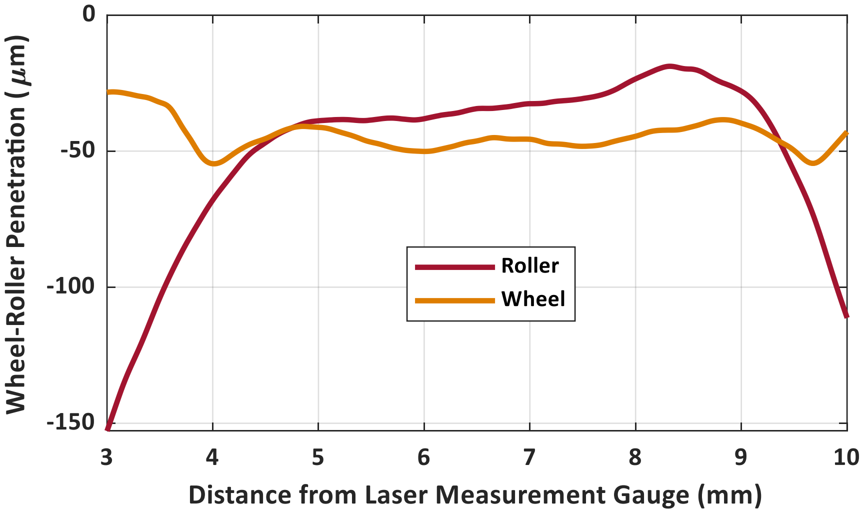

Figure 7.22 Wheel-Roller Penetration under 10 kN Load

Table 7.7 Simulation Parameters – Pure Wheel-Roller Contact

PARAMETER	VALUE
Wheel-Roller Module of Elasticity	200 GPa

Load	10 kN
Poisson Ratio	0.28

Figure 7.23 provides four simulations performed using the algorithm for slices of cylinders. At small loads, the contact patch is smaller with smaller pressure distributions. The simulated contact areas are far smaller than the measured ones with the pressure sensitive films, which implies that pressure sensitive films or any third body layer at contact affects the contact area and pressure distributions significantly. In the next section, the contact patch area and pressure distribution are simulated in the presence of pressure sensitive films with the same wheel and roller profiles.

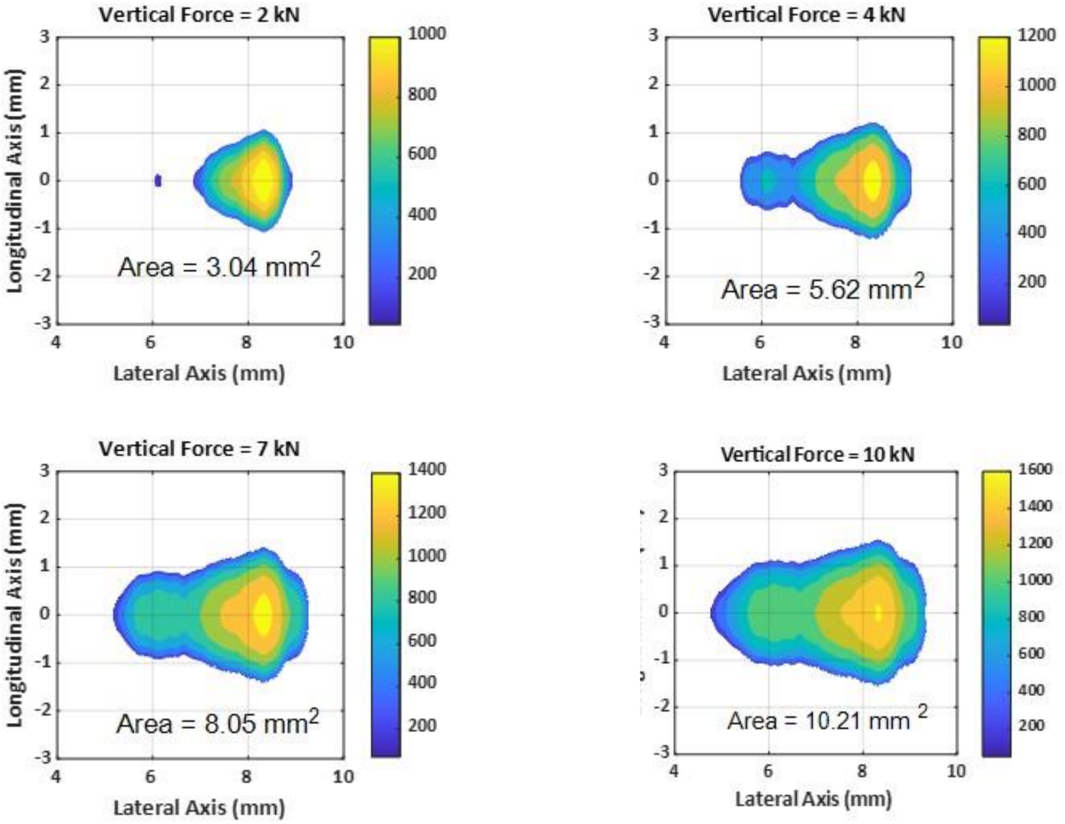

Figure 7.23 Simulated Wheel-Roller Contact Patch - Pure Contact

7.6.2. Contact Patch Simulation in the Presence of Third Body Layer

In this section, the contact patch is simulated using the method of contacting a rigid cylinder with an elastic layer [62], [63]. A schematic of the cylinder-elastic layer contact is provided in Figure 7.24. Based on the stress-strain analysis, the surface displacement at $x_3 = 0$ in vertical direction is

$$u_3 = L_3 p_3, \quad L_3 = b\frac{(1+\nu)(1-2\nu)}{(1-\nu)E} \tag{7-14}$$

where u_3 is the displacement in the vertical direction, p_3 is the corresponding pressure, b is the film thickness, ν is the film Poisson ration, and E is the film module of elasticity.

To solve the contact problem numerically, displacement at each node is calculated and the node force is estimated by

$$F_3 = \frac{u_3}{L_3} A \tag{7-15}$$

where F_3 is the node force, and A is the node area.

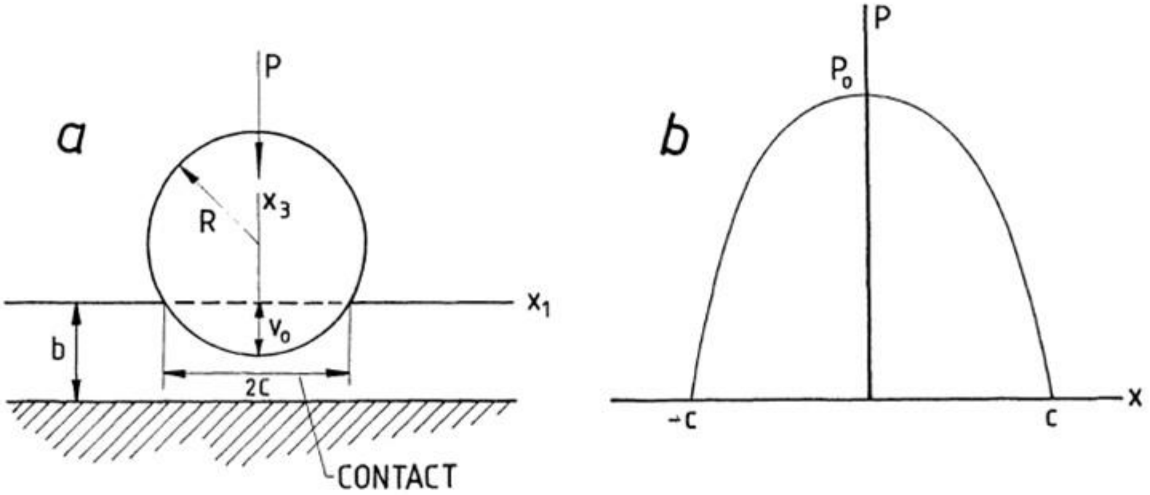

Figure 7.24 Rigid Cylinder-Elastic Layer Contact [62]

Wheel-roller surface segmentation and force calculation was performed based on the laser scanner resolution in the x-direction. Figure 7.25 shows a sample of wheel-roller segmentation. In this method, the wheel and roller surface are pressed on the pressure sensitive film until the desired force is reached. The total force is calculated based on the sum of node forces. If the total force is equal to the desired load, the algorithm would be terminated. It is obvious that the force is applied in nodes where the distance between two corresponding nodes on the wheel and roller surfaces is less than the pressure sensitive film thickness. The applied displacement on the film will cause a force at each node.

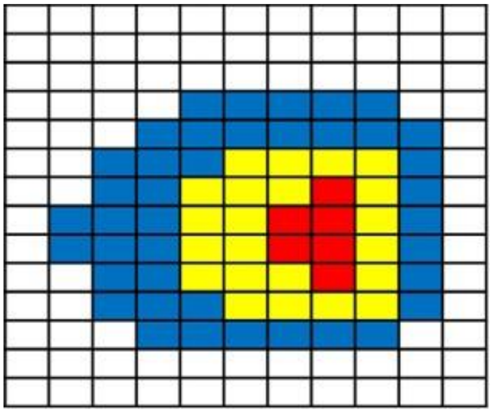

Figure 7.25 Sample of Wheel-Roller Segmentation

For the Super Low pressure sensitive film, the module of elasticity and Poisson ratio can be estimated by comparing the simulation results with the measurements.

Figure 7.26 provides a contact measurement using the Super-Low pressure sensitive film (left), and the simulated contact patch and area based on the module of elasticity of 800 MPa and Poisson ratio of 0.33 for the film.

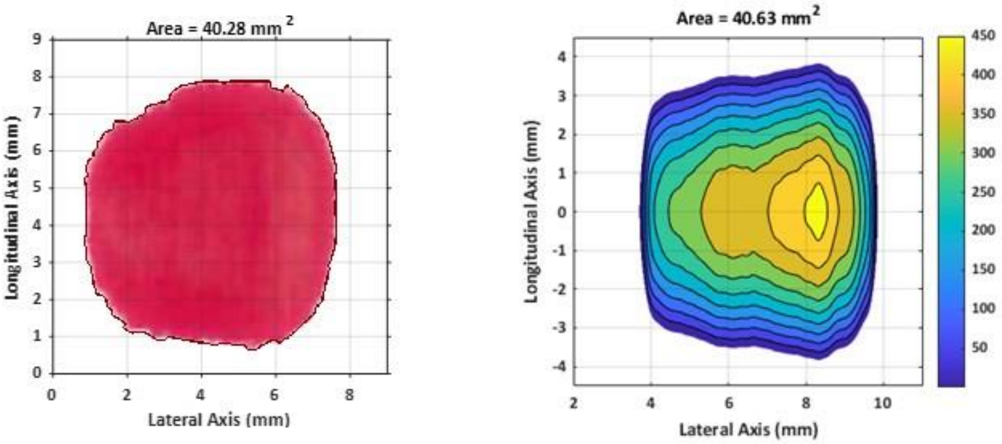

Figure 7.26 Contact Shape Measurement (left), Contact Shape Simulation (right)

The simulated results show a good match between contact measurement and simulated one for both contact shape and contact area. Therefore, the model can be used further to estimate the contact patch shape and pressure distribution specially in the presence of third body layers.

7.7. Summary

In this chapter, contact patch geometry is calculated based on the roller rig's wheel and roller profiles. Hertz's theory is used to estimate the elliptical shape of contact patch under a range of wheel loads. The scaled-down profiles of AAR-1B wheel and US-136 roller have been considered. It is assumed that all the contact points are located in the taper portion of the wheel. Based on the splines form the roller profile and the range of cant angle on the rig, it is shown that the contact can occur on two profiles with different radii. The contact area is calculated based on contacting in both regions of the roller. Hertz's theory is extended for contacts where the contact shape is placed on both roller profiles. If the contact occurs on the region with bigger radius on the roller, the contact area would be bigger, the ellipse aspect ratio and the contact pressures would be smaller.

In the second phase of the chapter, pressure sensitive films are utilized to evaluate the contact patch geometry and pressure distribution at contact. Three types of pressure sensitive films with low to high ranges of pressure are considered for this study. In addition, the contact area and contact pressure are estimated with respect to the sets of wheel load experiments on the rig. The experiments are performed on a static mode, i.e., the wheel and roller are fixed in the desired position without rotational movement. All experiments are conducted at the same contact point on the wheel and roller surfaces to be able to compare the results of experiments. The results indicate that increasing the wheel load influence the regions with high pressures more than increasing the total contact patch area.

8. Summary and Recommendations

8.1. Summary

The VT-FRA roller rig has provided an unprecedented opportunity to explore the wheel-rail contact mechanics and dynamics with a high degree of precision in conditions that resemble field environment. Of course, with far more control on the test parameters and far greater precision. The rig is composed of five state-of-the-art electromagnetic actuators that allow precise positioning and angling of wheel and roller together to emulate AOA, cant angle, lateral wheel-rail position, and wheel load to unparallel degree of accuracy. It also includes two independently controlled motors that allow setting the relative speed of the wheel and roller to within 0.1 RPM, hence enabling setting the %creepage with precision. Finally, the rig includes a high-precision load measurement unit that allows measuring wheel load and moments at the contact.

The high frequency dynamics that occurs as a result of a compliance-like phenomenon in the direction of motion at the contact is formulated, and the corresponding high frequency is calculated based on the rig's wheel and roller geometry, material specifications, and the range of wheel loads (vertical loads) that can be accommodated with the rig.

The creep forces and traction coefficients are analyzed under various conditions considering wheel load, creepage, and angle of attack as parameters. Applying more wheel load leads to having more wear on the wheel surface, i.e., when plotted versus time, creep forces go up at a steep rate initially, which is referred to as the "transient" range or period. The %creepage strongly influences traction. As expected, increasing %creepage leads to higher traction coefficients until saturation is reached. The maximum traction coefficient is established for various. %creepage, which proves to be independent of the amount of the natural third body layer generated as the result of wear.

To analyze the effect of angle of attack, two sets of tests are carried out. First, the running surface is redressed (completely cleaned and smoothed) and the angle of attack is adjusted before the start of the test, and the effect of natural third body layer generation on creep forces and traction coefficients is investigated. For the second set of tests, the running surfaces are not redressed (include worn material and a slight devout at the running surface) and the angle of attack is changed from -1 to +1 degree during the experiment in a slow sweep. The test results with a 1:20 tapered wheel clearly indicate that lateral forces even when there is no angle of attack, much like a DC offset. The DC offset is directly related to the taper of the wheel. The large the wheel taper is, the larger the DC offset would be. The zero lateral force occurs at an angle of attack other than zero. Additionally, the DC offset causes asymmetric lateral forces for positive and negative AOA. This means that a tapered wheel negotiates a right-hand curve differently from a left-hand curve.

The wheel surface conditions have a strong influence on creep forces. Therefore, it is needed to evaluate the wheel surface metrology, especially before and after each test. The rig is equipped with a laser scanner camera that provides a three-dimensional surface measurement of the wheel with micron precision. Using the laser scanner, the study provides a precise account of the change in traction forces with increasing wheel wear and worn material accumulation at the running surface. The results indicate that there is a rapid rise in traction upon the accumulation of worn material, and it reaches a plateau after the running surface is saturated with worn material. The Worn material acts as a “natural” third body layer that increases traction until its maximum level is reached for the test condition. This acts opposite of most added third body layers that reduce traction. The study also measures wheel wear with time for various running conditions. As expected, the most influential factors prove to be wheel load and %creepage. Their influence, however, is measured to be nonlinear. Large wheel loads and %creepage result in significantly larger wheel wear. Although not directly measured, we anticipate that the increased wheel wear would also result in increased rail wear.

Finally, the contact patch geometry is modeled based on the rig’s wheel and roller profiles, material properties, and the range of wheel loads applying at contact. Using Hertzian contact, the contact patch area and the contact ellipse aspect ratio is estimated. Based on the wheel and roller geometry, it is assumed that the contact point is located on the taper portion of the wheel. For the roller, the contact can occur at two profiles with different radii, leading to different contact patch shapes. Pressure sensitive films are used to measure the contact patch geometry and pressure distribution on the roller rig statically. The relationship between wheel load, contact area, and contact pressure are evaluated. It is shown that increasing the wheel load increases contact pressure far more than increasing the contact area. It is estimated that the wheel and rail material properties play a significant role in the latter.

8.2. Recommendations for Future Study

This study’s results have set the foundation for many future studies that can use the unique parameter control and measurement precision of the VT-FRA roller rig to further advance the result or venture out in other scientific directions that can benefit the safety and operational efficiency of the railroads. Some of such studies can be summarized as follows:

- Evaluate the effect of rail cant angle on contact dynamics
- Analyze the effect of ToR friction modifier on creep forces and wheel wear,
- Investigate the parameters affecting the squeal noise,
- Evaluate the effect of wheel surface roughness and hardness on forces at the wheel-rail interface (WRI).

References

[1] K. S. Baek, K. Kyogoku, and T. Nakahara, "An Experimental Investigation of Transient Traction Characteristics in Rolling-Sliding Wheel/Rail Contacts under Dry-Wet Conditions," *Wear*, vol. 263, no. 1-6 SPEC. ISS., pp. 169–179, 2007, doi: 10.1016/j.wear.2007.01.067.

[2] K. S. Baek, K. Kyogoku, and T. Nakahara, "An Experimental Study of Transient Traction Characteristics between Rail and Wheel under Low Slip and Low Speed Conditions," *Wear,* vol. 265, no. 9–10, pp. 1417–1424, 2008, doi: 10.1016/j.wear.2008.02.044.

[3] Y. Berthier, S. Descartes, M. Busquet, E. Niccolini, C. Desrayaud, and L. Baillet, "The Role and Effects of the Third Body in the Wheel-Rail Interaction," *Fatigue Fract. Eng. Mater. Struct.*, vol. 27, no. 5, pp. 423–436, 2004, doi: 10.1109/MPER.1985.5528789.

[4] S. Descartes, C. Desrayaud, E. Niccolini, and Y. Berthier, "Presence and Role of the Third Body in a Wheel-Rail Contact," *Wear*, vol. 258, no. 7–8, pp. 1081–1090, 2005, doi: 10.1016/j.wear.2004.03.068.

[5] S. Descartes, C. Desrayaud, and Y. Berthier, "Experimental Identification and Characterization of the Effects of Contaminants in the Wheel-Rail Contact," *Proc. Inst. Mech. Eng. Part F J. Rail Rapid Transit*, vol. 222, no. 2, pp. 207–216, 2008, doi: 10.1243/09544097JRRT191.

[6] S. R. Lewis, R. Lewis, and U. Olofsson, "An Alternative Method for the Assessment of Railhead Traction," *Wear*, vol. 271, no. 1–2, pp. 62–70, 2011, doi: 10.1016/j.wear.2010.10.035.

[7] M. Spiryagin, O. Polach, and C. Cole, "Creep Force Modelling for Rail Traction Vehicles Based on the Fastsim Algorithm," *Veh. Syst. Dyn.*, vol. 51, no. 11, pp. 1765–1783, 2013, doi: 10.1080/00423114.2013.826370.

[8] O. Polach, "Creep Forces in Simulations of Traction Vehicles Running on Adhession Limit," *Wear*, vol. 258, pp. 992–1000, 2005.

[9] Y. Zhu, U. Olofsson, and K. Persson, "Investigation of Factors Influencing Wheel-Rail Adhesion Using a Mini-Traction Machine," *Wear*, vol. 292–293, pp. 218–231, 2012, doi: 10.1016/j.wear.2012.05.006.

[10] Y. Zhu, U. Olofsson, and H. Chen, "Friction Between Wheel and Rail: A Pin-on-Disc Study of Environmental Conditions and Iron Oxides," *Tribol. Lett.*, vol. 52, no. 2, pp. 327–339, 2013, doi: 10.1007/s11249-013-0220-0.

[11] T. Nakahara, K. S. Baek, H. Chen, and M. Ishida, "Relationship between Surface Oxide Layer and Transient Traction Characteristics for Two Steel Rollers under Unlubricated and Water Lubricated Conditions," *Wear*, vol. 271, no. 1–2, pp. 25–31, 2011, doi: 10.1016/j.wear.2010.10.030.

[12] K. Hou, J. Kalousek, and E. Magel, "Rheological Model of Solid Layer in Rolling Contact," *Wear*, vol. 211, no. 1, pp. 134–140, 1997, doi: 10.1016/S0043-1648(97)00097-5.

[13] O. Arias-Cuevas, Z. Li, R. Lewis, and E. A. Gallardo-Hernandez, "Rolling-Sliding Laboratory Tests of Friction Modifiers in Dry and Wet Wheel-Rail Contacts," *Wear*, vol. 268, no. 3–4, pp. 543–551, 2010, doi: 10.1016/j.wear.2009.09.015.

[14] C. Hardwick, S. Lewis, and R. Lewis, "The Effect of Friction Modifiers on Wheel/Rail Isolation at Low Axle Loads," *Proc. Inst. Mech. Eng. Part F J. Rail Rapid Transit*, vol. 228, no. 7, pp. 768–783, 2014, doi: 10.1177/0954409713488102.

[15] Y. Zhu, "The Influence of Iron Oxides on Wheel–Rail Contact: A Literature Review," *Proc. Inst. Mech. Eng. Part F J. Rail Rapid Transit*, vol. 232, no. 3, pp. 734–743, 2018, doi: 10.1177/0954409716689187.

[16] A. Meierhofer, C. Hardwick, R. Lewis, K. Six, and P. Dietmaier, "Third Body Layer-Experimental Results and a Model Describing Its Influence on the Traction Coefficient," *Wear*, vol. 314, no. 1–2, pp. 148–154, 2014, doi: 10.1016/j.wear.2013.11.040.

[17] H. Ronasi, K. D. Oldknow, J. Vander Marel, J. Cotter, and D. T. Eadie, "Traction-Creepage Curve Identification at the Wheel/Rail Interface: A Fast Experimental Approach," *Wear*, vol. 366–367, pp. 346–351, 2016, doi: 10.1016/j.wear.2016.06.017.

[18] P. Voltr and M. Lata, "Transient Wheel-Rail Adhesion Characteristics under the Cleaning Effect of Sliding," *Veh. Syst. Dyn.*, vol. 53, no. 5, pp. 605–618, 2015, doi: 10.1080/00423114.2014.961488.

[19] R. Lewis, R. S. Dwyer-Joyce, S. R. Lewis, C. Hardwick, and E. A. Gallardo-Hernandez, "Tribology of the Wheel-Rail Contact: The Effect of Third Body Materials," *Int. J. Railw. Technol.*, vol. 1, no. 1, pp. 167–194, 2012, doi: 10.4203/ijrt.1.1.8.

[20] W. Zhang, J. Chen, X. Wu, and X. Jin, "Wheel/Rail Adhesion and Analysis by Using Full Scale Roller Rig," *Wear*, vol. 253, no. 1–2, pp. 82–88, 2002, doi: 10.1016/S0043-1648(02)00086-8.

[21] O. Arias-Cuevas, Z. Li, and R. Lewis, "A Laboratory Investigation on the Influence of the Particle Size and Slip during Sanding on the Adhesion and Wear in the Wheel-Rail Contact," *Wear*, vol. 271, no. 1–2, pp. 14–24, 2011, doi: 10.1016/j.wear.2010.10.050.

[22] G. Trummer, L. E. Buckley-Johnstone, P. Voltr, A. Meierhofer, R. Lewis, and K. Six, "Wheel-Rail Creep Force Model for Predicting Water Induced Low Adhesion Phenomena," *Tribol. Int.*, vol. 109, no. December 2016, pp. 409–415, 2017, doi: 10.1016/j.triboint.2016.12.056.

[23] Y. Xi, M. Björling, Y. Shi, J. Mao, and R. Larsson, "Traction Formula for Rolling-Sliding Contacts in Consideration of Roughness under Low Slide to Roll Ratios," *Tribol. Int.*, vol. 104, pp. 263–271, 2016, doi: 10.1016/j.triboint.2016.09.006.

[24] X. Cao *et al.*, "The Effect of Alumina Particle on Improving Adhesion and Wear Damage of Wheel/Rail under Wet Conditions," *Wear*, vol. 348–349, pp. 98–115, 2016, doi: 10.1016/j.wear.2015.12.004.

[25] R. Galas, D. Kvarda, M. Omasta, I. Krupka, and M. Hartl, "The Role of Constituents Contained in Water–Based Friction Modifiers for Top–of–Rail Application," *Tribol. Int.*, vol. 117, no. April 2017, pp. 87–97, 2018, doi: 10.1016/j.triboint.2017.08.019.

[26] L. E. Buckley-Johnstone *et al.*, "Assessing the impact of small amounts of water and iron oxides on adhesion in the wheel/rail interface using High Pressure Torsion testing," *Tribol. Int.*, vol. 135, no. January, pp. 55–64, 2019, doi: 10.1016/j.triboint.2019.02.024.

[27] I. Goryacheva and A. Miftakhova, "Modelling of the viscoelastic layer effect in rolling contact," *Wear*, vol. 430–431, no. January, pp. 256–262, 2019, doi: 10.1016/j.wear.2019.05.021.

[28] M. B. Marshall, R. Lewis, R. S. Dwyer-Joyce, U. Olofsson, and S. Björklund, "Experimental Characterization of Wheel-Rail Contact Patch Evolution," *J. Tribol.*, vol. 128, no. 3, pp. 493–504, 2006, doi: 10.1115/1.2197523.

[29] M. Pau, F. Aymerich, and F. Ginesu, "Distribution of Contact Pressure in Wheel-Rail Contact Area," *Wear*, vol. 253, no. 1–2, pp. 265–274, 2002, doi: 10.1016/S0043-1648(02)00112-6.

[30] A. Rovira, A. Roda, M. B. Marshall, H. Brunskill, and R. Lewis, “Experimental and Numerical Modelling of Wheel-Rail Contact and Wear,” *Wear*, vol. 271, no. 5–6, pp. 911–924, 2011, doi: 10.1016/j.wear.2011.03.024.

[31] L. Zhou, H. Brunskill, M. Pletz, W. Daves, S. Scheriau, and R. Lewis, “Real-Time Measurement of Dynamic Wheel-Rail Contacts Using Ultrasonic Reflectometry,” *J. Tribol.*, vol. 141, no. 6, pp. 1–9, 2019, doi: 10.1115/1.4043281.

[32] J. Piotrowski and H. Chollet, “Wheel-Rail Contact Models for Vehicle System Dynamics Including Multi-Point Contact,” *Veh. Syst. Dyn.*, vol. 43, no. 6–7, pp. 455–483, 2005, doi: 10.1080/00423110500141144.

[33] J. B. Ayasse and H. Chollet, “Determination of the Wheel Rail Contact Patch in Semi-Hertzian Conditions,” *Veh. Syst. Dyn.*, vol. 43, no. 3, pp. 161–172, 2005, doi: 10.1080/00423110412331327193.

[34] F. Braghin, R. Lewis, R. S. Dwyer-Joyce, and S. Bruni, “A Mathematical Model to Predict Railway Wheel Profile Evolution Due to Wear,” *Wear*, vol. 261, no. 11–12, pp. 1253–1264, 2006, doi: 10.1016/j.wear.2006.03.025.

[35] M. S. Sichani, R. Enblom, and M. Berg, “A Novel Method to Model Wheel-Rail Normal Contact in Vehicle Dynamics Simulation,” *Veh. Syst. Dyn.*, vol. 52, no. 12, pp. 1752–1764, 2014, doi: 10.1080/00423114.2014.961932.

[36] Y. Sun, W. Zhai, and Y. Guo, “A Robust Non-Hertzian Contact Method for Wheel–Rail Normal Contact Analysis,” *Veh. Syst. Dyn.*, vol. 56, no. 12, pp. 1899–1921, 2018, doi: 10.1080/00423114.2018.1439587.

[37] R. Skrypnyk, J. C. O. Nielsen, M. Ekh, and B. A. Pålsson, “Metamodelling of Wheel–Rail Normal Contact in Railway Crossings with Elasto-Plastic Material Behaviour,” *Eng. Comput.*, vol. 35, no. 1, pp. 139–155, 2019, doi: 10.1007/s00366-018-0589-3.

[38] O. Polach and D. Nicklisch, “Wheel/Rail Contact Geometry Parameters in Regard to Vehicle Behaviour and Their Alteration with Wear,” *Wear*, vol. 366–367, pp. 200–208, 2016, doi: 10.1016/j.wear.2016.03.029.

[39] B. Zhu, J. Zeng, D. Zhang, and Y. Wu, “A non-Hertzian wheel-rail contact model considering wheelset yaw and its application in wheel wear prediction,” *Wear*, vol. 432–433, no. June, 2019, doi: 10.1016/j.wear.2019.202958.

[40] J. Piotrowski, B. Liu, and S. Bruni, “The Kalker book of tables for non-Hertzian contact of wheel and rail,” *Veh. Syst. Dyn.*, vol. 55, no. 6, pp. 875–901, 2017, doi: 10.1080/00423114.2017.1291980.

[41] S. Myamlin, J. Kalivoda, and L. Neduzha, “Testing of Railway Vehicles Using Roller Rigs,” *Procedia Eng.*, vol. 187, pp. 688–695, 2017, doi: 10.1016/j.proeng.2017.04.439.

[42] A. Jaschinski, H. Chollet, S. Iwnicki, A. Wickens, and J. W�rzen, “The Application of Roller Rigs to Railway Vehicle Dynamics,” *Veh. Syst. Dyn.*, vol. 31, no. 5–6, pp. 345–392, 1999, doi: 10.1076/vesd.31.5.345.8360.

[43] S. Association of American Railroads and M107/208, “Wheels, Carbon Steel,” 2011.

[44] Arema, “Manual for Railway Engineering, Volume 1 Track,” Lanham, MD.

[45] S. Z. Meymand and M. Ahmadian, “Design, Development, and Calibration of a Force-Moment Measurement System for Wheel-Rail Contact Mechanics in Roller Rigs,” *Meas. J. Int. Meas. Confed.*, vol. 81, pp. 113–122, 2016, doi: 10.1016/j.measurement.2015.12.012.

[46] A. Keylin, “Analytical Evaluation of the Accuracy of Roller Rig Data for Studying Creepage in Rail Vehicles,” 2012.

[47] A. Radmehr, A. Tajaddini, B. Marquis, and M. Ahmadian, “Virginia Tech Federal Railroad Administration Roller Rig Measurement Capabilities and Baseline Measurements,” in *Proceedings of the 2019 ASME Joint Rail Conference*, 2019.
[48] E. A. H. Vollebregt, “Updates on the Rocking Phenomenon,” in *Proceedings of the 25th International Symposium on Dynamics of Vehicles on Roads and Tracks*, 2017.
[49] E. A. H. Vollebregt, “Rocking on the Roller Rig: Formulas and Derivations,” 2017.
[50] K. L. Johnson, *Contact Mechanics*. Cambridge (UK): Cambridge University Press, 1985.
[51] K. L. Johnson, “Surface Interaction Between Elastically Loaded Bodies Under Tangential Forces,” *Proc. R. Soc.*, vol. A230, pp. 531–548, 1955.
[52] R. Lewis and U. Olofsson, *Wheel—rail interface handbook*. 2009.
[53] K. Corporation, “In-Line Profile Measurement System, High-Speed 2D/3D Laster Scanner, LJ-V7000 Series,” 2016.
[54] L. T. Inc., “Gocator 2300 Series Catalog,” 2013.
[55] A. G. Asuero, A. Sayago, and A. G. González, “The correlation coefficient: An overview,” *Crit. Rev. Anal. Chem.*, vol. 36, no. 1, pp. 41–59, 2006, doi: 10.1080/10408340500526766.
[56] H. R. Hertz, “Uber die Beruhrung fester elastischer Korper und Uber die Harte,” *Verhandlung des Vereins zur Beforderung des GewerbefleiBes*, p. 449, 1882.
[57] J.-B. Ayasse and H. Chollet, “Wheel-Rail Contact,” in *Handbook of Railway Vehicle Dynamics*, 2006, pp. 85–120.
[58] V. Garg and R. Dukkipati, *Dynamics of Railway Vehicle Systems*. Orlando (FL): Elsevier, 1984.
[59] Fujifilm Prescale, “Tactile Pressure Indicating Sensor Film Catalog,” 2015.
[60] Fujifilm Corporation, “Prescale Pressure Measurement Film Catalog,” Japan.
[61] V. L. Popov, *Contact Mechanics and Friction - Hertz force*. 2010.
[62] J. J. Kalker, *Three-Dimensional Elastic Bodies in Rolling Contact*. 1990.
[63] P. Meijers, “The contact problem of a rigid cylinder on an elastic layer,” *Appl. Sci. Res.*, vol. 18, no. 1, pp. 353–383, 1968, doi: 10.1007/BF00382359.

ACKNOWLEDGEMENTS

The authors wish to thank and acknowledge the US Department of Transportation, University Transportation Center Program (RailTEAM UTC) for funding support for this research.

ABOUT THE AUTHORS

Mehdi Ahmadian, J. Bernard Jones Chair and Director

Dr. Mehdi Ahmadian is a Dan Pletta Professor of Mechanical Engineering at Virginia Tech, where he also holds the position of Director of Center for Vehicle Systems and Safety (CVeSS), and the Railway Technologies Laboratory (RLT). Dr. Ahmadian has authored more than 130 archival journal publications and more than 250 conference publications, including a number of keynote lectures. He has served as Editor or Editor-in-Chief for four journals on Vehicle System Dynamics, Vibration and Control, Shock and Vibration and Automobile Engineering. Dr. Ahmadian is Fellow of American Society of Mechanical Engineers of the American Institute for Aeronautics and Astronautics (AIAA). He has received many distinguished scholar awards.

Ahmad Radmehr

Ahmad Radmehr was a graduate research assistant when he worked on this project. Ahmad earned his Ph.D. in Mechanical Engineering in December 2020 at Virginia Tech, He received his B.Sc. in Mechanical Engineering from Isfahan University of Technology and his M.Sc. at Sharif University of Technology.